Metal Waveguides for Multi-Axial Light Guiding at Nanometer Scales

by

Muhammad Waqas Maqsood

B.Sc., University of Engineering and Technology, 2008

A THESIS SUBMITTED IN PARTIAL FULFILLMENT OF
THE REQUIREMENTS FOR THE DEGREE OF

MASTER OF APPLIED SCIENCE

in

The College of Graduate Studies

(Electrical Engineering)

THE UNIVERSITY OF BRITISH COLUMBIA

(Okanagan)

December 2011

Abstract

Recent advancements in nanofabrication now allow precise fabrication of devices and systems on nanometer scales. This technology is currently used in the field of photonics to construct optical systems possessing sub-wavelength features. A basic component of most optical systems is an optical waveguide. There has been an increased interest in nanofabricated optical waveguides that incorporate metal layers due to their fabrication compatibility with existing complimentary-metal-oxide-semiconductor (CMOS) processes and, as will be discussed in this thesis, their ability to sustain sub-wavelength-confined electromagnetic modes. In this work, we have developed analytical techniques for designing metal waveguides that achieve tailored optical functionalities. The developed techniques are applied in two design examples which address contemporary problems related to waveguiding at sub-wavelength and nanometer scales.

Realization of complex optical circuits based on miniaturized optical waveguides requires components that can bend light around tight 90° bends. In the first design example, we apply our analytical technique to optimize a bi-axial waveguide constructed from two uni-axial metal waveguides joined together at 90°. The optimization procedure consists of mapping out wavevector values of the electromagnetic modes sustained by the two waveg-

uides over the intended operational frequency range. The constituent materials and geometry of the waveguides are selected such that each waveguide sustains only one low-loss mode. The geometry of each of the waveguides is tailored in such a way that the in-plane wavevector components for both waveguide modes are matched. The wavevector matching results in efficient coupling between the two modes, yielding 90° light bending with predicted efficiencies over 90%.

In the second design example, we apply our analytical technique to optimize a bi-axial waveguide structure for coupling free-space light into surface plasmon polaritons (SPP), electromagnetic excitations bounded to the surface of a metal. One of the practical challenges in realizing devices that use SPPs is the development of efficient ways to couple in free-space plane-wave light. We study the simple SPP coupling geometry consisting of a slit in a metal film, filled and covered with a dielectric. We break the configuration down into two constituent uni-axial waveguide components, modeling the slit as a metal-dielectric-metal waveguide and the adjacent metal surface as a metal-dielectric waveguide. Using similar analysis as in the first example, we optimize the materials and geometry of the slit so that wavevector matching is achieved between the light emanating from the slit and the adjacent SPP modes, resulting in predicted peak SPP coupling efficiencies over 68%.

Preface

This work has been done under the guidance of Dr. Kenneth Chau at the School of Engineering in The University of British Columbia. My colleague Reyad Mehfuz was involved with the finite-difference time-domain technique (FDTD) calculations. Throughout the course of this work, Dr. Chau has played a key role in providing guidance and support. Portions of my thesis have been published in two journal articles:

- M. W. Maqsood, R. Mehfuz, and K. J. Chau, "High-throughput diffraction assisted surface-plasmon-polariton coupling by a super-wavelength slit," Optics Express **18**, 21669-21677 (2010).

- M. W. Maqsood, R. Mehfuz, and K. J. Chau, "Design and optimization of a high-efficiency nanoscale $\pm 90^{\circ}$ light-bending structure by mode selection and tailoring," Applied Physics Letters **97**, 151111 (2010),

A portion of the thesis has also been published in a conference proceeding:

- M. W. Maqsood, K. J. Chau, "Designing a Nanometer-scale Light Bending Structure," Proceedings of SPIE (6pp), in press (2011).

Table of Contents

List of Tables

List of Figures

Acknowledgements

I would like to thank my supervisor, Dr. Kenneth Chau, for introducing me to the interesting topics of metal waveguides and surface waves. He has been a great person and a source of inspiration for me. His guidance and encouragement throughout my thesis were invaluable. I am also thankful to Dr. Thomas Johnson who served as an examination committee member for my thesis. The discussions I had with him were very useful in shaping my masters.

I would also like to thank my colleague, Reyad Mehfuz, for all of his support. His work using FDTD technique has been very helpful and played an important role in development of this work.

At the end, I would like to thank my family members. Their support throughout this time has been remarkable and has been instrumental in shaping my life and career.

To my family for their support and for all those who seek truth

Chapter 1

Introduction

1.1 Optical Waveguides: from Water Streams to Nanometer-Scale Metallic Structures

An optical waveguide is a device that can guide light. This is achieved by confining light within a boundary such that light can only propagate along one or multiple directions defined by the waveguide [1]. The first optical waveguide was demonstrated in 1840 by Daniel Colladon using a thin curved stream of falling water [2]. A beam of light shone into the water stream was shown to follow the curvature of the stream. The stream of water thus acted like a pipe for light. In 1870, John Tyndall explained this phenomenon in terms of total internal reflection (TIR) [3]. TIR occurs at an interface between two media having different optical refractive indices. Consider an interface formed between dielectric medium 1 with refractive index n_1 and dielectric medium 2 with refractive index n_2. A beam of light incident from medium 1 into medium 2 will obey Snell's law, written as

$$n_1 sin\theta_i = n_2 sin\theta_r, \tag{1.1}$$

where $0 \leq \theta_i \leq 90$ is the angle of incidence of the beam (with respect to normal to the interface) and θ_r is the angle of refraction of the beam refracted into medium 2. When n_1 is greater than n_2, there exists an acute critical angle of incidence where the refracted beam becomes parallel to the interface. For angles of incidence greater than the critical angle, light no longer refracts, but is totally internally reflected. This forms the basis of optical waveguiding using dielectric materials.

Since the 1970s, developments in glass processing technology have allowed the controlled manufacturing of optical fibre waveguides constructed from thin glass wires. An optical fiber consists of two concentric glass regions: a cylindrical core of higher refractive index and a surrounding cladding of lower refractive index. The optical fibre works by guiding light along the axis of the fibre and confining light within the core by total internal reflection. Fiber optics have revolutionized the field of communications by providing a means to transfer information with low loss, high speed, wide bandwidth, and immunity to electromagnetic interference, which has translated into tangible benefits such as fast internet speeds and instantaneous communication across continents.

Along with faster information transmission via optical fibres, the last half century has witnessed dramatic miniaturization of electronic components, resulting in smaller devices with more functionalities. The modern cellular phone, for example, has more processing power than the original room-sized computers. This miniaturization has been possible due to the development of nanofabrication processes enabling controllable manufacturing on nanometer-size scales. In the last decades, there has been intense

research interest in using nanofabrication to miniaturize optical waveguides. The motivation for these efforts has been two-fold: first, smaller optical waveguides means that more functionalities can be compressed into an optical system [4–9] and second, optical waveguides that are size-compatible with smaller electronic components could pave the way to opto-electronic systems that exploit both the advantages of electronics and optics, which could lead to significantly faster and more powerful computers [10–13].

A major road-block in efforts to miniaturize optical waveguides is the so-called "diffraction limit". This term was originally used to describe the minimum resolution that can be achieved by an optical imaging system (on the order of the wavelength of light). The same physical constraints placed on the resolution of optical imaging systems also applies to most optical waveguiding systems. Generally, light cannot propagate in a dielectric-based waveguide system when the transverse profile of the waveguide is less than the wavelength of light. At infrared and visible frequencies, this means that the minimum transverse profile size of an optical waveguide is on the order of 100s of nanometers or even microns, which is several orders of magnitude greater than the typical feature sizes of electronic components [11, 14, 15]. This constraint can be overcome by using optical waveguides constructed from metals. A waveguide created using metallic components can support light waves that propagate even when the transverse profile of the waveguide is significantly less than the wavelength of light [16–19]. In recent years, there has been tremendous research interest in the development of nanometer-scale optical waveguides constructed from metallic components. Metallic waveguiding systems have been realized

in the form metal nanoparticle arrays [20], metal nanowires [21–24], and nano-apertures in metal films [14, 25–27]. Research continues to understand light interactions with these small metallic systems and to optimize their performance.

1.2 Designing Uni- and Multi-Axial Optical Waveguides

With the advent of nanofabrication, optical waveguides can now be created in a wide range of geometries using dielectric, metallic, or semiconducting materials. Given the many degrees of freedom afforded by nanofabrication, optimization of a waveguide design requires efficient modeling techniques. All modeling schemes are, in some way or another, rooted in Maxwell's equations, a set of four equations describing the relationship between electromagnetic fields and their sources. The way in which Maxwell's equations are applied to model a given optical waveguide depends in large measure on the geometry of the waveguide. One of the simplest configurations is the uni-axial waveguide, which guides electromagnetic waves along a single axial direction. The electromagnetic properties of a uni-axial waveguide can be modeled by analytically solving Maxwell's equations. This is achieved by assuming a general form of the electromagnetic fields propagating along the direction of the waveguide. Applying boundary conditions to the interfaces of the waveguide yields characteristic eigenvalue equations having solutions corresponding to the wavevector of a wave. This wavevector contains information on the wavelength and attenuation of the wave. When a uni-axial

waveguide is composed of dielectric materials described by real permittivity values, the resulting eigenvalue equation is real and can be easily solved using standard root-finding algorithms like the Newton-Raphson method. When the uni-axial waveguide is composed of metallic materials described by complex permittivity values, the resulting eigenvalue equation is complex and requires more sophisticated root-finding algorithms.

Multi-axial waveguides guide electromagnetic waves along more than one direction. They are challenging to model by analytical solutions to Maxwell's equations and often require numerical techniques. One of the most popular numerical techniques is the finite-difference time-domain (FDTD) technique. The FDTD technique is based on a one-, two-, or three-dimensional spatial grid containing the waveguide structure and an electromagnetic wave source. Approximating the time- and space- derivatives of Maxwell's equations using difference equations, Maxwell's equations are solved to determine the electric and magnetic field values in the simulation space at each grid point as a function of time. Numerical simulation tools like the FDTD technique are powerful because they enable detailed visualization of electromagnetic fields within complicated optical waveguides. One of the major limitations, however, is the massive computational power and processing time required to complete a simulation. Because only one combination of parameters can be explored for a given simulation, hundreds or thousands of simulations are required to completely map out the frequency-dependent electromagnetic response of an optical waveguide for various material combinations and geometrical configurations. As a result, optimization using only numerical simulations is often not feasible.

1.3 Analytical Approach for Designing Multi-Axial Metallic Waveguides

The goal of this thesis is to explore a new analytical method to model the electromagnetic properties of multi-axial, metallic, nanometer-scale waveguides. The methodology is based on conceptually dividing a multi-axial waveguide into uni-axial waveguide sub-components. By approximating the more-complex multi-axial waveguide as a collection of simpler uni-axial waveguide parts, analytical solutions can be obtained to describe electromagnetic wave behaviour in different regions of the multi-axial waveguide. To achieve electromagnetic coupling between uni-axial waveguide components, the geometries of the uni-axial waveguide components are tailored so that the in-plane electromagnetic momenta are matched. This is achieved by analytically mapping out the electromagnetic wavevectors of the uni-axial waveguide sub-components as a function of both frequency and geometry and then tailoring the geometries so that the magnitudes of the wavevectors are equal. We test the predictive power of this approach in two design examples in which visible-frequency electromagnetic waves are guided by bi-axial, metallic, nanometer-scale waveguides along two directions. Optimal parameters selected to yield maximum coupling using our analytical method are shown to match those predicted to yield maximum coupling using FDTD numerical simulations. Our analytical method thus provides a supplemental, high-level tool for the design of complicated waveguide systems and provides new physical insights into multi-axial electromagnetic waveguiding.

1.4 Thesis Outline

This thesis is divided into two parts. The first part, consisting of Chapters 1 and 2, develops the theoretical background required for understanding the design technique and the second part, consisting of Chapters 3 and 4, describe the two basic examples where the technique is applied.

In the remainder of Chapter 1, we will introduce classical electromagnetic theory used in the thesis. Chapter 2 describes the background and theory of metallic waveguides. We formulate the dispersion relations describing electromagnetic modes in metallic waveguides and discuss the numerical techniques used to find their roots. In Chapters 3 and 4, we discuss the application of a new analytical method to model bi-axial, metallic, nanoscale waveguides based on breaking down the bi-axial waveguide into two uni-axial waveguide sub-components. Predictions based on this method are compared with predictions using well-accepted FDTD simulations. The thesis concludes in Chapter 5. Appendix A lists a series of analytical functions that are fitted to the wavevector of electromagnetic modes in various metallic waveguide structures. The intention is to provide the interested reader with easy-to-evaluate functions and to circumvent the need to solve the complex dispersion relations, which can be tedious and time-consuming.

1.5 Maxwell's Equations

In 1873, J. C. Maxwell developed the fundamental equations describing the behavior of electromagnetic waves [28]. The equations relate four vector fields - the displacement field, **D**, the electric field, **E**, the magnetic flux density, **B**, and the magnetic field, **H** - to the presence of charge density, ρ, and current density, **J**. The equations are given by

$$\nabla \cdot \mathbf{D}(\mathbf{r}, t) = \rho, \tag{1.2}$$

$$\nabla \cdot \mathbf{B}(\mathbf{r}, t) = 0, \tag{1.3}$$

$$\nabla \times \mathbf{E}(\mathbf{r}, t) = -\frac{\partial \mathbf{B}(\mathbf{r}, t)}{\partial t}, \tag{1.4}$$

and

$$\nabla \times \mathbf{H}(\mathbf{r}, t) = \mathbf{J}(\mathbf{r}, t) + \frac{\partial \mathbf{D}(\mathbf{r}, t)}{\partial t}, \tag{1.5}$$

where (**r**,t) describes the position and time dependence of the fields. The displacement field, **D** is related to electric field, **E** and magnetic flux density field, **B** is related to magnetic field, **H** via

$$\mathbf{D}(\mathbf{r}, t) = \epsilon_o \mathbf{E}(\mathbf{r}, t) + \mathbf{P}(\mathbf{r}, t) \tag{1.6}$$

and

$$\mathbf{B}(\mathbf{r}, t) = \mu_o \mathbf{H}(\mathbf{r}, t) + \mathbf{M}(\mathbf{r}, t), \tag{1.7}$$

where ϵ_o is the free-space permittivity, μ_o is the free-space permeability, **P** is the polarization field and **M** is the magnetization field.

1.5.1 Constitutive Material Relations

The fields **P**, **M**, and **J** describe the response of a medium to electromagnetic fields. By assuming a medium that is linear, isotropic, lossless, and instantaneously responsive, we get the relations

$$\mathbf{P}(\mathbf{r},t) = \epsilon_o \chi_e \mathbf{E}(\mathbf{r},t), \tag{1.8}$$

$$\mathbf{M}(\mathbf{r},t) = \mu_o \chi_m \mathbf{H}(\mathbf{r},t), \tag{1.9}$$

and

$$\mathbf{J}(\mathbf{r},t) = \sigma \mathbf{E}(\mathbf{r},t), \tag{1.10}$$

where χ_e is the electric susceptibility, χ_m is the magnetic susceptibility, and σ is the electric conductivity.

Inserting Eq. 1.8 into Eq. 1.6, we get

$$\mathbf{D}(\mathbf{r},t) = \epsilon_o \epsilon_r \mathbf{E}(\mathbf{r},t) \tag{1.11}$$

where ϵ_r is the relative electric permittivity given by

$$\epsilon_r = 1 + \chi_e. \tag{1.12}$$

Similarly, inserting Eq. 1.9 into Eq. 1.7, we get

$$\mathbf{B}(\mathbf{r},t) = \mu_o \mu_r \mathbf{H}(\mathbf{r},t), \tag{1.13}$$

where μ_r is relative magnetic permeability given by

$$\mu_r = 1 + \chi_m. \tag{1.14}$$

For most materials, $\chi_m \simeq 0$ and $\mu_r = 1$.

1.5.2 Electromagnetic Wave Equation

We generally deal with systems having no external charge ($\rho = 0$). Imposing the additional constraint that $\mathbf{J} = 0$, Maxwell's equations for such systems can be written as

$$\nabla \cdot \mathbf{D}(\mathbf{r}, t) = 0, \tag{1.15}$$

$$\nabla \cdot \mathbf{B}(\mathbf{r}, t) = 0, \tag{1.16}$$

$$\nabla \times \mathbf{E}(\mathbf{r}, t) = -\frac{\partial \mathbf{B}(\mathbf{r}, t)}{\partial t}, \tag{1.17}$$

and

$$\nabla \times \mathbf{H}(\mathbf{r}, t) = \frac{\partial \mathbf{D}(\mathbf{r}, t)}{\partial t}. \tag{1.18}$$

Inserting the constitutive relation of Eq. 1.11 in Eq. 1.15 we get:

$$\begin{aligned} \nabla \cdot (\epsilon_o \epsilon_r \mathbf{E}(\mathbf{r}, t)) &= 0, \\ \epsilon_o \epsilon_r (\nabla \cdot \mathbf{E}(\mathbf{r}, t)) + \mathbf{E}(\mathbf{r}, t) \cdot \nabla(\epsilon_o \epsilon_r) &= 0, \end{aligned}$$

which yields

$$\nabla \cdot \mathbf{E}(\mathbf{r}, t) = -\frac{\mathbf{E}(\mathbf{r}, t) \cdot \nabla(\epsilon_o \epsilon_r)}{\epsilon_o \epsilon_r}. \tag{1.19}$$

For an isotropic and homogeneous medium, $\nabla(\epsilon_o\epsilon_r) = 0$, which leads to the compact relation

$$\nabla \cdot \mathbf{E}(\mathbf{r}, t) = 0. \tag{1.20}$$

Using Eq. 1.13 with $\mu_r = 1$ (for nonmagnetic materials), Eq. 1.17 becomes

$$\nabla \times \mathbf{E}(\mathbf{r}, t) = -\mu_o \frac{\partial \mathbf{H}(\mathbf{r}, t)}{\partial t}. \tag{1.21}$$

Taking the curl of both sides yields

$$\begin{aligned} \nabla \times \nabla \times \mathbf{E}(\mathbf{r}, t) &= \nabla \times \left(-\mu_o \frac{\partial \mathbf{H}(\mathbf{r}, t)}{\partial t}\right) \\ &= -\mu_o \frac{\partial}{\partial t}(\nabla \times \mathbf{H}(\mathbf{r}, t)). \end{aligned} \tag{1.22}$$

Using Eq. 1.18, Eq. 1.22 simplifies to

$$\begin{aligned} \nabla \times \nabla \times \mathbf{E}(\mathbf{r}, t) &= -\mu_o \frac{\partial^2 \mathbf{D}(\mathbf{r}, t)}{\partial t^2} \\ &= -\mu_o \epsilon_o \epsilon_r \frac{\partial^2 \mathbf{E}(\mathbf{r}, t)}{\partial t^2}. \end{aligned} \tag{1.23}$$

The left side of Eq. 1.23 simplifies to

$$\nabla \times \nabla \times \mathbf{E}(\mathbf{r}, t) = \nabla(\nabla \cdot \mathbf{E}(\mathbf{r}, t)) - \nabla^2 \mathbf{E}(\mathbf{r}, t) \tag{1.24}$$

Using Eq. 1.20 in Eq. 1.24 yields

$$\nabla \times \nabla \times \mathbf{E}(\mathbf{r}, t) = -\nabla^2 \mathbf{E}(\mathbf{r}, t). \tag{1.25}$$

Combining Eq. 1.23 and Eq. 1.25, we get

$$\nabla^2 \mathbf{E}(\mathbf{r}, t) - \mu_o \epsilon_o \epsilon_r \frac{\partial^2 \mathbf{E}(\mathbf{r}, t)}{\partial t^2} = 0. \tag{1.26}$$

Given the speed of light defined by

$$c = \frac{1}{\sqrt{\mu_o \epsilon_o}}, \tag{1.27}$$

we arrive at the general wave equation

$$\nabla^2 \mathbf{E}(\mathbf{r}, t) - \frac{\epsilon_r}{c^2} \frac{\partial^2 \mathbf{E}(\mathbf{r}, t)}{\partial t^2} = 0, \tag{1.28}$$

which is also known as the *Helmholtz wave equation*. Using a similar treatment for the magnetic field yields

$$\nabla^2 \mathbf{H}(\mathbf{r}, t) - \frac{\epsilon_r}{c^2} \frac{\partial^2 \mathbf{H}(\mathbf{r}, t)}{\partial t^2} = 0. \tag{1.29}$$

The above equations describe the electric and magnetic field component of an electromagnetic wave as it travels in a medium. Both equations will be used for analyzing the electromagnetic wave behaviour in a medium.

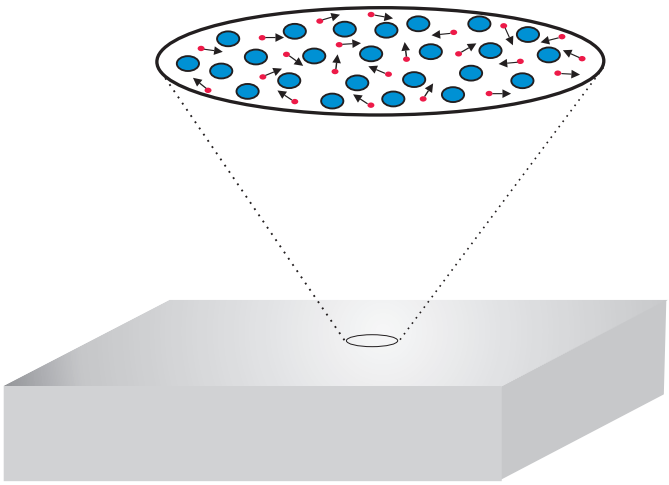

Figure 1.1: Cartoon depiction of a piece of metal. The magnified part of the metal shows its microscopic constituents consisting of free electrons (red dots) moving around fixed positive ions (blue circles).

1.6 Drude Model

In 1900, Paul Drude explained the transport of electrons in metals by applying the principles of kinetic theory [29, 30]. In this treatment, metals consist of a density of free electrons, ρ_n, immersed in a collection of positive ions, as shown in Fig. 1.1. The electrons are unbound and free to move, surrounded by background ions without any restoring force.

When an external oscillating electromagnetic field is applied to the metal, electrons start oscillating. These oscillations are damped by electron collisions with other electrons and ions. The damping rate is approximately $1/\tau$, where τ is the average time between collisions [31]. To derive the equation of motion for an electron inside the metal, let's consider an electromagnetic wave varying in the x-axis and uniform along all other directions such that

$\mathbf{E}(\mathbf{r},t) = E(x,t)\hat{x}$. Treating a free electron like a classical particle, we have the equation of motion [32]

$$m\frac{d^2\tilde{\ell}}{dt^2} + \frac{m}{\tau}\frac{d\tilde{\ell}}{dt} = -eE(x,t), \tag{1.30}$$

where $\tilde{\ell}$, m, and e are the displacement, effective mass, and charge of an electron, respectively.

Generally, the electric field is time-harmonic with the form

$$\tilde{E}(\omega) = E_0(x)e^{-i\omega t}, \tag{1.31}$$

where ω is the frequency. Time-harmonic excitation yields time-harmonic electron motion given by

$$\tilde{\ell}(\omega) = \tilde{\ell}_o e^{-i\omega t}, \tag{1.32}$$

where $\tilde{\ell}_o$ is a complex quantity whose magnitude is equal to the peak displacement and whose phase describes temporal shifts between the electron displacement and the driving field [33, 34].

Inserting Eq. 1.32 into Eq. 1.31 yields

$$m(-\omega^2\tilde{\ell}_o e^{-i\omega t}) + \frac{m}{\tau}(-i\omega\tilde{\ell}_o e^{-i\omega t}) = -e\tilde{E}(\omega)$$

$$-m\omega\tilde{\ell}_o e^{-i\omega t}\left(\omega + \frac{i}{\tau}\right) = -e\tilde{E}(\omega)$$

which results in the complex amplitude

$$\tilde{\ell}(\omega) = \frac{e\tilde{E}(\omega)}{m\omega(\omega + i/\tau)}. \tag{1.33}$$

The displacement of individual electrons contribute towards a dipole moment density. This dipole moment density yields a polarization field given by

$$\begin{aligned} \tilde{P}(\omega) &= -\rho_n e \tilde{\ell}(\omega) \\ &= -\frac{\rho_n e^2}{m\omega(\omega + i/\tau)} \tilde{E}(\omega). \end{aligned} \tag{1.34}$$

In frequency-domain notation, the polarization field is related to the electric field by

$$\tilde{P}(\omega) = \epsilon_o(\tilde{\epsilon}_m(\omega) - 1)\tilde{E}(\omega), \tag{1.35}$$

where $\tilde{\epsilon}_m$ is the frequency-dependent relative electric permittivity of the metal. Comparing Eqs. 1.34 and 1.35, we obtain the dielectric function

$$\tilde{\epsilon}_m(\omega) = 1 - \frac{\rho_n e^2}{m\omega\epsilon_o(\omega + i/\tau)}. \tag{1.36}$$

Given the plasma frequency for a free electron gas $\omega_p^2 = \rho_n e^2/m\epsilon_o$, $\tilde{\epsilon}_m$ is then given by

$$\tilde{\epsilon}_m(\omega) = 1 - \frac{\omega_p^2}{\omega(\omega + i/\tau)}. \tag{1.37}$$

Re-writing Eq. 1.37 into a distinctive real part, $\epsilon'(\omega)$, and imaginary part, $\epsilon''(\omega)$, yields

$$\tilde{\epsilon}_m(\omega) = 1 - \frac{\omega_p^2}{(\omega^2 + 1/\tau^2)} + i\frac{\omega_p^2\tau}{\omega(1 + \omega^2\tau^2)}. \tag{1.38}$$

1.7 Limitations of the Drude Model

In this section, we examine the accuracy of the Drude model for describing the dielectric functions of noble metals over visible frequencies. We select gold and silver because they both have low losses at visible frequencies ($4.5 \times 10^{14} - 8 \times 10^{14}$ Hz) and are widely used in optical waveguides. We use experimentally-measured values of the plasma frequency and collision rates for gold and silver measured by Zeman and Sachts in [35] and summarized in Table 1.1. The experimentally-measured parameters are then inserted into the analytical function given in Eq.1.38. The resulting real and imaginary components of the dielectric function are compared to complex permittivity values experimentally measured by Johnson and Christy [36].

Table 1.1: Constant parameters for the Drude model for Ag and Au

Metal	**Plasma frequency ω_p (Hz)**	**Collision rate τ^{-1} (s^{-1})**
Silver	2.186×10^{15}	5.139×10^{12}
Gold	2.15×10^{15}	17.14×10^{12}

As shown in Fig. 1.2, values of $\mathrm{Re}[\epsilon_m]$ for gold obtained from the Drude model closely match the experimental data over a frequency range spanning from the infrared to the ultraviolet. On the other hand, values of $\mathrm{Im}[\epsilon_m]$ match the experimental data only at lower frequencies below 4.5×10^{14} Hz (Fig. 1.3). Deviations of the Drude model from experimentally-measured

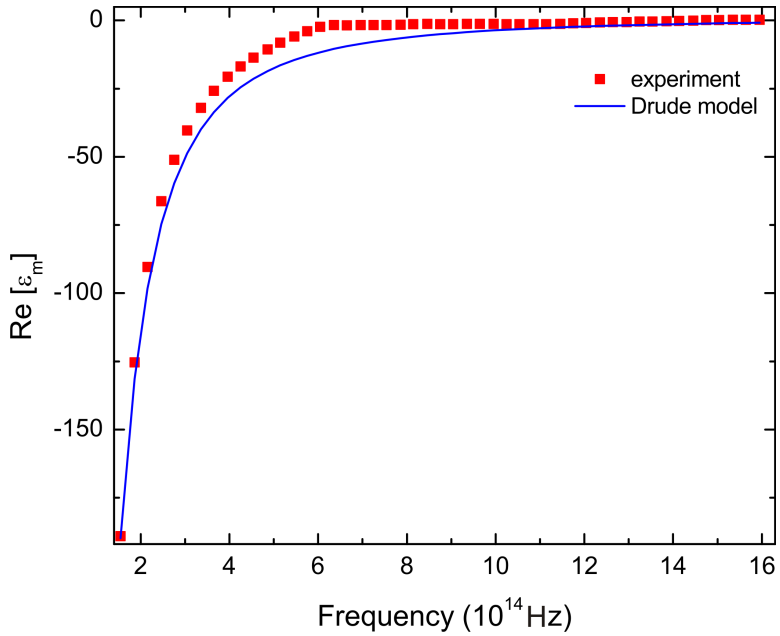

Figure 1.2: Comparison between Re[ϵ_m] values for gold obtained indirectly from the Drude model using experimentally-measured ω_p and τ (line) with those obtained directly from permittivity measurements (squares).

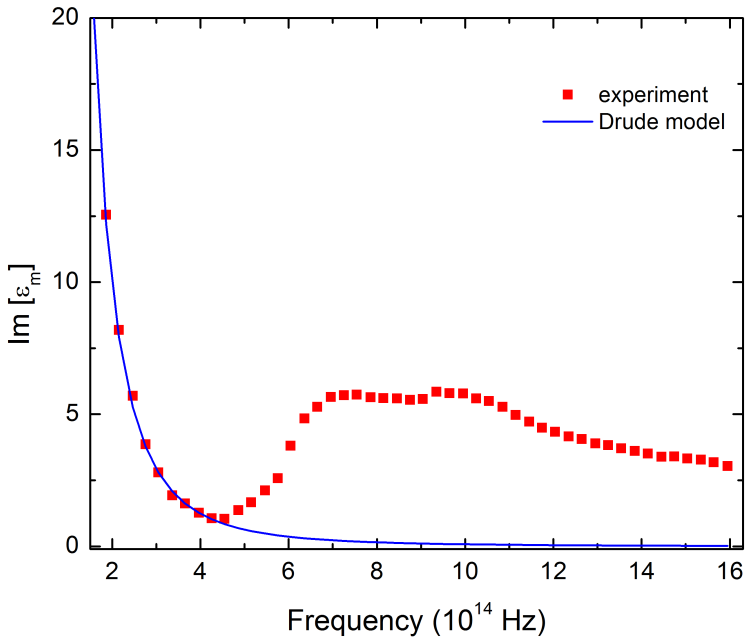

Figure 1.3: Comparison between Im[ϵ_m] values for gold obtained from indirectly from the Drude model using experimentally-measured ω_p and τ (line) with those obtained directly from permittivity measurements (squares).

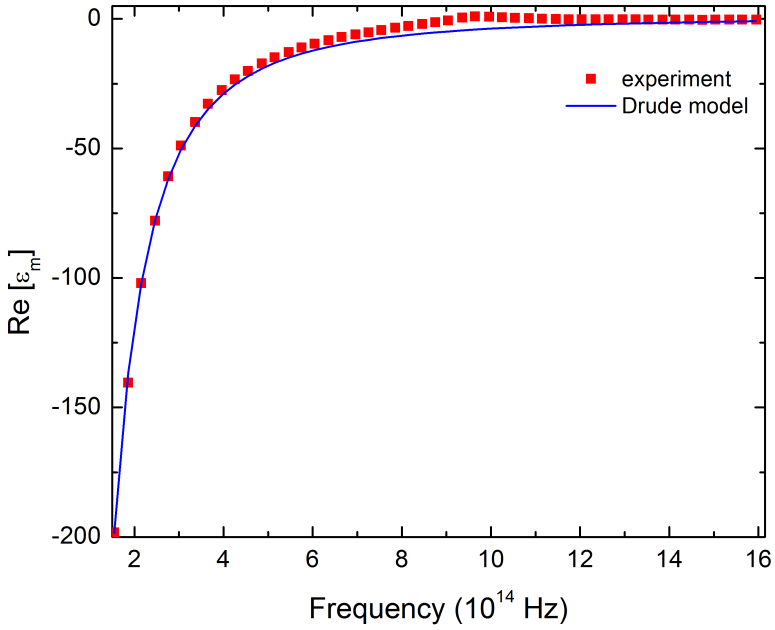

Figure 1.4: Comparison between Re[ϵ_m] values for silver obtained indirectly from the Drude model using experimentally-measured ω_p and τ (line) with those obtained directly from permittivity measurements (squares).

values at higher frequencies are attributed to inter-band transitions which are not accounted for in the Drude model.

Application of the Drude model to silver yields similar trends to those observed for gold. While there is a good agreement with experimentally-measured values of Re[ϵ_m] throughout the frequency range (Fig. 1.4), agreement with experimentally-measured values of Im[ϵ_m] is achieved only at lower frequencies below 4.0×10^{14} Hz (Fig. 1.5). Agreement between the Drude model predictions and experimental data for both gold and silver

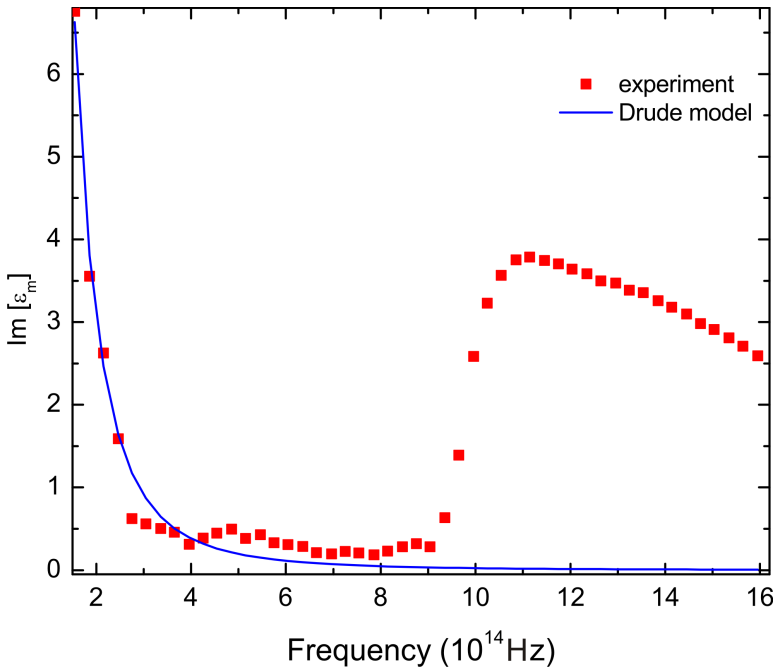

Figure 1.5: Comparison between Im[ϵ_m] values for silver obtained indirectly from the Drude model using experimentally-measured ω_p and τ (line) with those obtained directly from permittivity measurements (squares).

suggests that, at lower frequencies, the free-electron picture is an accurate description of the microscopic motion of electrons. At higher frequencies, modifications to the Drude model are required to accurately describe interband transitions. These modifications can be implemented, for instance, by restricting the free-electron approximation and modeling electrons as bound, resonant entities [37].

The imaginary part of a medium's dielectric function describes the attenuation of an electromagnetic wave propagating in the medium. Silver is an ideal metal for optical waveguiding because its Im[ϵ_m] at visible fre-

quencies is among the lowest of all metals [38, 39] and, as a result, exhibits the lowest visible-frequency losses. Throughout the remainder of the thesis, we will restrict our treatment of metallic waveguide systems by considering only those consisting of silver.

1.8 Dielectric Function for Silver

We describe the complex dielectric function of silver by high-order polynomial fits to the Johnson and Christy experimental data. The order of the polynomial is chosen such that the difference between the fit and experimental data is minimum. The polynomial fit for the real part of the dielectric function is obtained as

$$\begin{aligned} \mathrm{Re}[\tilde{\epsilon}_m(f)] &= -958.72693 + (9.24279 \times 10^{-12})\, f \\ &\quad - (3.99243 \times 10^{-26})\, f^2 + (9.69973 \times 10^{-41})\, f^3 \\ &\quad - (1.43038 \times 10^{-55})\, f^4 + (1.30694 \times 10^{-70})\, f^5 \\ &\quad - (7.22877 \times 10^{-86})\, f^6 + (2.21643 \times 10^{-101})\, f^7 \\ &\quad - (2.88985 \times 10^{-117})\, f^8 \end{aligned} \tag{1.39}$$

where f is the frequency in units of Hz. As shown in Fig. 1.6, the polynomial function given in Eq. 1.39 accurately models experimentally-measured values of $\mathrm{Re}[\epsilon_m]$, with only slight deviations at higher frequencies above the visible spectrum. To obtain a polynomial fit for the imaginary part of the dielectric function of silver, we divide the visible frequency spectrum into

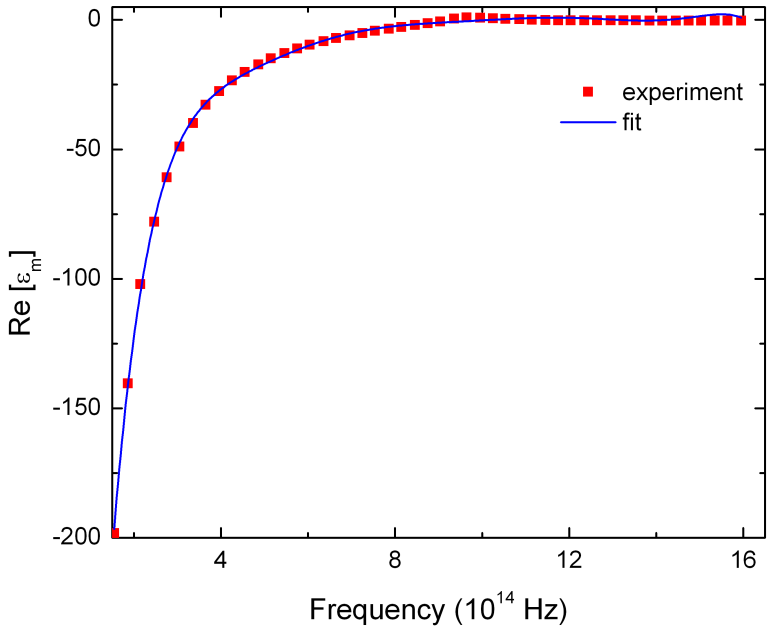

Figure 1.6: Polynomial fit function to model the real part of the dielectric function of silver.

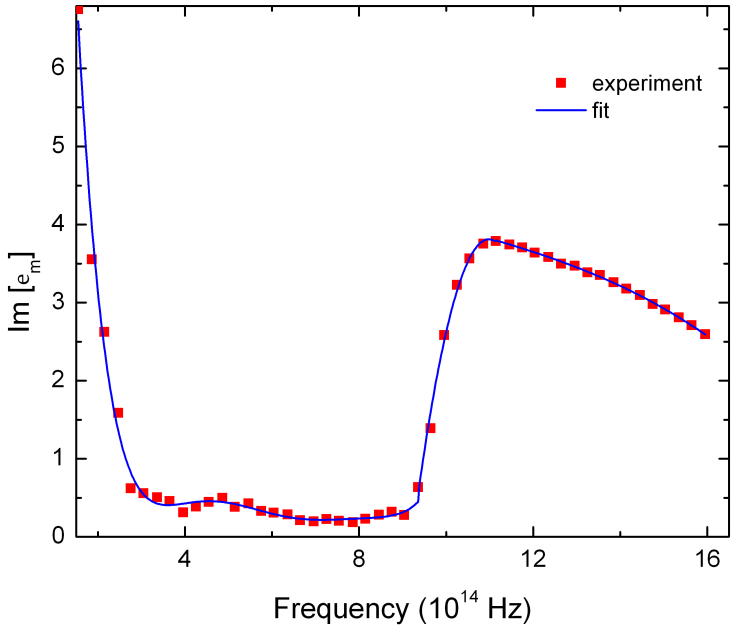

Figure 1.7: Polynomial fit function to model the imaginary part of the dielectric function of silver.

three intervals.

For 1.54683×10^{14} Hz$< f < 9.35347 \times 10^{14}$ Hz, the fit function is

$$\begin{aligned} \mathrm{Im}[\tilde{\epsilon}_m(f)] &= 48.47405 - (5.22332 \times 10^{-13})\, f \\ &\quad + (2.29072 \times 10^{-27})\, f2 - (5.18924 \times 10^{-42})\, f^3 \\ &\quad + (6.41697 \times 10^{-57})\, f^4 - (4.12193 \times 10^{-72})\, f^5 \\ &\quad + (1.07857 \times 10^{-87})\, f^6, \end{aligned} \tag{1.40}$$

for 9.35347×10^{14} Hz$\leq f < 9.35347 \times 10^{14}$ Hz, the fit function is

$$\begin{aligned} \mathrm{Im}[\tilde{\epsilon}_m(f)] &= 7.36947 - (7.29005 \times 10^{-15})\, f + \\ & \quad (5.92 \times 10^{-30})\, f^2 - (2.024 \times 10^{-45})\, f^3, \end{aligned} \tag{1.41}$$

and for $f \geq 9.35347 \times 10^{14}$ Hz, the fit function is

$$\begin{aligned} \mathrm{Im}[\tilde{\epsilon}_m(f)] &= -145.44771 + (2.71872 \times 10^{-13})\, f \\ & \quad - (1.23802 \times 10^{-28})\ f^2. \end{aligned} \tag{1.42}$$

As shown in Fig. 1.7, the piece-wise polynomial fit function accurately models experimentally-measured values of $\mathrm{Im}[\epsilon_m]$.

1.9 Summary

In this chapter, we have introduced classical electromagnetic theory in the form of Maxwell's equations and derived the general electromagnetic wave equations. We have discussed the application of the Drude model for describing the complex dielectric function of noble metals and shown that at visible frequencies, the Drude model yields inaccurate results. To describe the dielectric function of silver (which will be used throughout the remainder of this thesis), we have introduced analytical high-order polynomial functions fitted to experimentally-measured data. In the next chapter, we will apply Maxwell's equations to model the electromagnetic properties of uni-axial waveguides constructed from metallic constituents.

Chapter 2

Metallic Waveguides

2.1 Uni-Axial Waveguide Composed of a Single Metal-Dielectric Interface

A uni-axial waveguide is a structure that guides electromagnetic waves along one direction. One of the simplest ways to implement a uni-axial waveguide using metallic media is in the form of a single metal-dielectric interface. In this section, we will analyze the electromagnetic waves that can be sustained at a metal-dielectric interface by first assuming a general form of the electromagnetic fields. Application of boundary conditions to the waveguide will then yield a characteristic eigenvalue equation from which possible wavevector values, $\tilde{\beta}$, of the electromagnetic waves are mapped as a function of ω. The $\tilde{\beta}$-ω relationship is known as the dispersion relation of the waveguide.

To analyze a single metal-dielectric uni-axial waveguide, we consider the geometry of a semi-infinite metal occupying the region $z < 0$ and a semi-infinite dielectric occupying the region $z > 0$ as shown in Fig. 2.1. The metal is characterized by a local complex relative permittivity $\tilde{\epsilon}_2$, and the dielectric is characterized by a local generally-complex relative permittivity $\tilde{\epsilon}_1$. We

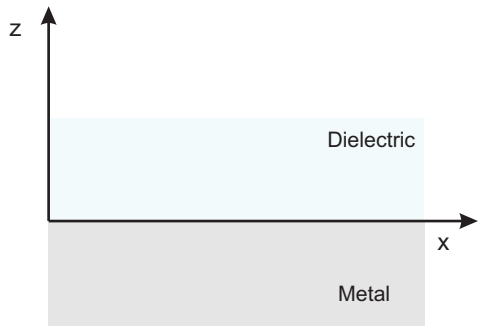

Figure 2.1: Single interface formed between a metal and dielectric.

assume a general form of the electromagnetic fields consisting of a transverse-magnetic (TM) polarized electromagnetic wave propagating along the $+x$-direction, which is given by

$$\tilde{H}_y(z) = \begin{cases} \tilde{H}_1 e^{i\tilde{\beta}x} e^{\tilde{k}_1 z} & z < 0 \\ \tilde{H}_2 e^{i\tilde{\beta}x} e^{-\tilde{k}_2 z} & z > 0, \end{cases} \tag{2.1}$$

$$\tilde{E}_x(z) = \begin{cases} \frac{-i\tilde{k}_1}{\omega\epsilon_o\tilde{\epsilon}_1} \tilde{H}_1 e^{i\tilde{\beta}x} e^{\tilde{k}_1 z} & z < 0 \\ \frac{i\tilde{k}_2}{\omega\epsilon_o\tilde{\epsilon}_2} \tilde{H}_2 e^{i\tilde{\beta}x} e^{-\tilde{k}_2 z} & z > 0, \end{cases} \tag{2.2}$$

and

$$\tilde{E}_z(z) = \begin{cases} \frac{-\tilde{\beta}}{\omega\epsilon_o\tilde{\epsilon}_1} \tilde{H}_1 e^{i\tilde{\beta}x} e^{\tilde{k}_1 z} & z < 0 \\ \frac{-\tilde{\beta}}{\omega\epsilon_o\tilde{\epsilon}_2} \tilde{H}_2 e^{i\tilde{\beta}x} e^{-\tilde{k}_2 z} & z > 0. \end{cases} \tag{2.3}$$

where $\tilde{k}_i (i = 1, 2)$ correspond to the exponential decay constants along the z-axis and $\tilde{\beta}$ is the wavevector. Wavevector of an electromagnetic wave

traveling with velocity, v and radial frequency, ω is defined as

$$\tilde{\beta} = \frac{\omega}{v}. \tag{2.4}$$

The decay length of the electromagnetic fields from the interface is given by

$$l_d = \frac{1}{|\tilde{k}_i|}. \tag{2.5}$$

Continuity of the tangential component of the electric field at $z = 0$ yields

$$-\frac{\tilde{k}_1 \tilde{H}_1}{\tilde{\epsilon}_1} = \frac{\tilde{k}_2 \tilde{H}_2}{\tilde{\epsilon}_2}. \tag{2.6}$$

Given continuity of the magnetic field at $z = 0$, we arrive at

$$\frac{\tilde{k}_1}{\tilde{k}_2} = -\frac{\tilde{\epsilon}_1}{\tilde{\epsilon}_2}. \tag{2.7}$$

Application of the general electromagnetic fields to the general wave equation yields

$$\tilde{k}_1^2 = \tilde{\beta}^2 - k_0^2 \tilde{\epsilon}_1 \tag{2.8}$$

and

$$\tilde{k}_2^2 = \tilde{\beta}^2 - k_0^2 \tilde{\epsilon}_2, \tag{2.9}$$

where k_0 is the free space wavevector. Applying Eqs. 2.8 and 2.9 to Eq. 2.7, we obtain the dispersion relation for a single metal-dielectric interface

$$\tilde{\beta} = k_0 \sqrt{\frac{\tilde{\epsilon}_1 \tilde{\epsilon}_2}{\tilde{\epsilon}_1 + \tilde{\epsilon}_2}}. \tag{2.10}$$

It is interesting to note that transverse electric (TE) polarized electromagnetic waves cannot be sustained at a single metal-dielectric interface. This can be shown using by first assuming a general form of TE-polarized electromagnetic fields given by

$$\tilde{E}_y(z) = \begin{cases} \tilde{E}_1 e^{i\tilde{\beta}x} e^{\tilde{k}_1 z} & z < 0 \\ \tilde{E}_2 e^{i\tilde{\beta}x} e^{-\tilde{k}_2 z} & z > 0, \end{cases} \tag{2.11}$$

$$\tilde{H}_x(z) = \begin{cases} \frac{i\tilde{k}_1}{\omega\epsilon_o} \tilde{E}_1 e^{i\tilde{\beta}x} e^{\tilde{k}_1 z} & z < 0 \\ \frac{-i\tilde{k}_2}{\omega\epsilon_o} \tilde{E}_2 e^{i\tilde{\beta}x} e^{-\tilde{k}_2 z} & z > 0, \end{cases} \tag{2.12}$$

and

$$\tilde{H}_z(z) = \begin{cases} \frac{\tilde{\beta}}{\omega\mu_o} \tilde{E}_1 e^{i\tilde{\beta}x} e^{\tilde{k}_1 z} & z < 0 \\ \frac{\tilde{\beta}}{\omega\mu_o} \tilde{E}_2 e^{i\tilde{\beta}x} e^{-\tilde{k}_2 z} & z > 0. \end{cases} \tag{2.13}$$

Continuity of $\tilde{E}_y$ and $\tilde{H}_x$ gives

$$\tilde{E}_1 = \tilde{E}_2 \tag{2.14}$$

and

$$\tilde{E}_1(\tilde{k}_1 + \tilde{k}_2) = 0. \tag{2.15}$$

For $\tilde{k}_1, \tilde{k}_2 > 0$ (required for finite-energy solutions), $\tilde{E}_1 = \tilde{E}_2 = 0$ is the only possible solution.

2.2 Uni-Axial Waveguide Composed of Metal-Dielectric-Metal Layers

We next consider a more complex uni-axial metallic waveguide consists of two metal-dielectric interfaces, formed by a dielectric layer sandwiched between two metal layers (forming a metal-dielectric-metal (MDM) waveguide). We will analyze the electromagnetic waves that can be sustained by MDM waveguides using analytical solutions to Maxwell's equations. Similar to the analysis used in the previous section, we assume a general form of the electromagnetic fields and apply boundary conditions to the fields to derive an eigenvalue equation.

Consider the geometry shown in Fig. 2.2 consisting of a lower metallic region occupying $z < -d$, a dielectric region occupying $-d < z < d$, and an upper metallic region occupying $z > d$. The lower metallic cladding layer is characterized by a local complex relative permittivity $\tilde{\epsilon}_1$, the dielectric is characterized by a local real relative permittivity ϵ_3, and the upper metallic cladding layer is characterized by a local complex relative permittivity $\tilde{\epsilon}_2$. We assume a general exponentially decaying form of the electromagnetic fields consisting of a transverse-magnetic (TM) polarized electromagnetic wave propagating along the $+x$-direction, which is given by

$$\tilde{H}_y(z) = \begin{cases} \tilde{H}_1 e^{i\tilde{\beta}x} e^{\tilde{k}_1 z} & z < -d \\ \tilde{H}_{31} e^{i\tilde{\beta}x} e^{\tilde{k}_3 z} + \tilde{H}_{32} e^{i\tilde{\beta}x} e^{-\tilde{k}_3 z} & -d < z < d \\ \tilde{H}_2 e^{i\tilde{\beta}x} e^{-\tilde{k}_2 z} & z > d. \end{cases} \tag{2.16}$$

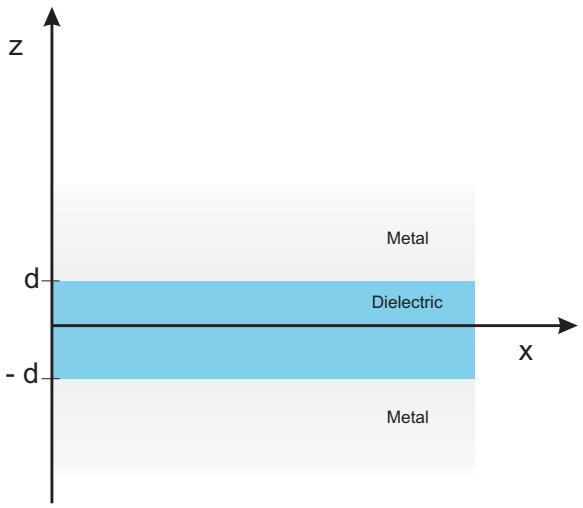

Figure 2.2: Geometry of a three-layered structure consisting of metallic cladding layers sandwiching a dielectric core.

$$\tilde{E}_x(z) = \begin{cases} \dfrac{-i}{\omega\epsilon_o\tilde{\epsilon}_1}\tilde{k}_1\tilde{H}_1 e^{i\tilde{\beta}x}e^{\tilde{k}_1 z} & z < -d \\ \dfrac{-ie^{i\tilde{\beta}x}\tilde{k}_3}{\omega\epsilon_o\epsilon_3}\tilde{H}_{31}e^{\tilde{k}_3 z} + \dfrac{-ie^{i\tilde{\beta}x}\tilde{k}_3}{\omega\epsilon_o\epsilon_3}\tilde{H}_{32}e^{-\tilde{k}_3 z} & -d < z < d \\ \dfrac{i}{\omega\epsilon_o\tilde{\epsilon}_2}\tilde{k}_2\tilde{H}_2 e^{i\tilde{\beta}x}e^{-\tilde{k}_2 z} & z > d. \end{cases} \quad (2.17)$$

and

$$\tilde{E}_z(z) = \begin{cases} \dfrac{-\tilde{\beta}}{\omega\epsilon_o\tilde{\epsilon}_1}\tilde{H}_1 e^{i\tilde{\beta}x}e^{\tilde{k}_1 z} & z < -d \\ \dfrac{-\tilde{\beta}}{\omega\epsilon_o\epsilon_3}\tilde{H}_{31}e^{i\tilde{\beta}x}e^{\tilde{k}_3 z} + \dfrac{-\tilde{\beta}}{\omega\epsilon_o\epsilon_3}\tilde{H}_{32}e^{i\tilde{\beta}x}e^{\tilde{k}_3 z} & -d < z < d \\ \dfrac{-\tilde{\beta}}{\omega\epsilon_o\tilde{\epsilon}_2}\tilde{H}_2 e^{i\tilde{\beta}x}e^{-\tilde{k}_2 z} & z > d. \end{cases} \quad (2.18)$$

Continuity of $\tilde{H}_y$ and $\tilde{E}_x$ at the boundaries $z = d$ and $z = -d$ yields the

relations

$$\tilde{H}_1 e^{-\tilde{k}_1 d} = \tilde{H}_{31} e^{-\tilde{k}_3 d} + \tilde{H}_{32} e^{\tilde{k}_3 d} \tag{2.19}$$

$$\frac{-\tilde{k}_1}{\tilde{\epsilon}_1} \tilde{H}_1 e^{-\tilde{k}_1 d} = \frac{-\tilde{k}_3}{\epsilon_3} \tilde{H}_{31} e^{-\tilde{k}_3 d} + \frac{\tilde{k}_3}{\epsilon_3} \tilde{H}_{32} e^{\tilde{k}_3 d}, \tag{2.20}$$

and

$$\tilde{H}_2 e^{-\tilde{k}_2 d} = \tilde{H}_{31} e^{\tilde{k}_3 d} + \tilde{H}_{32} e^{-\tilde{k}_3 d} \tag{2.21}$$

$$\frac{\tilde{k}_2}{\tilde{\epsilon}_2} \tilde{H}_2 e^{-\tilde{k}_2 d} = \frac{-\tilde{k}_3}{\epsilon_3} \tilde{H}_{31} e^{\tilde{k}_3 d} + \frac{\tilde{k}_3}{\epsilon_3} \tilde{H}_{32} e^{-\tilde{k}_3 d}. \tag{2.22}$$

Application of the generalized electromagnetic fields into the wave equation Eq. 1.29 and free space wavevector relation, $k_0 = \omega\sqrt{\mu_0 \epsilon_0}$ yields the relations

$$\tilde{k}_1^2 = \tilde{\beta}^2 - k_0^2 \tilde{\epsilon}_1, \tag{2.23}$$

$$\tilde{k}_2^2 = \tilde{\beta}^2 - k_0^2 \tilde{\epsilon}_2, \tag{2.24}$$

and

$$\tilde{k}_3^2 = \tilde{\beta}^3 - k_0^2 \epsilon_3. \tag{2.25}$$

Using Eqs.2.19, 2.21, 2.23, 2.24, and 2.25, we obtain the dispersion relation

$$e^{4\tilde{k}_3 d} = \frac{\tilde{k}_3/\epsilon_3 - \tilde{k}_1/\tilde{\epsilon}_1}{\tilde{k}_3/\epsilon_3 + \tilde{k}_1/\tilde{\epsilon}_1} \frac{\tilde{k}_3/\epsilon_3 - \tilde{k}_2/\tilde{\epsilon}_2}{\tilde{k}_3/\epsilon_3 + \tilde{k}_2/\tilde{\epsilon}_2} \quad . \tag{2.26}$$

Eq. 2.26 is a general relation and can be used for any three-layered waveguide in which $\tilde{\epsilon}_1 \neq \tilde{\epsilon}_2 \neq \epsilon_3$. For a symmetric structure with cladding layers

constructed using same material, $\tilde{\epsilon}_1 = \tilde{\epsilon}_2$ and $\tilde{k}_1 = \tilde{k}_2$, Eq.2.26 simplifies to

$$e^{4\tilde{k}_3 d} = \left(\frac{\tilde{k}_3/\epsilon_3 - \tilde{k}_1/\tilde{\epsilon}_1}{\tilde{k}_3/\epsilon_3 + \tilde{k}_1/\tilde{\epsilon}_1} \right)^2 . \tag{2.27}$$

Taking square root of both sides of Eq. 2.27 yields two families of solutions, one of which is symmetric and the other asymmetric. It can be shown that the negative solution of Eq. 2.27 gives the symmetric dispersion relation

$$e^{2\tilde{k}_3 d} = -\frac{\tilde{k}_3/\epsilon_3 - \tilde{k}_1/\tilde{\epsilon}_1}{\tilde{k}_3/\epsilon_3 + \tilde{k}_1/\tilde{\epsilon}_1}, \tag{2.28}$$

which can be re-expressed in the simple relation

$$\coth(\tilde{\mathrm{k}}_3 \mathrm{d}) = -\frac{\tilde{\mathrm{k}}_1 \epsilon_3}{\tilde{\mathrm{k}}_3 \tilde{\epsilon}_1}. \tag{2.29}$$

The asymmetric dispersion relation takes the form

$$e^{2\tilde{k}_3 d} = \frac{\tilde{k}_3/\epsilon_3 - \tilde{k}_1/\tilde{\epsilon}_1}{\tilde{k}_3/\epsilon_3 + \tilde{k}_1/\tilde{\epsilon}_1}, \tag{2.30}$$

or more simply

$$\coth(\tilde{\mathrm{k}}_3 \mathrm{d}) = -\frac{\tilde{\mathrm{k}}_3 \tilde{\epsilon}_1}{\tilde{\mathrm{k}}_1 \epsilon_3}. \tag{2.31}$$

2.3 Uni-Axial Waveguide Composed of an Arbitrary Number of Metal-Dielectric Layers

In this section, we derive a general dispersion relation for a uni-axial waveguide composed of an arbitrary number of metal-dielectric layers using

the transfer matrix method [40–42]. The description presented here follows similar to that of Verhaugen [42]. Consider the geometry shown in Fig 2.3. The geometry consists of n alternating layers of metal and dielectric. The general form of the magnetic fields in the bottom layer ($z < (z_2 = 0)$) and in the uppermost layer ($z > z_n$) is assumed as

$$\tilde{H}_{1y} = \tilde{H}_1 e^{i\tilde{\beta}x} e^{\tilde{k}_1 z}, \tag{2.32}$$

and

$$\tilde{H}_{ny} = \tilde{H}_n e^{i\tilde{\beta}x} e^{\tilde{k}_n (z_n - z)}, \tag{2.33}$$

respectively, where $\tilde{H}_1$ is the magnetic field at $z = z_2$ and $\tilde{H}_n$ is the magnetic field at $z = z_n$. Within an arbitrary layer j, the magnetic field is given by

$$\tilde{H}_{jy} = \tilde{H}_j(z) e^{i\tilde{\beta}x}. \tag{2.34}$$

Applying the general magnetic fields into the electromagnetic wave equation Eq. 1.29, we obtain following relation

$$\frac{\partial^2 \tilde{H}_j(z)}{\partial z^2} + (\tilde{k}_o^2 \tilde{\epsilon}_j - \tilde{\beta}^2)\tilde{H}_j(z) = 0. \tag{2.35}$$

The solution for the above equation is

$$\tilde{H}_j(z) = \tilde{C}_j \sin(\tilde{k}_j(z_j - z)) + \tilde{D}_j \cos(\tilde{k}_j(z_j - z)) \tag{2.36}$$

where

$$\tilde{k}_j = \sqrt{\tilde{\beta}^2 - k_o^2 \tilde{\epsilon}_j} \tag{2.37}$$

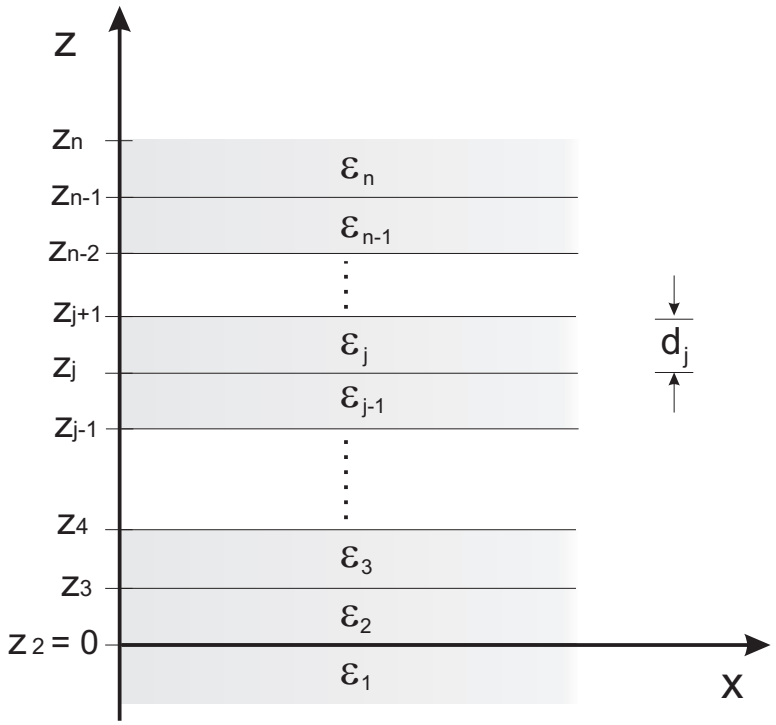

Figure 2.3: Uni-axial waveguide composed of an arbitrary number of metal-dielectric layers stacked along the z direction.

Differentiating Eq. 2.36 with respect to z yields

$$\frac{d}{dz}\tilde{H}_j(z) = -\tilde{C}_j\tilde{k}_j\cos(\tilde{k}_j(z_j - z)) + \tilde{D}_j\tilde{k}_j\sin(\tilde{k}_j(z_j - z)). \tag{2.38}$$

To determine the values of $\tilde{C}_j$ and $\tilde{D}_j$, we evaluate the magnetic field and its differential at $z = z_j$ to yield

$$\tilde{D}_j = \tilde{H}_j(z_j) \tag{2.39}$$

$$\tilde{C}_j = \frac{1}{\tilde{k}_j}\frac{d}{dz}\tilde{H}_j(z_j). \tag{2.40}$$

Inserting $\tilde{C_j}$ and $\tilde{D_j}$ into Eq. 2.36 and Eq. 2.38 yields

$$\begin{aligned} \tilde{H}_j(z) &= \frac{1}{\tilde{k}_j}\frac{d}{dz}\tilde{H}_j(z_j)\sin(\tilde{k}_j(z_j-z)) \\ &\quad +\tilde{H}_j(z_j)\cos(\tilde{k}_j(z_j-z)) \qquad (2.41) \\ \frac{d}{dz}\tilde{H}_j(z) &= -\frac{d}{dz}\tilde{H}_j(z_j)\cos(\tilde{k}_j(z_j-z)) \\ &\quad +\tilde{H}_j(z_j)\tilde{k}_j\sin(\tilde{k}_j(z_j-z)). \qquad (2.42) \end{aligned}$$

In matrix form, we can write Eq. 2.41

$$\begin{bmatrix} \tilde{H}_j(z) \\ \frac{d}{dz}\tilde{H}_j(z) \end{bmatrix} = \begin{bmatrix} \cos(\tilde{k}_j(z_j-z)) & \frac{1}{\tilde{k}_j}\sin(\tilde{k}_j(z_j-z)) \\ \tilde{k}_j\sin(\tilde{k}_j(z_j-z)) & -\cos(\tilde{k}_j(z_j-z)) \end{bmatrix} \begin{bmatrix} \tilde{H}_j(z_j) \\ \frac{d}{dz}\tilde{H}_j(z_j) \end{bmatrix}. \qquad (2.43)$$

The corresponding electric fields are given by

$$\begin{aligned} \tilde{E}_{jx} &= -\frac{i}{\omega\epsilon_o\tilde{\epsilon}_j}e^{i\tilde{\beta}x}\frac{d}{dz}\tilde{H}_j(z) \qquad (2.44) \\ \tilde{E}_{jz} &= -\frac{\tilde{\beta}}{\omega\epsilon_o\tilde{\epsilon}_j}e^{i\tilde{\beta}x}\tilde{H}_j(z). \qquad (2.45) \end{aligned}$$

Applying boundary conditions for the tangential components of the electric and magnetic field at the arbitrary interface $z = z_j$ yields

$$\tilde{H}_j(z_j) = \tilde{H}_{j-1}(z_j) \qquad (2.46)$$

and

$$\tilde{E}_{jx} = \tilde{E}_{(j-1)x}$$

$$\begin{aligned} \frac{1}{\tilde{\epsilon}_j}\frac{d}{dz}\tilde{H}_j(z_j) &= \frac{1}{\tilde{\epsilon}_{j-1}}\frac{d}{dz}\tilde{H}_j(z_{j-1}) \\ \frac{d}{dz}\tilde{H}_j(z_j) &= \frac{\tilde{\epsilon}_j}{\tilde{\epsilon}_{j-1}}\frac{d}{dz}\tilde{H}_{j-1}(z_j), \end{aligned} \tag{2.47}$$

which can be re-expressed in matrix form as

$$\begin{bmatrix} \tilde{H}_j(z_j) \\ \frac{d}{dz}\tilde{H}_j(z_j) \end{bmatrix} = \begin{bmatrix} 1 & 0 \\ 0 & \frac{\tilde{\epsilon}_j}{\tilde{\epsilon}_{j-1}} \end{bmatrix} \begin{bmatrix} \tilde{H}_{j-1}(z_j) \\ \frac{d}{dz}\tilde{H}_{j-1}(z_j) \end{bmatrix}. \tag{2.48}$$

At the interface $z = z_{j+1}$, from Eq. 2.43

$$\begin{bmatrix} \tilde{H}_j(z_{j+1}) \\ \frac{d}{dz}\tilde{H}_j(z_{j+1}) \end{bmatrix} = \begin{bmatrix} \cos(\tilde{k}_j(d_j)) & \frac{1}{\tilde{k}_j}\sin(\tilde{k}_j(d_j)) \\ \tilde{k}_j\sin(\tilde{k}_j(d_j)) & -\cos(\tilde{k}_j(d_j)) \end{bmatrix} \begin{bmatrix} \tilde{H}_j(z_j) \\ \frac{d}{dz}\tilde{H}_j(z_j) \end{bmatrix}$$

where $d_j = z_{j+1} - z_j$ is the thickness of the jth layer. Putting values from Eq. 2.48 into the above equation

$$\begin{bmatrix} \tilde{H}_j(z_{j+1}) \\ \frac{d}{dz}\tilde{H}_j(z_{j+1}) \end{bmatrix} = \tilde{T}_j \begin{bmatrix} \tilde{H}_{j-1}(z_j) \\ \frac{d}{dz}\tilde{H}_{j-1}(z_j) \end{bmatrix}$$

where

$$\tilde{T}_j = \begin{bmatrix} \cos(\tilde{k}_j(d_j)) & \frac{1}{\tilde{k}_j}\sin(\tilde{k}_j(d_j)) \\ \tilde{k}_j\sin(\tilde{k}_j(d_j)) & -\cos(\tilde{k}_j(d_j)) \end{bmatrix} \begin{bmatrix} 1 & 0 \\ 0 & \frac{\tilde{\epsilon}_j}{\tilde{\epsilon}_{j-1}} \end{bmatrix}. \tag{2.49}$$

The magnetic field in layer 1 is given by Eq. 2.32. Using Eq. 2.48, we can

relate the magnetic field at interface z_3 with the field in layer 1 by

$$\begin{bmatrix} \tilde{H}_2(z_3) \\ \frac{d}{dz}\tilde{H}_2(z_3) \end{bmatrix} = \tilde{T_2} \begin{bmatrix} \tilde{H}_1 \\ k_1\tilde{H}_1 \end{bmatrix}. \tag{2.50}$$

Similarly, the field at interface z_3 can be related to the field at interface z_2 by

$$\begin{bmatrix} \tilde{H}_3(z_4) \\ \frac{d}{dz}\tilde{H}_3(z_4) \end{bmatrix} = \tilde{T_3} \begin{bmatrix} \tilde{H}_2(z_3) \\ \frac{d}{dz}\tilde{H}_2(z_3) \end{bmatrix}.$$

From above two relations, we can relate the field in layer 3 at interface z_4 with the field in layer 1 by

$$\begin{bmatrix} \tilde{H}_3(z_4) \\ \frac{d}{dz}\tilde{H}_3(z_4) \end{bmatrix} = \tilde{T_3}\tilde{T_2} \begin{bmatrix} \tilde{H}_1(z_2) \\ \tilde{k}_1 H_1(z_2) \end{bmatrix}. \tag{2.51}$$

In general, we can relate the field in layer $j-1$ at interface z_j with the field in layer 1 by

$$\begin{bmatrix} \tilde{H}_{j-1}(z_j) \\ \frac{d}{dz}\tilde{H}_{j-1}(z_j) \end{bmatrix} = \tilde{T_{j-1}}\tilde{T_{j-2}}...\tilde{T_2} \begin{bmatrix} \tilde{H}_1(z_2) \\ \tilde{k}_1\tilde{H}_1(z_2) \end{bmatrix}. \tag{2.52}$$

Further, we can relate the field in layer j at interface z_j with the field in layer 1 using relation 2.48 by

$$\begin{bmatrix} \tilde{H}_j(z_j) \\ \frac{d}{dz}\tilde{H}_j(z_j) \end{bmatrix} = \tilde{V_j}\tilde{T_{j-1}}\tilde{T_{j-2}}...\tilde{T_2} \begin{bmatrix} \tilde{H}_1(z_2) \\ \tilde{k}_1\tilde{H}_1(z_2) \end{bmatrix} \tag{2.53}$$

where

$$\tilde{V_j} = \begin{bmatrix} 1 & 0 \\ 0 & \frac{\tilde{\epsilon}_j}{\tilde{\epsilon}_{j-1}} \end{bmatrix}.$$

We now define the quantity

$$\begin{aligned} \tilde{W_j} &= \tilde{V_j}\tilde{T_{j-1}}\tilde{T_{j-2}}...\tilde{T_2} \\ &= \begin{bmatrix} \tilde{W_{11}} & \tilde{W_{12}} \\ \tilde{W_{21}} & \tilde{W_{22}} \end{bmatrix}. \end{aligned}$$

We can now relate the fields at interface $z_2 = 0$ with fields at interface $z = z_n$ by

$$\begin{bmatrix} \tilde{H}_n(z_n) \\ -\tilde{k}_n\tilde{H}_n(z_n) \end{bmatrix} = \tilde{W_j} \begin{bmatrix} \tilde{H}_1(0) \\ \tilde{k}_1\tilde{H}_1(0) \end{bmatrix}. \tag{2.54}$$

The above matrix can be resolved into the simplified equation

$$\tilde{W_{11}} + \tilde{W_{12}}\tilde{k}_1 + \frac{\tilde{W_{21}}}{\tilde{k}_n} + \tilde{W_{22}}\frac{\tilde{k}_1}{k_n} = 0. \tag{2.55}$$

Equation 2.55 is a general dispersion relation for a multi-layered uni-axial waveguide structure. The solutions to Eq. 2.55 are complex wavevector values $\tilde{\beta}$.

2.4 Davidenko Method

The analytically-derived dispersion relations obtained in the previous sections for various types of uni-axial metallic waveguides contain the necessary information to understand the flow of electromagnetic waves within the

waveguides. The complexity of the dispersion relation depends in large part on the complexity of the waveguide geometry. The dispersion relation for a single metal-dielectric interface is an explicit expression, but the dispersion relation for multi-layered structures is an implicit, complex, transcendental equation. In this section, we introduce a robust iterative method to solve complex transcendental equations [43]. The method is commonly ascribed to Davidenko [44–46].

The Davidenko method is widely used for solving transcendental equations that cannot otherwise be solved using traditional methods such as Newton's method and quasi-Newton methods [47]. The Davidenko method can be understood by first considering the equation

$$f(x) = 0, \tag{2.56}$$

which has a solution determined by the Newton's method as

$$x_{n+1} = x_n - \frac{f(x_n)}{df(x_n)/dx}. \tag{2.57}$$

We can modify Eq. 2.57 to yield

$$\frac{df(x_n)}{dx} = \frac{0 - f(x_n)}{x_{n+1} - x_n}. \tag{2.58}$$

Eq. 2.58 describes a straight line in which the next iteration point x_{n+1} lies at the intersection of this straight line with tangent to the function $f(x_n)$. This restricts the initial guess to lie in an area that is sufficiently near the actual solution. This condition can be relaxed by inserting a factor, t, such

that

$$\frac{df(x_n)}{dx} = -t\frac{0 - f(x_n)}{x_{n+1} - x_n} \tag{2.59}$$

where $0 < t < 1$. Equation 2.59 can be rearranged, using $\Delta x_n = x_{n+1} - x_n$, to give

$$\frac{\Delta x_n}{t} = -\frac{f(x_n)}{df(x_n)/dx}. \tag{2.60}$$

In the limit $t \to 0$, Δx_n transforms into a differential. We can assume that $f(x)$ remains continuous in the small area near x_n, yielding

$$\begin{aligned} \frac{dx}{dt} &= -\frac{f(x)}{df/dx} \\ &= -\frac{1}{\frac{df}{dx}\left(\frac{1}{f(x)}\right)} \\ &= -\frac{1}{d(ln(f(x)))/dx}. \end{aligned} \tag{2.61}$$

The solution of Eq. 2.61 is given by

$$f(x) = Ce^{-t(x)}, \tag{2.62}$$

where C is the integration constant. Equation 2.62 suggests that $f(x) = 0$ is a limiting case when $t \to \infty$. The differential equation can also be transformed in terms of a Jacobian operator J as

$$\frac{dx}{dt} = -J^{-1}f(x). \tag{2.63}$$

This relation is the basic form of Davidenko method. We can use the Davidenko method to solve the dispersion relation for various uni-axial metallic

waveguides. We can write the general dispersion relation as

$$F(\omega;\tilde{\beta}) = 0, \tag{2.64}$$

where the wavevector $\tilde{\beta}$ is a complex quantity and can be written in its real and imaginary components as

$$\beta = a + ib. \tag{2.65}$$

In other words, we can write the dispersion relation 2.64 as

$$F(\omega;a,b) = 0. \tag{2.66}$$

We can resolve Eq. 2.66 into two sets of equations given by

$$R(\omega;a,b) = Re[F(\omega;a,b)] = 0 \tag{2.67}$$

$$I(\omega;a,b) = Im[F(\omega;a,b)] = 0. \tag{2.68}$$

Because the dispersion relation is a complex analytical function, we can express the Jacobian operator and its inverse in closed form. The dispersion relation then satisfies the Cauchy-Riemann relations

$$\begin{aligned} \frac{\partial R}{\partial a} &= \frac{\partial I}{\partial b} \\ R_a &= I_b \end{aligned} \tag{2.69}$$

and

$$\begin{aligned} \frac{\partial R}{\partial b} &= -\frac{\partial I}{\partial a} \\ R_b &= -I_a. \end{aligned} \tag{2.70}$$

From the property of analytical functions, we have

$$\begin{aligned} F_\beta = \frac{\partial F}{\partial \beta} &= R_a + jI_a \\ &= R_a - jR_b, \end{aligned} \tag{2.71}$$

which yields

$$R_a = \frac{\partial R}{\partial a} = Re[F_\beta] \tag{2.72}$$

$$R_b = \frac{\partial R}{\partial b} = -Im[F_\beta]. \tag{2.73}$$

The Jacobian matrix in this case will be

$$J = \begin{bmatrix} R_a & R_b \\ I_a & I_b \end{bmatrix}. \tag{2.74}$$

Using Eqs. 2.69 and 2.70, the Jacobian matrix becomes

$$J = \begin{bmatrix} R_a & R_b \\ -R_b & R_a \end{bmatrix}. \tag{2.75}$$

To obtain the inverse Jacobian matrix, we first get the determinant of

Eq. 2.75 by

$$\mathrm{detJ} = \mathrm{R_a^2} + \mathrm{R_b^2} = |\mathrm{F}_\beta|^2, \tag{2.76}$$

which yields the inverse Jacobian matrix

$$\begin{aligned} J^{-1} &= \frac{1}{detJ}\begin{bmatrix} R_a & -R_b \\ R_b & R_a \end{bmatrix} \\ &= \frac{1}{|F_\beta|^2}\begin{bmatrix} Re[F_\beta] & Im[F_\beta] \\ -Im[F_\beta] & Re[F_\beta]. \end{bmatrix}. \end{aligned} \tag{2.77}$$

Now we can write the Davidenko equation for the general dispersion relation as

$$\frac{d}{dt}\begin{bmatrix} a \\ b \end{bmatrix} = -J^{-1}\begin{bmatrix} R \\ I \end{bmatrix}.$$

Putting the value of the inverse Jacobian matrix yields

$$\frac{d}{dt}\begin{bmatrix} a \\ b \end{bmatrix} = -\frac{1}{|F_{\tilde{\beta}}|^2}\begin{bmatrix} Re[F_{\tilde{\beta}}] & Im[F_{\tilde{\beta}}] \\ -Im[F_{\tilde{\beta}}] & Re[F_{\tilde{\beta}}]. \end{bmatrix}\begin{bmatrix} R \\ I \end{bmatrix}. \tag{2.78}$$

From Eq. 2.78, we can obtain separate real, ordinary differential equations for the real and imaginary parts of the wavevector

$$\frac{da}{dt} = -\frac{1}{|F_{\tilde{\beta}}|^2}(Re[F]Re[F_{\tilde{\beta}}] + Im[F]Im[F_{\tilde{\beta}}]), \tag{2.79}$$

and

$$\frac{db}{dt} = \frac{1}{|F_{\tilde{\beta}}|^2}(Re[F]Im[F_{\tilde{\beta}}] + Im[F]Re[F_{\tilde{\beta}}]), \tag{2.80}$$

which are considerably easier to solve than the original complex transcen-

dental equation.

2.5 Summary

In this chapter, we have explored interaction of electromagnetic waves with uni-axial metallic waveguides and derived characteristic equations that yield the dispersion relations for different waveguide geometries. The Davidenko method has been introduced and will be used throughout the remainder of the thesis to solve complex transcendental equations corresponding to the dispersion relations for various uni-axial metallic waveguides. We will next develop a method to design multi-axial waveguides by conceptually de-composing the structures into simpler uni-axial waveguide components. The dispersion relations for uni-axial waveguides will then be used to approximate the electromagnetic wave behaviour in different sections of the multi-axial waveguide.

Chapter 3

Multi-Axial Nanoscale Light Bending

Multi-axial waveguides are structures that guide light along more than one direction. Modeling multi-axial waveguides is challenging because the electromagnetic waves sustained within these structure are no longer characterized by a single wavevector. Designing multi-axial waveguides generally requires numerical techniques, such as the FDTD method, to model the multi-axial flow of electromagnetic waves within the structure. Numerical simulations, however, are both computationally expensive and time-consuming. Because only one set of parameters can be modeled in a given simulation, full characterization and optimization of the waveguide using a numerical simulation tool only, is often not feasible.

In this and coming sections, an analytical technique for designing a multi-axial waveguide designing technique is investigated. The technique is based on conceptually dividing a multi-axial waveguide into uni-axial waveguide

---

Adapted and reprinted with permission from M. W. Maqsood, R. Mehfuz, and K. J. Chau, "Design and optimization of a high-efficiency nanoscale ±90° light-bending structure by mode selection and tailoring," Applied Physics Letters **97**, 151111 (2010), American Institute of Physics.

sub-components. Solving the dispersion relations of the uni-axial waveguide components then enables approximation of the electromagnetic wave behaviour in different sections of the multi-axial waveguide. By tailoring the geometry of the uni-axial waveguide sub-components so that each of them sustain a single propagative mode with matched electromagnetic wavevectors, efficient coupling between different sections of the multi-axial waveguide is predicted. The predictions made using this simple analytical approach are confirmed using rigorous numerical simulations.

In recent years, there has been a growing interest in the development of light steering structures for application in dense integrated optical systems. Achieving efficient light bending over sharp corners is generally challenging due to bending losses - a general term that describes the propensity of light to scatter and escape into free-space when curvature of a waveguide bend is very small. Recently, several different approaches have been put forward which use dielectric waveguide resonators [48, 49] and dielectric photonic crystals [50] placed at the intersection of two waveguides, to achieve bending over 90°. An alternative method is to use waveguides composed of metals. One such implementation is based on joining two nanoscale metal-dielectric-metal (MDM) waveguides at 90° [51–53] to form either an L or a T-junction. When the thickness of dielectric core in these structures is reduced such that it is smaller than the wavelength of the incident light, the waveguides sustain only the lowest-order TM mode, TM_0 mode (commonly referred as the surface plasmon polariton (SPP) mode), which travels along the metal surface and around the waveguide bend. There are a few limitations with this implementation. TM_0 modes are highly dissipative and can

only propagate over a few microns at visible frequencies. Furthermore, there is significant back scattering of the TM_0 mode when it encounters the bend. Back scattering can be somewhat reduced by converting the bend into a curve. Even with curved bends, waveguide bends based on SPP modes have limited efficiency. A maximum bending efficiency of 77% has been reported for a metallic waveguide bend with a bending curvature radius of 20 nm at a free-space wavelength of 632 nm [52].

3.1 Material and Geometry Selection

Here, we will explore a bi-axial, metallic, nanometer scale waveguide designed to bend light with high efficiency and low loss over right angles. We start by selecting the constituent materials of the waveguide. At visible frequencies, silver is the most suitable choice for the metal component, as indicated by the small magnitude of the imaginary part of its permittivity. For the dielectric component, we want to select a material that has low loss yet has a high refractive index to reduce the effective wavelength of light in the structure. With this in mind, we select gallium phosphide (GaP) which is nearly transparent in the visible region and has a mostly real refractive index $n \simeq 3.5$.

We first consider a basic multi-axial T-junction waveguide geometry as shown in Fig. 3.1. The waveguide consists of semi-infinite silver metal film with a slit in the center. The slit is filled with GaP and the complete structure is covered with GaP. The waveguide structure is illuminated from the bottom with a TM-polarized light at a frequency ω and wavelength

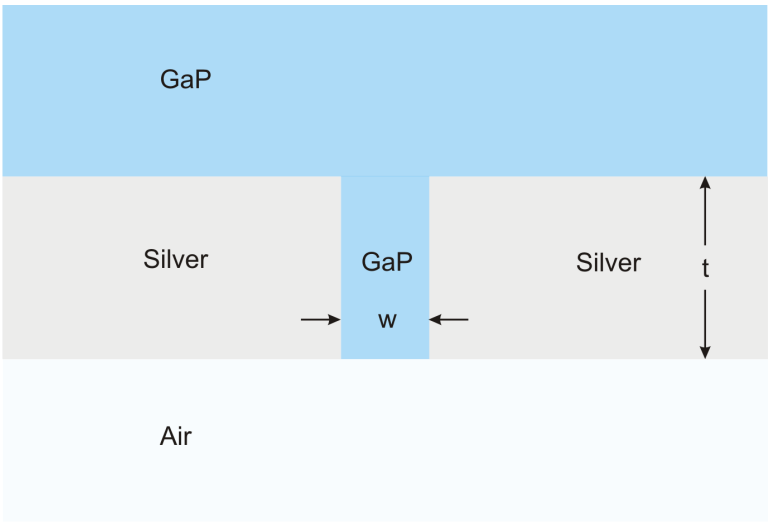

Figure 3.1: Waveguide structure consisting of a silver slit filled with GaP, with the complete structure covered with a semi-infinite GaP layer. GaP is chosen due to its higher refractive index of $n = 3.5$.

λ. For analysis, the region before the bend is approximated as an infinite metal-dielectric-metal (MDM) waveguide and region after the bend is approximated as single metal-dielectric waveguide. In this case, the MDM waveguide is composed of a GaP core surrounded by silver cladding layers and the metal-dielectric waveguide is composed of an interface between silver and GaP.

3.2 Mode Selection

We analyze the propagation of an electromagnetic wave in the waveguide regions by approximating each region as an independent uni-axial waveguide. The modes sustained by each of the uni-axial waveguides are mapped

out to describe the propagation characteristics of the wave inside different parts of the waveguide. A mode is a confined electromagnetic wave which is described by a distinctive wavevector value at a given frequency. This wavevector value corresponds to transverse field amplitudes that are independent of the mode propagation. For a given waveguide geometry only a finite number of modes are allowable and out of these only some are propagative. The distinction between a propagative and non-propagative mode is made through the figure-of-merit (FOM) given by

$$\text{FOM} = \frac{Re(\tilde{\beta})}{Im(\tilde{\beta})}. \tag{3.1}$$

A mode is considered propagative if it can propagate at least one complete cycle. This condition is achieved when FOM $> 2\pi$. Using eigenvalue equations derived in Chapter 2 and the Davidenko method, we obtain values of the complex wavevector, $\tilde{\beta}$, for the uni-axial waveguides. From $\tilde{\beta}$, we calculate FOM curves for the waveguides and identify the propagative modes having FOM $> 2\pi$.

We first consider the lowest order asymmetric SPP mode (also known as the TM_0 mode) sustained by the uni-axial MDM waveguide section. Using the asymmetric form of the dispersion relation obtained in Eq. 2.30 and experimental data of Johnson and Christy [36] for silver, complex wavevector values are numerically evaluated for the lowest order mode. Figure 3.2 depicts $Re(\tilde{\beta})$ and FOM curves for the asymmetric SPP mode sustained by a silver-GaP-silver waveguide for slit width values varying from $w = 10$ nm to $w = 300$ nm. The $Re(\tilde{\beta})$ curves have an inflection point near 5.5×10^{14}

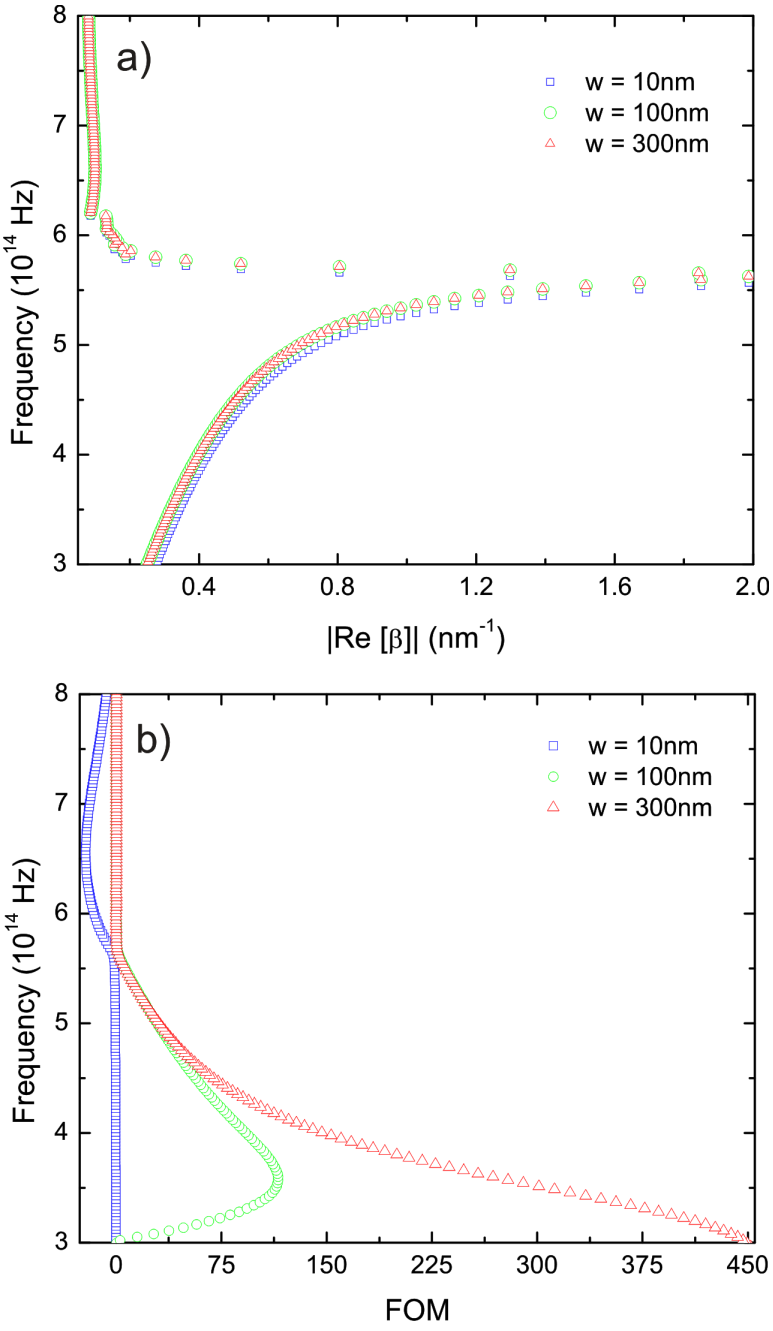

Figure 3.2: Dispersion curves for the asymmetric SPP modes sustained by an MDM (Ag-GaP-Ag) waveguide. a) Real part of the wavevector and b) figure of merit (FOM) as a function of frequency for various dielectric core thickness values.

Hz, a frequency known as the surface plasmon resonance frequency. At the surface plasmon resonance frequency, the magnitude of the real part of the relative permittivity of the metal and dielectric are equivalent and, as a result, $Re(\tilde{\beta})$ becomes large. From the FOM curves, the asymmetric mode is generally only propagative for frequencies below the surface plasmon resonance frequency. It is interesting to note that for the smallest slit width ($w = 10$ nm) and at UV frequencies above the surface plasmon resonance frequency, the asymmetric SPP mode is propagative with a negative FOM. This describes a backwards-propagating mode which has a phase velocity oriented in the opposite direction to the energy velocity.

We next consider the lowest order symmetric SPP mode (also known as the TM_0 mode) sustained by the MDM waveguide section. Using the symmetric form of the dispersion relation obtained in Eq. 2.28 and experimental data of Johnson and Christy [36] for silver, complex wavevector values are numerically evaluated for the lowest order mode. The $Re(\tilde{\beta})$ and FOM curves for the symmetric mode are presented in Figure 3.3 for slit width values varying from $w = 10$nm to $w = 300$nm. Again, the $Re(\tilde{\beta})$ curves are characterized by an inflection point at a surface plasmon resonance frequency which matches that of the asymmetric SPP mode. The FOM values of the symmetric SPP mode approach zero near the resonance frequency. Below this frequency, the symmetric SPP mode is propagative with FOM values exceeding those of the asymmetric SPP mode. Based on the relative FOM values of the symmetric and asymmetric SPP modes throughout the explored frequency interval, we conclude that the symmetric SPP mode is dominant over the asymmetric SPP mode.

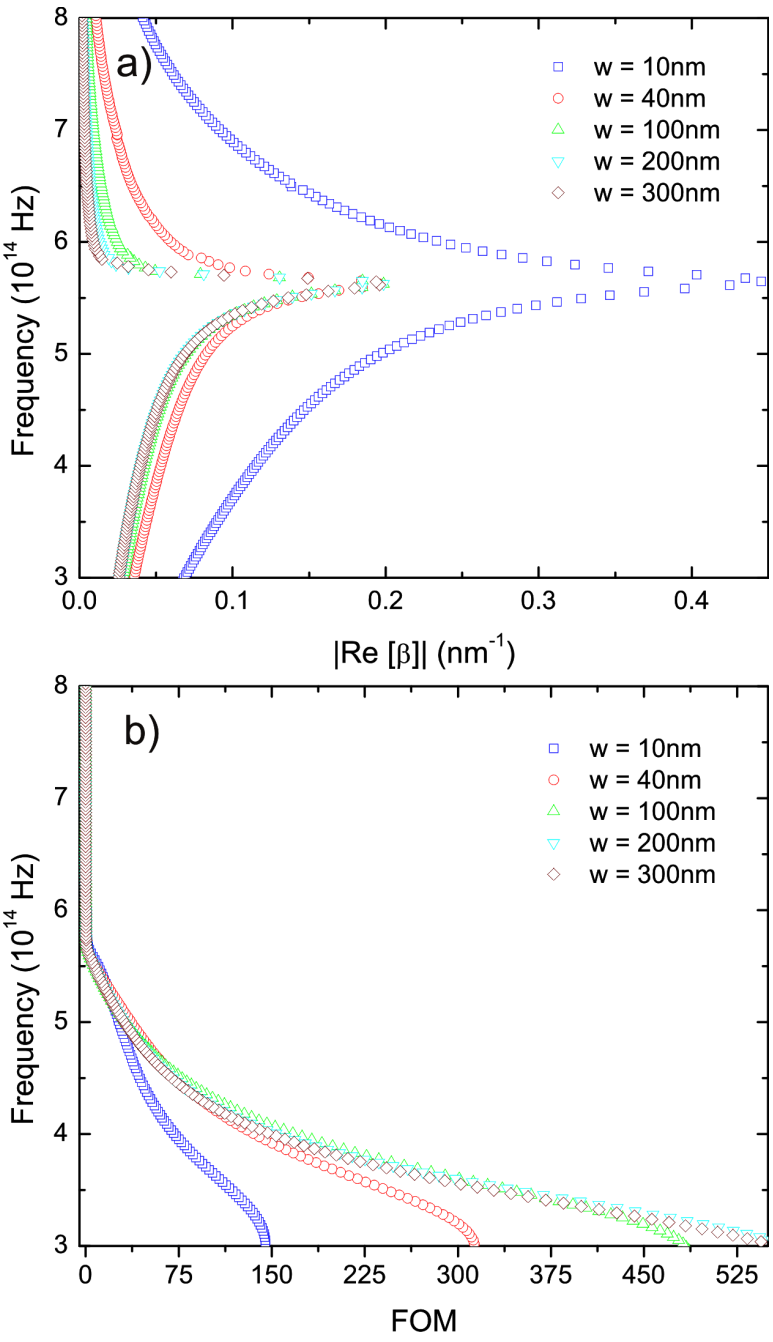

Figure 3.3: Dispersion curves for the symmetric SPP modes sustained by an MDM (Ag-GaP-Ag) waveguide. a) Real part of the wavevector and b) figure of merit (FOM) as a function of frequency for various dielectric core thickness values.

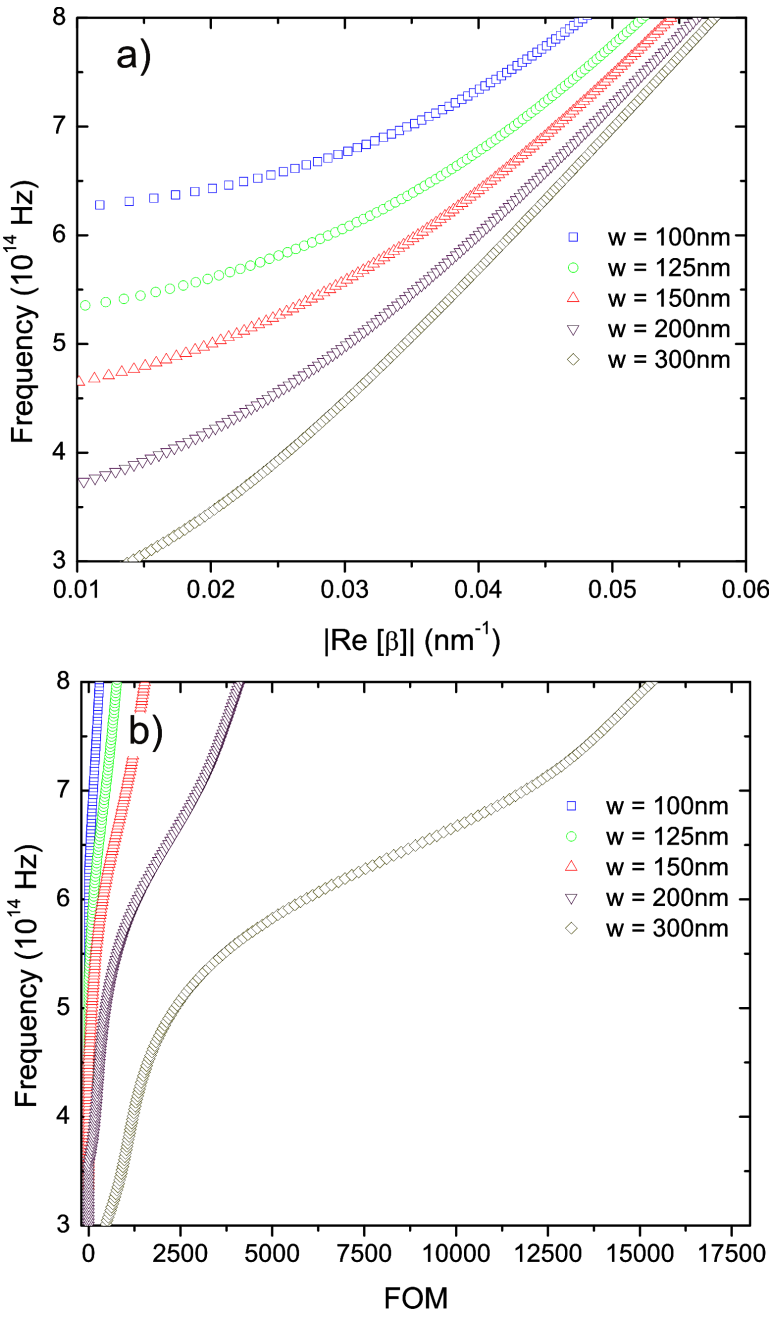

Figure 3.4: Dispersion curves for the TM_1 modes sustained by an MDM (Ag-GaP-Ag) waveguide. a) Real part of the wavevector and b) figure of merit (FOM), as a function of frequency for various dielectric core thickness values.

We finally consider the first order symmetric TM mode sustained by the MDM waveguide section, labeled as the TM_1 mode. Using the symmetric form of the dispersion relation obtained in Eq. 2.28 and experimental data of Johnson and Christy [36] for silver, complex wavevector values are numerically evaluated for the second-lowest order mode. Figure 3.4 depicts the $Re(\tilde{\beta})$ and FOM curves for TM_1 modes sustained by the MDM waveguide for varying slit width values from $w = 10$nm to $w = 300$nm. Unlike the SPP modes, the $Re(\tilde{\beta})$ curve of the TM_1 mode is characterized by a cutoff frequency - a frequency below which the wavevector value vanishes - and $Re(\tilde{\beta})$ values that monotonically increase as a function of frequency. Near the surface plasmon resonance frequency, the FOM values of the TM_1 mode are significantly larger than the FOM values of the SPP modes. For visible frequencies near and above the surface plasmon resonance frequency, the relative large FOM values of the TM_1 mode as compared to the symmetric and asymmetric SPP modes means that the TM_1 mode is the dominant mode.

Next we analyze the modes sustained by the silver-GaP interface by approximating the interface as an uni-axial metal-dielectric waveguide section. As discussed in Chapter 2, a uni-axial waveguide composed of a metal-dielectric interface can sustain only a single SPP mode. The $Re(\tilde{\beta})$ and FOM curves for the SPP mode are depicted in Figure 3.5. Similar to the case of SPP mode in the MDM waveguide, the $Re(\tilde{\beta})$ for the SPP mode at the metal dielectric interface is characterized by an inflection point at the surface plasmon resonance frequency 5.5×10^{14} Hz. The SPP mode is propagative below the surface plasmon resonance frequency and non-propagative

above it.

Based on our analysis, a nanometer-scale GaP-filled slit in a silver film coated with a semi-infinite GaP layer can potentially sustain four types of modes. In the GaP-filled slit section of the structure, three modes are possible: asymmetric and symmetric SPP modes and the first order TM_1 mode (it can be shown that the higher order TM modes are all cutoff). Of these three modes, the TM_1 mode is desirable because it has the largest FOM values, which are achieved at higher frequencies above both the surface plasmon resonance frequency and the cutoff frequency. In the silver-GaP section of the structure, only the SPP mode is allowable, which is propagative below the surface plasmon resonance frequency and non-propagative above it. At lower frequencies where the SPP mode is propagative, the TM_1 mode is cutoff and at higher frequencies where the TM_1 mode in the slit section is dominant, the SPP mode at the metal interface becomes non-propagative. Thus the SPP mode of the silver-GaP interface is not compatible with the TM_1 mode of the GaP-filled slit.

3.3 Modified Bi-Axial Waveguide Structure

We next modify the structure so that the GaP layer on the metal film has a finite thickness, with a dielectric region on top of the GaP layer consisting of air. The resulting structure is shown in Figure 3.6. To analyze this modified structure, the region on top of the metal film is approximated as a uni-axial metal-dielectric-dielectric (MDD) waveguide composed of a silver cladding, a GaP core, and an air cladding. This MDD waveguide is

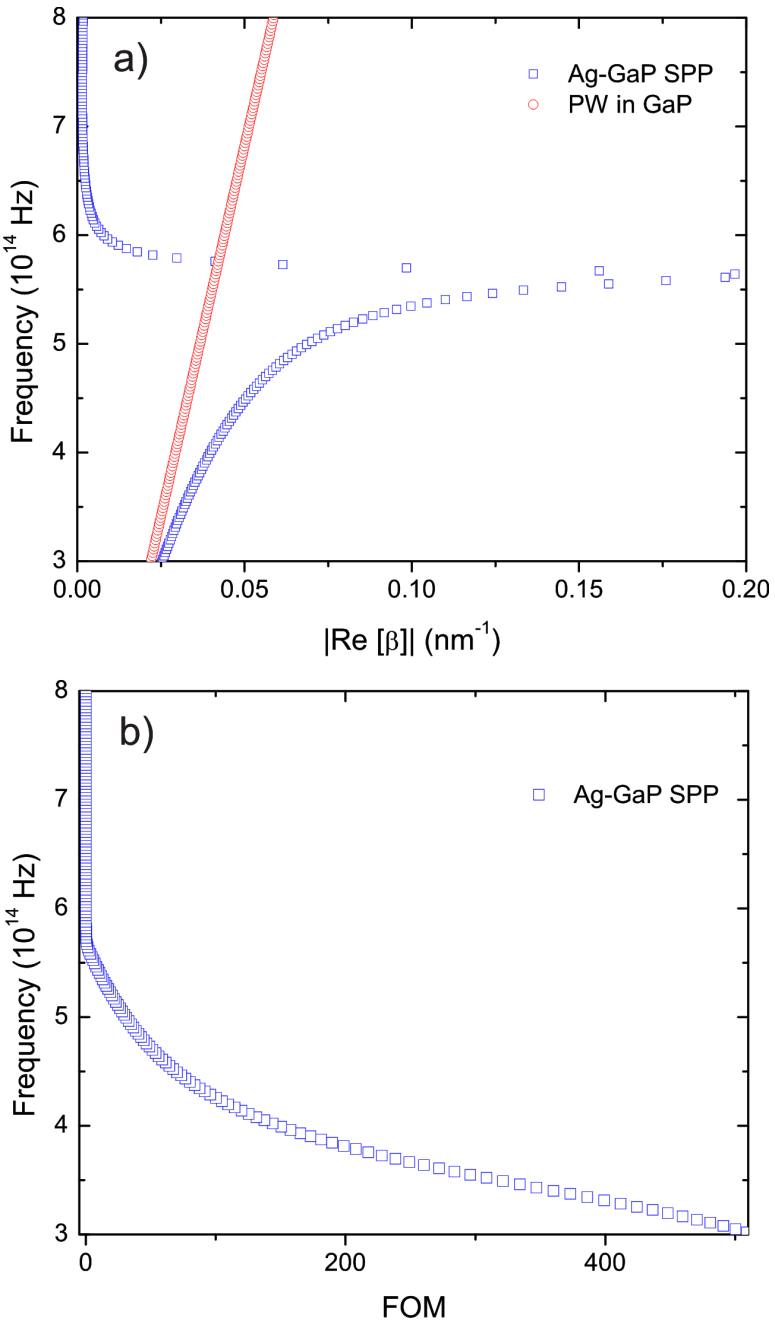

Figure 3.5: Dispersion curves for the SPP mode sustained by a Ag-GaP interface. a) Real part of the wavevector and b) figure of merit (FOM) as a function of frequency.

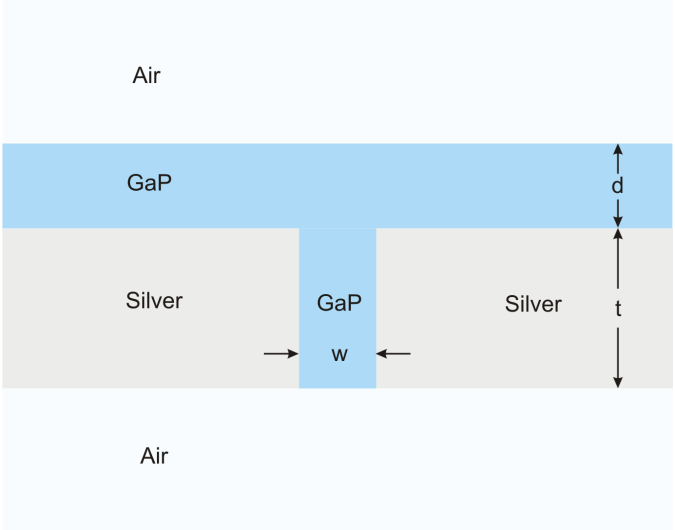

Figure 3.6: Waveguide structure consisting of a slit in a silver film where the slit is filled with GaP and the entire silver film is coated with a GaP layer of finite thickness. The structure is immersed in air.

advantageous to a metal-dielectric waveguide because the MDD waveguide can sustain higher-order TM modes in addition to the SPP mode. Figure 3.7 shows the $Re(\tilde{\beta})$ and FOM curves for the SPP mode, and the first-order TM_1 mode sustained by an MDD waveguide for core thickness values ranging from 100nm to 300nm (the higher-order TM modes are cutoff for these core thickness values). Similar to the trends observed for other SPP modes, the SPP mode in the MDD waveguide is only propagative below the surface plasmon resonance frequency, 5.5×10^{14} Hz. As before, this SPP mode is not compatible with the TM_1 mode in the MDM waveguide. The TM_1 mode of the MDD waveguide, on the other hand, is compatible with the TM_1 mode in the MDM waveguide because both TM_1 modes are propagative at frequencies above the surface plasmon resonance frequency. Based on

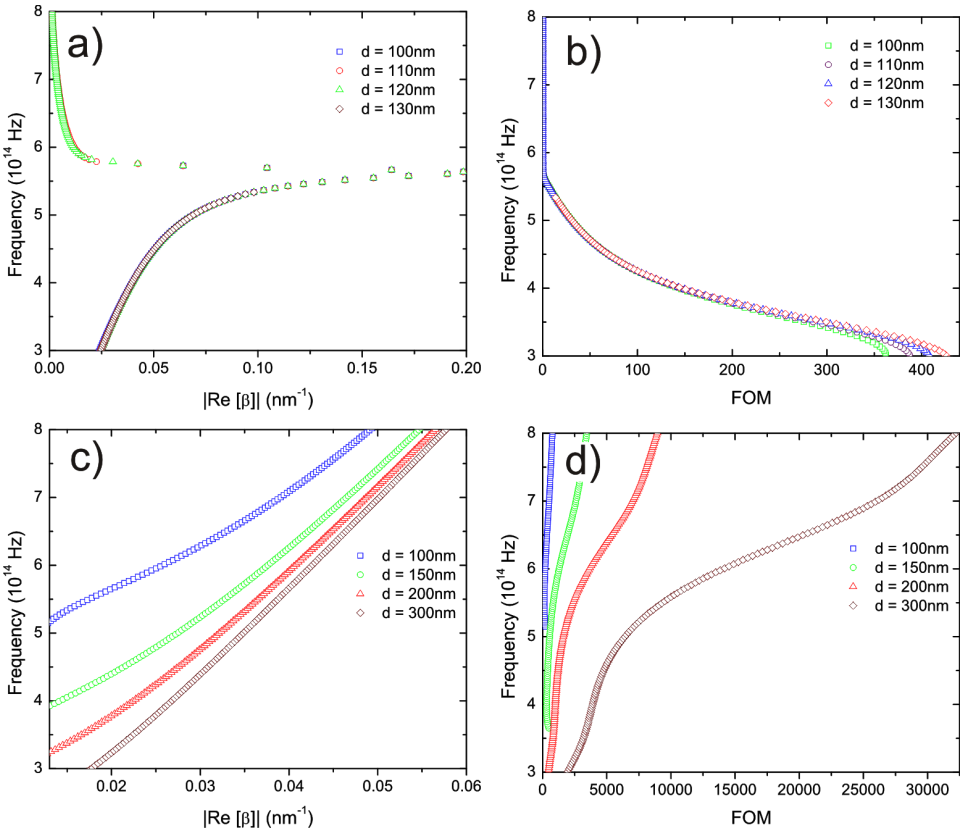

Figure 3.7: Modal solution for an MDD (Ag-GaP-Air) waveguide. a) Real part of the wavevector and b) figure of merit (FOM) as a function of frequency for the SPP mode. c) Real part of the wavevector and d) figure of merit (FOM) as a function of frequency for the TM_1 mode.

this analysis, we will design the light-bending structure to achieve coupling between the TM_1 modes in the slit region and the TM_1 mode in the GaP layer region.

3.4 Wavevector Matching

Wavevector mismatch describes the difference between the wavevector values of an electromagnetic wave in two regions of space. The concept of wavevector mismatch and its effects on electromagnetic wave propagation can be illustrated through a simple one dimensional example. Consider an electromagnetic plane wave normally incident from medium 1, having refractive index n_1, onto medium 2, having refractive index $n_2 \neq n_1$. We assume that both media have positive relative permittivity values. For a homogeneous and isotropic medium, the refractive index of a region, n, is directly related to the wavevector in the region, $\tilde{\beta}$, by

$$\tilde{\beta} = nk_o. \tag{3.2}$$

An electromagnetic wave incident normally at the interface between two media experiences a sudden change in its wavevector. This wavevector mismatch results in reflection of a portion of the incident electromagnetic wave and a reduction in the transmission from medium 1 to medium 2, as shown in Figure 3.8(b). The relative amplitudes of the electromagnetic wave com-

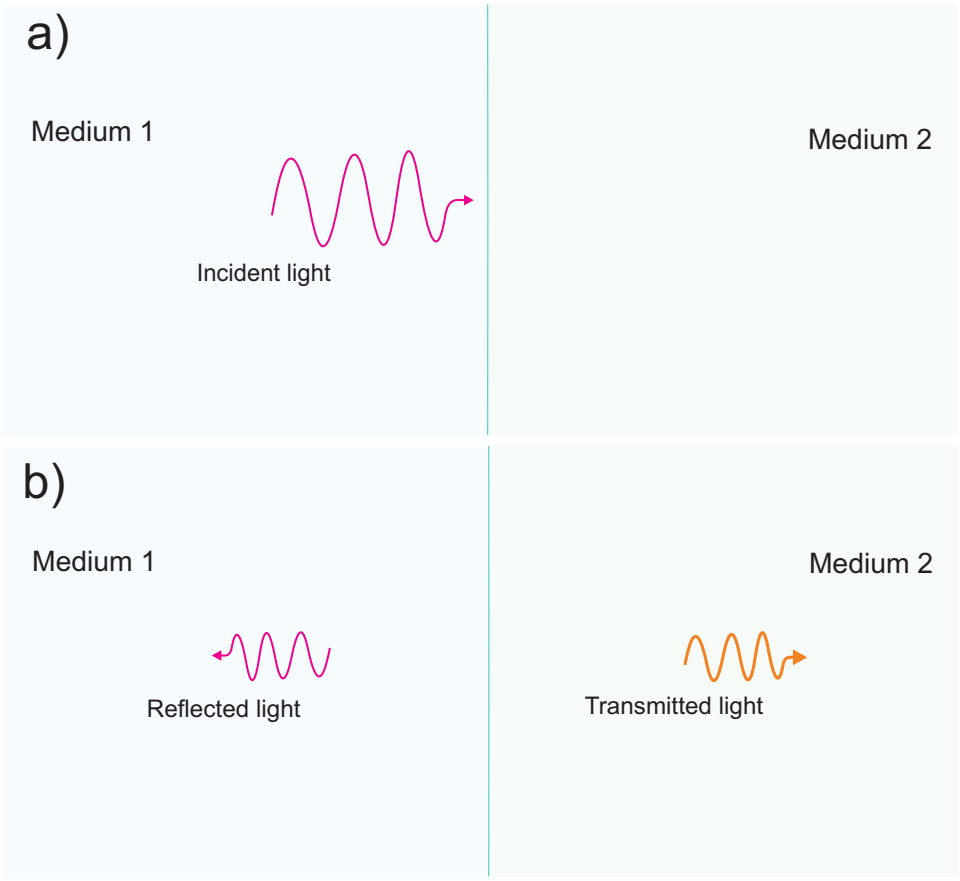

Figure 3.8: A simple example demonstrating the reflection loss due to wavevector mismatch. An electromagnetic plane wave is a) incident onto a dielectric interface and b) scattered into reflected and transmitted components after interacting with the interface. The relative amplitudes of the reflected and transmitted components are proportional to the degree of wavevector mismatch.

ponents in the two media can be predicted by Fresnel equations, given as

$$R = \frac{n_1 - n_2}{n_1 + n_2} \tag{3.3}$$

and

$$\begin{aligned} T &= 1 - R \\ &= \frac{2n_2}{n_1 + n_2}, \end{aligned} \tag{3.4}$$

where R and T are the reflection and transmission coefficients, respectively. The above relations show that as the difference in refractive indices increases (which then yield a wavevector mismatch), a greater portion of the incident electromagnetic wave is reflected and less transmitted.

We extend the concept of wavevector matching to predict the coupling efficiency of the two TM_1 modes sustained by the proposed bi-axial waveguide structure. It is hypothesized that the degree of coupling between the TM_1 mode in the slit section of the structure and the TM_1 mode in the GaP layer section of the structure is maximized when the degree of mismatch between the in-plane wavevector components of the two modes is minimized. This mismatch corresponds to the difference between transverse component of the wavevector, β_{1z}, directed along the z-axis of the TM_1 mode in the slit and the longitudinal component of the wavevector,β_2, directed along the x-axis of the TM_1 mode in the GaP layer. The configuration is shown in Figure 3.9. Thus, efficient coupling is achieved when the condition wavevector matching $\beta_{1z} = \beta_2$ is satisfied.

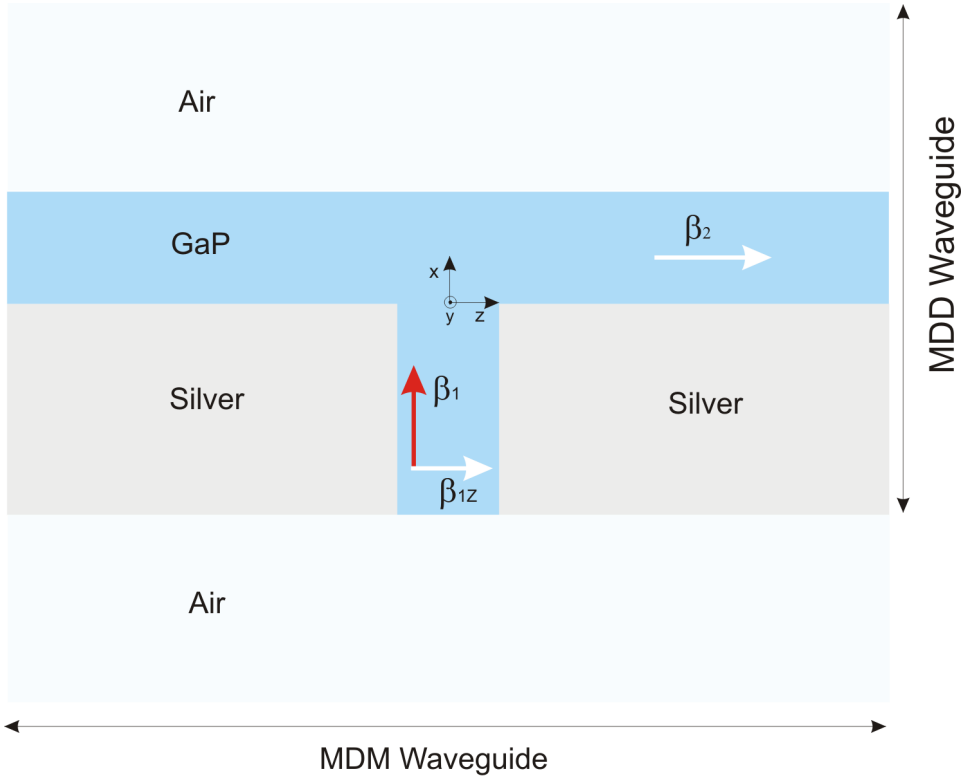

Figure 3.9: Wavevector matching applied to a bi-axial waveguide. Wavevector matching is achieved when the transverse component of the wavevector in the MDM waveguide matches with the longitudinal component of the wavevector in the MDD waveguide.

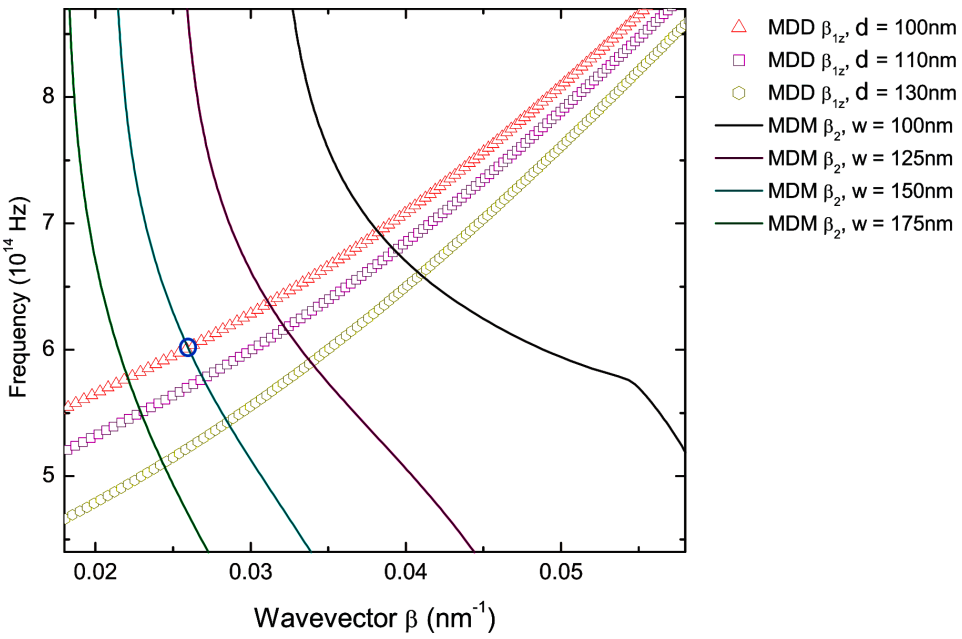

Figure 3.10: Plot of the longitudinal wavevector components of the TM_1 mode sustained by the MDD waveguide (β_2) and the transverse wavevector components of the TM_1 mode sustained by the MDM waveguide (β_{1z}). The blue circle shows the matching point at the operational frequency of $w = 6 \times 10^{14}$ Hz.

3.5 Waveguide Structure Optimization

To determine an optimal configuration that yields wavevector matching, we map out values of β_{1z} of the TM_1 mode in the slit as a function of the slit width and β_2 of the TM_1 mode in the GaP layer as a function of the layer thickness. The wavevector components are plotted in Figure 3.10 over the visible frequency range. For a nominal operational frequency of $\omega = 6 \times 10^{14}$ Hz, wavevector matching is achieved for a slit width value $w = 150$nm and a GaP layer thickness value $d = 100$nm. It is predicted that when a structure with these geometrical parameters is excited by an electromagnetic wave at a frequency of $\omega = 6 \times 10^{14}$ Hz, a TM_1 mode sustained in the slit couples efficiently to a TM_1 mode in the GaP layer.

3.5.1 FDTD Simulation

We test the predictive powers of our analytical method by performing rigorous numerical simulations of the electromagnetic response of the structure using the finite-difference-time-domain (FDTD) technique. The FDTD technique is a widely used method to model the spatial and temporal evolution of electromagnetic waves by directly solving Maxwell's equations over a spatial grid. The temporal and spatial partial derivatives in Maxwell's equations are discretized into difference equations using the central-difference approximations [54]. At a particular time step, the difference equations are solved at each grid point to determine the local amplitude of the electric and magnetic field components.

To model the electromagnetic response of the proposed coupling struc-

ture, we use a two dimensional spatial grid in the $x - z$ plane consisting of 4000×1400 pixels with a resolution of 1 nm/pixel, resulting in a rectangular grid occupying a physical area of 4.0×1.4 μm. A perfectly matched layer is placed at the edges of the simulation space [55–57]. This layer is impedance matched to free-space so that any electromagnetic waves incident onto the layer are totally absorbed and do not reflect back into the simulation space. Within the simulation space, we defined both an electromagnetic wave source and our proposed structure. The source consists of a TM-polarized electromagnetic wave oscillating at a frequency of $\omega = 6 \times 10^{14}$ Hz, which corresponds to a free-space wavelength $\lambda = 500$nm. The TM-polarized electromagnetic wave has a magnetic field component H_y and two electric field components E_x and E_z. The wave propagates in $+x$-direction and is centered at $z = 0$ with a full-width-at-half maximum of 1200 nm. Our structure is defined in the simulation space by assigning to the grid points occupied by the structure the relative permittivity of the local medium. For grid points corresponding to GaP, we assign a relative permittivity of 3.5^2. For grid points corresponding to silver, we model the relative permittivity using the Drude model with experimentally obtained Drude parameters. For grid points corresponding to air, we assign a unity relative permittivity.

Based on the field distributions calculated by the FDTD simulations, we measure the bending efficiency of the structure. Line detectors D_1, D_2, and D_3 are placed at different locations in the simulation space to measure the time-averaged values of the magnetic field intensity $|H_y|^2$. Detectors D_1 and D_2 are placed in the GaP layer to the left and right of the slit exit and the detector D_3 is placed in the air region above the slit exit. The

bending efficiency is quantified by the ratio of $|H_y|^2$ captured by D_1, D_2 to the total $|H_y|^2$ emitted from the slit and captured by D_1, D_2, and D_3. The bending efficiency therefore measures the percentage of the electromagnetic wave exiting the slit region of the structure that couples into the GaP layer.

Figure 3.12 shows a snapshot of the FDTD-calculated magnetic field intensity distribution when the structure is illuminated at a wavelength of $\lambda = 500$ nm. Light incident from the bottom of the structure channels into the slit and then emerges from the exit of the slit. There are two pathways for the light emerging from the slit: it can bend into the GaP layer or radiate into the air region above the GaP layer. At a wavelength of $\lambda = 500$ nm, highly efficient light bending at the slit exit is evident from almost complete diversion of the $+x$-propagating TM_1 mode in the slit into the $\pm z$-propagating TM_1 modes in the GaP layer, with minimal light scattered into free-space plane wave modes in the air region above the GaP layer. Figures 3.12(b) and (c) show the FDTD-calculated magnetic field intensity distribution when the structure is illuminated at wavelengths of $\lambda = 450$ nm and $\lambda = 400$ nm, respectively. For these shorter wavelengths, there is a greater amount of light scattered into the air region above the bend and relatively less light coupled into the GaP layer. Comparison of the FDTD calculated field distributions suggests that the efficiency of light bending at the slit exit is highly sensitive to the incident electromagnetic wavelength (and hence frequency).

Figure 3.13 plots the FDTD-calculated bending efficiency as a function of the GaP layer thickness d for a fixed wavelength $\lambda = 500$ nm. The FDTD simulations show that the bending efficiency reaches a maximum of 92% at

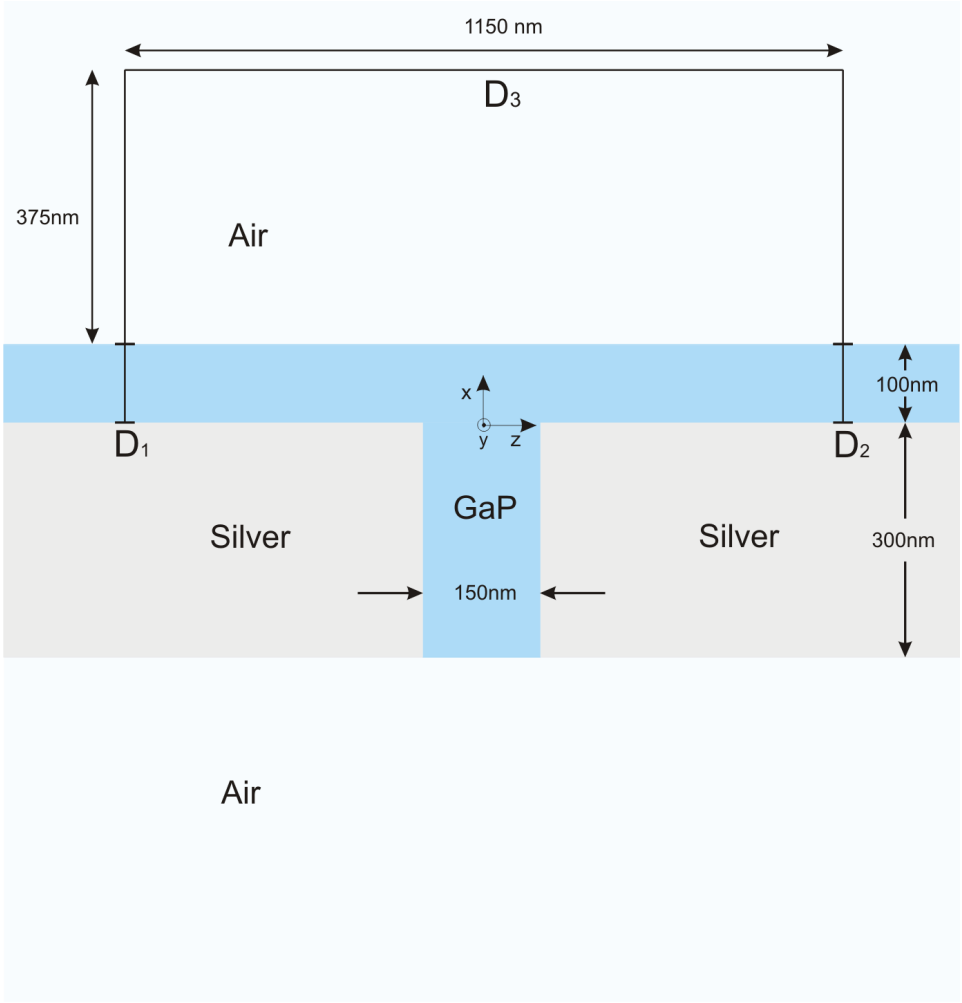

Figure 3.11: Simulation geometry of the waveguide structure designed to bend incident light at a frequency $\omega = 6 \times 10^{14}$ Hz. The structure has a metal thickness $t = 300$nm, slit width $w = 150$nm and dielectric cap $d = 100$nm. The detectors D_1 and D_2 measure the time-averaged magnetic field intensity,$|H_y|^2$, of the TM_1 mode in the GaP layer, and the detector D_3 measures $|H_y|^2$ radiated into the air region.

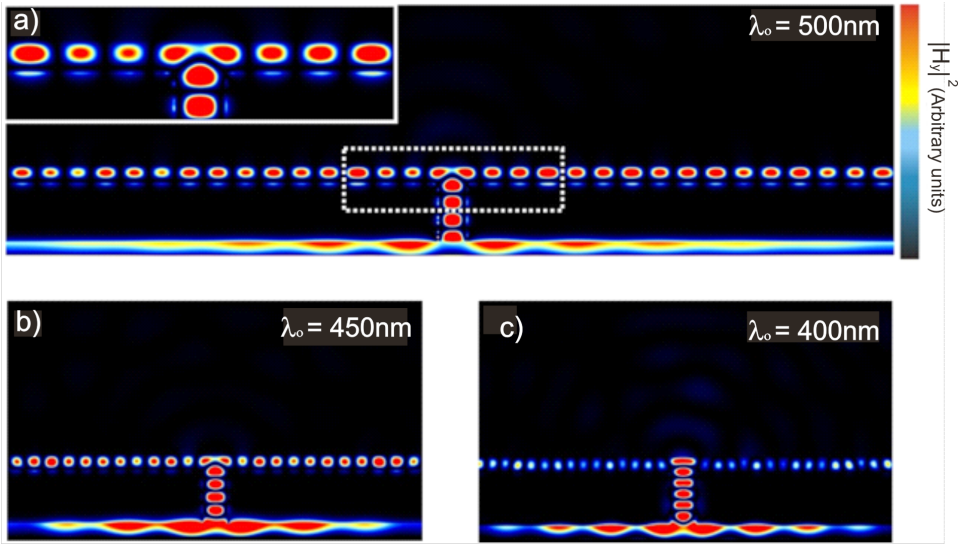

Figure 3.12: FDTD calculations to determine the bending efficiency for the designed waveguide. For calculations, TM-polarized wave centered at z = 0 with a full-width-at-half-maximum of 1200nm is normally incident on the bottom surface of the slit. Snapshots of the instantaneous magnetic field intensity for normally-incident, free-space, TM-polarized illumination of the structure at (a) $\omega = 6 \times 10^{14}$ Hz, $\lambda = 500$ nm (b) $\omega = 6.67 \times 10^{14}$ Hz, $\lambda = 450$ nm, and (c) $\omega = 7.5 \times 10^{14}$ Hz, $\lambda = 400$nm for fixed parameters $w = 150$nm and $d = 100$nm. The inset in (a) highlights the TM mode emanating from the slit to split symmetrically into TM_1 modes confined inside the GaP layer.

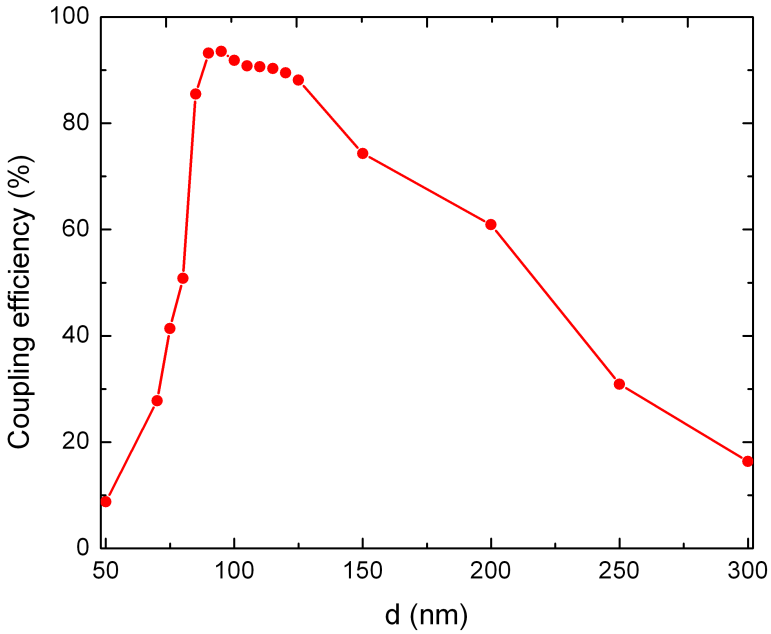

Figure 3.13: Coupling efficiency as a function of GaP layer thickness d. The frequency of the incident light is kept constant at $\omega = 6 \times 10^{14}$ Hz.

an optimal layer thickness $d = 100$ nm. This optimal value matches the layer thickness value predicted to yield wavevector matching. The bending efficiency drops off for layer thickness values both smaller and larger than the optimal value.

Figure 3.14 depicts the FDTD-calculated bending efficiency as a function of the wavelength of incident light for fixed slit width, $w = 150$ nm and GaP layer thickness, $d = 100$ nm. The FDTD calculations show that the bending efficiency is greater than 90% for incident wavelengths $\lambda = 450$ nm and $\lambda = 500$ nm. Increasing or decreasing the wavelength outside of these

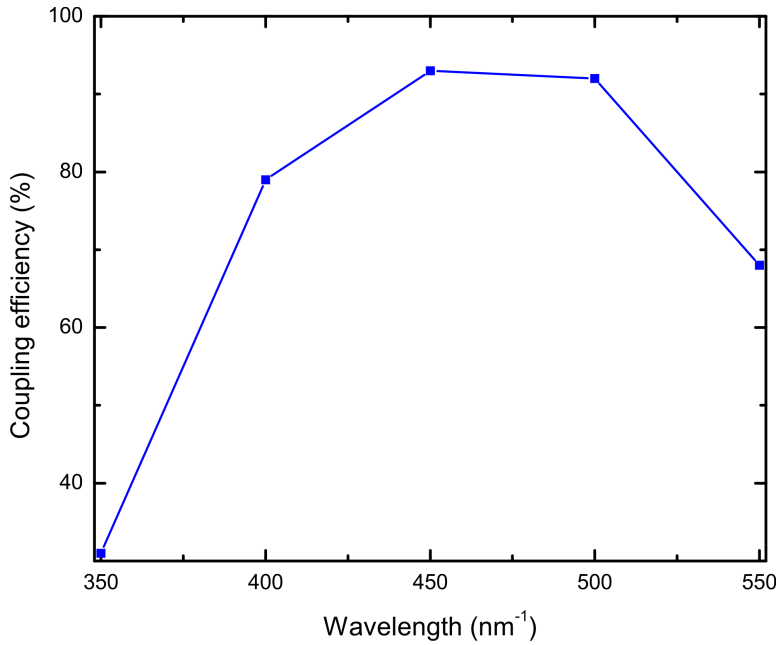

Figure 3.14: Coupling efficiency as a function of λ. The slit width and layer thickness are kept constant at $w = 150$ nm and $d = 100$ nm, respectively.

values, yields a dramatic drop in the bending efficiency of the structure. The FDTD calculations therefore support our hypothesis that in-plane wavevector matching, which is achieved for a single combination of slit width, layer thickness and wavelength, yields highly efficient mode coupling. For parameters departing from these optimal parameters, the coupling efficiency drops dramatically.

3.6 Summary

In this chapter we have presented a technique for designing a bi-axial nanoscale metal waveguide that can bend light around a tight $\pm 90^{\circ}$ bend. The design technique consists of first breaking the bi-axial waveguide into two region, each of which is then approximated as an independent uni-axial waveguide. The modes sustained by each of the uni-axial waveguides are mapped out to determine the propagative modes. The geometrical parameters for each of the uni-axial waveguides are designed such that the in-plane wavevector components of the propagative modes in the waveguides are matched. The wavevector matching condition is predicted to yield maximum coupling between the electromagnetic modes, even when they propagate along perpendicular directions, and thus achieve highly efficient light bending. The performance of the designed structure is modeled using a finite-difference-time-domain (FDTD) technique which solves Maxwell's equations directly over a discretized spatial grid. The FDTD-calculated bending efficiency as a function of the GaP layer thickness shows a pronounced peak for parameters corresponding to the wavevector matching condition, supporting the hypothesis that wavevector matching yields highly efficient coupling. Our design methodology is useful because it can potentially circumvent the need for tedious numerical simulations and may find application in the design of highly-integrated, miniaturized optical circuits.

Chapter 4

Multi-Axial Surface-Plasmon-Polariton Coupling

Surface plasmon polariton (SPP) modes are electromagnetic excitations at an interface between a metal and dielectric, hold promise for the miniaturization of optical devices [58, 59]. Due to the lack of readily-available sources directly emitting SPP modes, designing methods to couple plane-wave modes to SPP modes with high efficiency and throughput remains an important objective. Plane-wave modes directly incident onto a metal-dielectric interface cannot efficiently couple into SPP modes due to a mismatch between the SPP wavevector and the component of the plane-wave wavevector along the interface. Scatterers have been used to bridge the wavevector mismatch between plane-wave and SPP modes. When a scatterer is illuminated, enhancement of the incident plane-wave wavevector along the metal-dielectric interface by the Fourier spatial frequency components of the scatterer geometry in the plane of the interface enables wavevector matching between the incident light and the SPP mode.

A widely-used scatterer-based SPP coupling technique is to illuminate a slit in a metal film. Slit based SPP couplers have an inherent advantage that they can be easily incorporated in integrated optical devices. When a slit is illuminated with a TM-polarized plane wave, a small portion of the incident wave excites a guided mode in the slit. The guided mode propagates through the slit and subsequently diffracts at the slit exit. The total light intensity leaving the slit exit defines the total throughput, the SPP intensity leaving the slit exit defines the SPP throughput, and the ratio of the SPP throughput to the total throughput defines the SPP coupling efficiency. The throughput and efficiency of a slit are highly dependent on the width of the slit relative to the wavelength of the incident plane wave. A slit of width less than the wavelength has inherently low total throughput and low SPP throughput, but is capable of high SPP coupling efficiency. It has already been demonstrated that the SPP coupling efficiency of a sub-wavelength slit is increased up to $\simeq 80\%$ by coating the slit with a nanoscale dielectric layer[60]; the dielectric layer, however, does not significantly affect the SPP throughput. The objective of this chapter is to design a SPP coupling scheme capable of both high throughput and high efficiency.

Increasing the total throughput of a slit can be achieved by simply increasing the slit width. Increasing the SPP throughput, on the other hand, is more challenging because the SPP throughput is dependent on the coupling between the guided mode in the slit and the SPP mode, which has not been fully explored yet. Recently, several theoretical [61–63] and semi-analytical [60, 64–66] models have been developed to describe coupling from a guided mode in a single slit to a SPP mode. The SPP mode is defined

by a single, unique solution to Maxwell's equations when the magnetic field boundary conditions are imposed at the metal surface. The guided mode in the slit, on the other hand, generally consists of a superposition of infinite TM-polarized waveguide eigenmodes, and each of these modes correspond to a unique solution to the Maxwell's equations when the magnetic field boundary condition are imposed at the slit edges. The width of the slit dictates the eigenmode composition of the guided mode in the slit. All previous models [60–66] describing SPP coupling by a slit have assumed a slit width less than the wavelength. When the slit width is less than the wavelength, all eigenmodes are attenuated except the zeroth-order TM mode, TM_0 (also known as SPP mode) and the guided mode is accurately and simply approximated as the TM_0 mode. The TM_0 mode approximation becomes increasingly inaccurate [62, 64] as the slit width is increased to values comparable to and/or larger than the wavelength and higher-order eigenmodes become predominant. To date, accurate models of SPP coupling from super-wavelength slits sustaining higher-order eigenmodes have yet to be realized.

In this work, we propose and characterize a new SPP coupling technique for multi-axial metal waveguide structures. The technique is applied on a bi-axial metal waveguide constructed using slit of super-wavelength width immersed in a uniform dielectric. The width of the super-wavelength slit is selected to sustain a first-order TM_1 eigenmode, TM_1 mode, just above cut-off, which then couples to the SPP mode at the slit exit. This is in contrast to previously explored SPP coupling configurations using sub-wavelength slits that sustain only the lowest-order TM_0 eigenmode [60–66]. We show

that the TM_1 mode just above cutoff is advantageous for SPP coupling because it possesses a transverse wavevector component (lying in the plane of the metal surface) that is larger than that achievable with a TM_0 mode in a slit of sub-wavelength width. It is proposed that if the transverse wavevector component of the TM_1 mode, added with the peak Fourier spatial frequency component (due to diffraction at the slit exit), equals to the wavevector of the SPP mode on the metal surface, high SPP coupling efficiency is achievable. The hypothesis is tested by numerical simulation of visible light propagation through a slit as a function of the slit width and refractive index. An optimized geometry is discovered that satisfies the predicted wavevector matching condition, yielding a peak SPP coupling efficiency of $\simeq 68\%$ and an SPP throughput that is over an order of magnitude greater that achieved with a sub-wavelength slit. Compared to a sub-wavelength slit, the optimized super-wavelength slit geometry is easier to fabricate, has comparable SPP coupling efficiency and an over order-of-magnitude greater SPP throughput.

4.1 Hypothesis

Consider a semi-infinite layer of metal (silver) with relative complex permittivity $\tilde{\epsilon}_m$ extends infinitely in the y- and z-directions and having thickness t. A slit of width w oriented parallel to the x-axis and centred at $z = 0$ is cut into the metal film. The metal film is immersed in a homogeneous dielectric medium with relative permittivity ϵ_d and refractive index $n = \sqrt{\epsilon_d}$. The complete structure is presented in Fig. 4.1. The slit is illuminated from the region below it with a TM-polarized electromagnetic plane wave of wave-

length $\lambda = \lambda_0/n$ and wavevector $\beta_i = \beta_i \hat{x}$, where $\beta_i = 2\pi/\lambda$. The $+x$-axis defines the longitudinal direction, and the z-axis defines the transverse axis. The electromagnetic wave couples into a guided mode in the slit having complex wavevector $\tilde{\beta} = \tilde{\beta}_x \hat{x} + \tilde{\beta}_z \hat{z}$, where $\tilde{\beta}_x$ and $\tilde{\beta}_z$ are the longitudinal and transverse components of the complex wavevector, respectively. The attenuation of the guided mode in the slit can be characterized by a figure of merit (FOM) as described in previous chapter using eq. 3.1. When the guided mode exits the slit, electromagnetic energy is coupled into plane-wave modes and $\pm z$-propagating SPP modes. The SPP modes have complex wavevector $\pm\tilde{\beta}_{spp}\hat{z}$, where $\mathrm{Re}[\tilde{\beta}_{spp}]$ and $\mathrm{Im}[\tilde{\beta}_{spp}]$ describe the spatial periodicity and attenuation, respectively, of the SPP field along the transverse direction.

We treat the bi-axial waveguide SPP coupler by first dividing the structure into two uni-axial waveguides and mapping out the modes in each of the waveguides. The slit region is approximated as a metal-dielectric-metal (MDM) waveguide and the top of the metal film is approximated as a metal-dielectric (MD) waveguide. The waveguide parameters are tuned such that a propagating TM_1 mode in the MDM waveguide couples to a SPP mode in the MD waveguide. We map out the wavevector values of the TM_0 and TM_1 modes sustained in the slit (approximated as a MDM waveguide) for varying slit width by solving the complex eigenvalue equation, Eq. 2.26 using the Davidenko method. $\tilde{\epsilon}_m$ is modeled by fitting to experimental data of the real and imaginary parts of the permittivity of silver as obtained in Section 1.8, and ϵ_d is assumed to be real and dispersion-less. Figure 4.2(a) shows FOM curves for TM_0 and TM_1 modes in slits of varying width for the

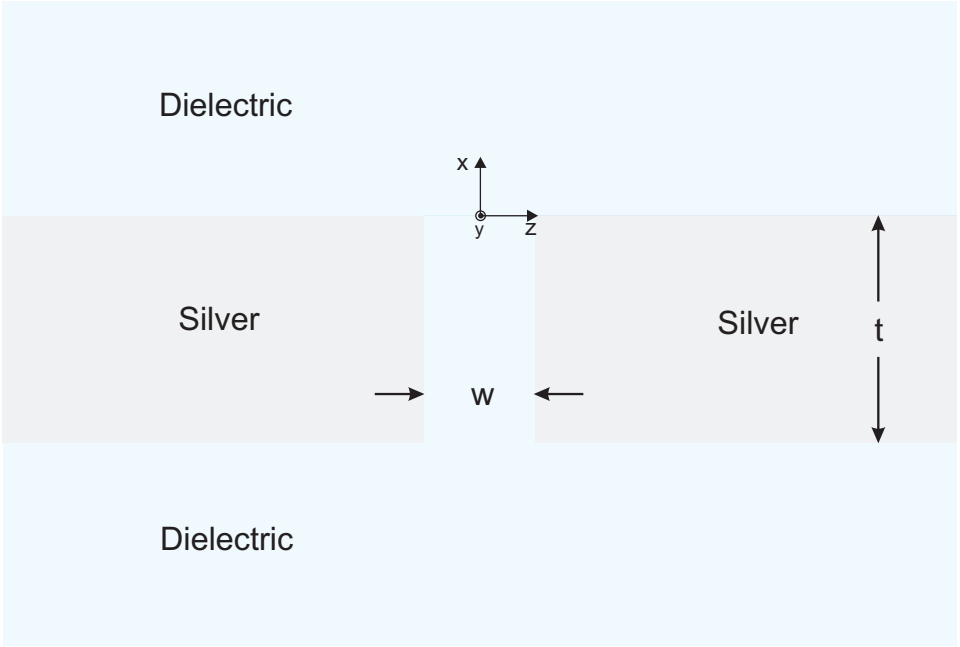

Figure 4.1: Waveguide structure consisting of a slit in a metal film immersed in a dielectric. TM-polarized light is normally incident from the bottom of the structure and is confined within the dielectric core.

representative case where the slit is immersed in a dielectric with a refractive index $n = 1.75$. The FOM values for the TM_0 modes are largely insensitive to variations in the slit width and gradually decrease as a function of increasing frequency. FOM curves for the TM_1 modes are characterized by a lower-frequency region of low figure of merit and a higher-frequency region of high figure of merit, separated by a kneel located at a cutoff frequency. The cutoff slit width w_c for the TM_1 mode at a given frequency ω is the threshold slit width value below which the TM_1 mode is attenuating. At a fixed visible frequency $\omega = 6.0 \times 10^{14}\,\mathrm{Hz}$ ($\lambda = 285\,\mathrm{nm}$), $w_c \sim 300\,\mathrm{nm}$. The dominant mode in the slit can be identified at a particular frequency and slit width by the mode with the largest FOM. The TM_0 mode is dominant for $w < w_c$, and the TM_1 mode is dominant for $w > w_c$.

The real part of the transverse wavevector component, $\mathrm{Re}[\tilde{\beta}_z]$, of the guided mode in the slit describes the component of electromagnetic momentum in the transverse plane parallel to the plane of the metal surface. Values of $\tilde{\beta}_z$ are obtained from the relation

$$\tilde{\beta}_z = \sqrt{{\beta_i}^2 - \tilde{\beta}_x^2}, \tag{4.1}$$

where $\beta_i = n\beta_0$ is the magnitude of the wavevector in the dielectric core of the slit. Figure 4.2(b) shows $\mathrm{Re}[\tilde{\beta}_z]$ values over the visible-frequency range for the TM_0 mode in a slit of width $w = 200\,\mathrm{nm}$ and for the TM_1 mode in slits of widths $w = 350\,\mathrm{nm}$ and $w = 500\,\mathrm{nm}$. At the frequency $\omega = 6.0 \times 10^{14}\,\mathrm{Hz}$, $\mathrm{Re}[\tilde{\beta}_z]$ for the TM_0 mode in the $w = 200\,\mathrm{nm}$ slit is nearly two orders of magnitude smaller than $\mathrm{Re}[\tilde{\beta}_z]$ for the TM_1 mode in

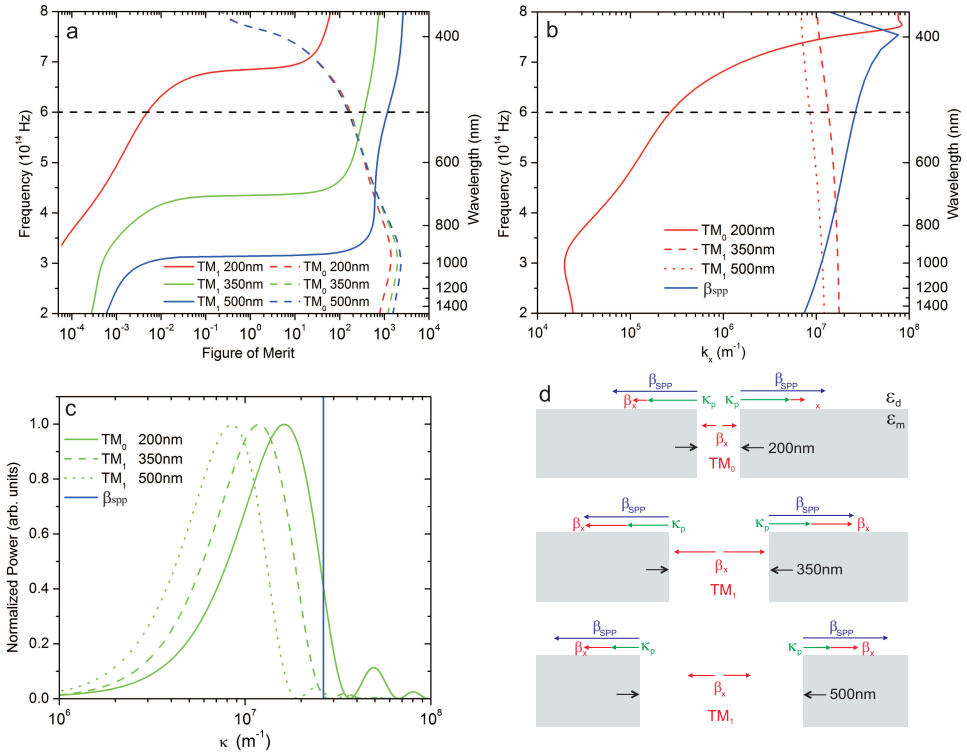

Figure 4.2: Formulation of a hypothesis for diffraction-assisted SPP coupling by a super-wavelength slit aperture. a) Figure-of-merit and b) the real transverse wavevector component versus frequency and wavelength for TM_0 and TM_1 modes sustained in slits of different widths. c) Diffraction spectrum corresponding to the TM_0 mode in a 200- nm-wide slit and the TM_1 modes in 350- nm-wide and 500- nm-wide slits. d) Wavevector-space depiction of diffraction-assisted SPP coupling from slits of width $w = 200\,\text{nm}$, $w = 350\,\text{nm}$, and $w = 500\,\text{nm}$, immersed in a uniform dielectric of refractive index $n = 1.75$.

the $w = 350\,\text{nm}$ and $w = 500\,\text{nm}$ slits. Values of $\text{Re}[\tilde{\beta}_z]$ for the TM_1 mode generally increase for decreasing slit width. Given the parameters in Fig. 4.2(b) and for a fixed $\omega = 6.0 \times 10^{14}\,\text{Hz}$, $\text{Re}[\tilde{\beta}_z]$ for the TM_1 mode increases from $8.5 \times 10^6\,\text{m}^{-1}$ to $1.3 \times 10^7\,\text{m}^{-1}$ as the slit width decreases from 500 nm to 350 nm.

Diffraction at the slit exit generates transverse spatial frequency components, κ. The diffraction spectrum is a distribution of transverse spatial frequencies generated by diffraction at the slit exit. We calculate the diffraction spectrum by Fourier transformation of the transverse field profiles of the guided mode [67]. Figure 4.2(c) shows the normalized diffraction spectrum for slit widths $w = 200\,\text{nm}$, $w = 350\,\text{nm}$, and $w = 500\,\text{nm}$ at a fixed frequency $\omega = 6.0 \times 10^{14}\,\text{Hz}$. The peak transverse spatial frequency component, κ_p, is the spatial frequency at which the diffraction spectrum peaks. For the parameters in Fig. 4.2(c), κ_p shifts from $1.6 \times 10^7\,\text{m}^{-1}$ to $\kappa_p = 8.3 \times 10^6\,\text{m}^{-1}$ as the slit width increases from $w = 200\,\text{nm}$ to $w = 500\,\text{nm}$. It is noteworthy that $\kappa_p < \text{Re}[\tilde{\beta}_{spp}]$ for all slit width values.

A simple picture of diffraction-assisted SPP coupling based on the data in Figs. 4.2(a)-(c) for $w = 200\,\text{nm}$, $w = 350\,\text{nm}$ and $w = 500\,\text{nm}$ at a fixed $\omega = 6.0 \times 10^{14}\,\text{Hz}$ is presented in Fig. 4.2(d). SPP coupling at the slit exit is mediated by diffraction of the guided mode, yielding a net real transverse wavevector component $\text{Re}[\tilde{\beta}_z] + \kappa_p$. Coupling from the diffracted mode at the slit exit to the SPP mode adjacent to the slit exit is optimized when the wavevector-matched condition $\text{Re}[\tilde{\beta}_z] + \kappa_p = \text{Re}[\tilde{\beta}_{spp}]$ is satisfied. Because $\text{Re}[\tilde{\beta}_{spp}]$ is generally larger than both $\text{Re}[\tilde{\beta}_z]$ and κ_p, large and commensurate contributions from both $\text{Re}[\tilde{\beta}_z]$ and κ_p are required to

fulfill wavevector matching. In a sub-wavelength slit, the TM_0 mode has $\mathrm{Re}[\tilde{\beta}_z] << \kappa_p$ and SPP coupling at the slit exit requires a sufficiently small slit width to generate large diffracted spatial frequency components to match with $\mathrm{Re}[\tilde{\beta}_{spp}]$. On the other hand, a super-wavelength slit sustains a TM_1 mode with $\mathrm{Re}[\tilde{\beta}_z] \simeq \kappa_p$. The large contributions of $\mathrm{Re}[\tilde{\beta}_z]$ to the net real transverse wavevector component reduces the required contributions from κ_p needed for wavevector matching. As a result, wavevector matching with the SPP mode adjacent to the slit exit can be achieved with a relatively large slit aperture.

4.2 Methodology

SPP coupling efficiency of a slit immersed in a dielectric is modeled using finite-difference-time-domain (FDTD) simulations of Maxwell's equations. The simulation grid has dimensions of 4000×1400 pixels with a resolution of 1 nm/pixel and is surrounded by a perfectly-matched layer to eliminate reflections from the edges of the simulation space. The incident beam is centered in the simulation space at $z = 0$ and propagates in the $+x$-direction, with a full-width-at-half-maximum of 1200 nm and a waist located at $x = 0$. The incident electromagnetic wave has a free-space wavelength $\lambda_0 = 500\,\mathrm{nm}$ and is TM-polarized such that the magnetic field, H_y, is aligned along the y-direction.

Control variables of this study include the type of metal (chosen as silver), the thickness of the metal layer (set at $t = 300\,\mathrm{nm}$), the polarization of the incident electromagnetic wave (TM), the angle of incidence of the

incident electromagnetic wave (normal), and the wavelength of the incident electromagnetic wave ($\lambda_0 = 500\,\text{nm}$). The independent variables include the width of the slit, w, which is varied from 100 nm to 800 nm, and the refractive index of the surrounding dielectric n, which varies from 1.0 to 2.5. The dependent variables are the time-averaged intensity of the SPP modes coupled to the metal surface at the slit exit, I_{spp}, the time-averaged intensity of the radiated modes leaving the slit region, I_r, and the SPP coupling efficiency, η. The dependent variables are quantified by placing line detectors in the simulation space to capture different components of the intensity pattern radiated from the exit of the slit, similar to the method employed in chapter 3. The I_{spp} detectors straddle the metal/dielectric interface, extending 50 nm into the metal and $\lambda_0/4\,\text{nm}$ into the dielectric region above the metal, and are situated adjacent to the slit exit a length λ_0 away from the edges of the slit. The I_r detector captures the intensity radiated away from the slit that is not coupled to the surface of the metal. The coupling efficiency is then calculated by the equation

$$\eta = \frac{1}{1 + I_r/I_{spp}}. \tag{4.2}$$

4.3 Results and Discussion

The numerical simulations provide evidence of high-throughput and high-efficiency SPP coupling from a slit of super-wavelength width. Figure 4.3 displays representative snap-shots of the instantaneous $|H_y|^2$ intensity and time-averaged $|H_y|^2$ angular distribution calculated from FDTD simula-

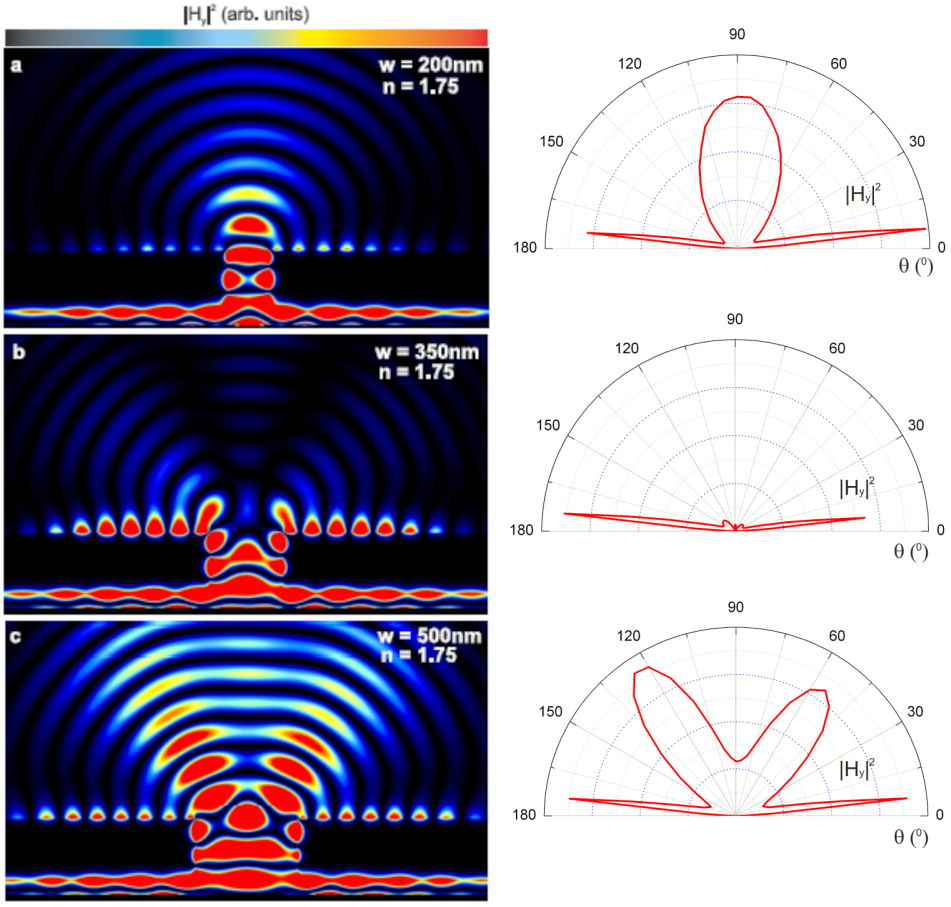

Figure 4.3: Images of the FDTD-calculated instantaneous $|H_y|^2$ distribution (left) and the time-averaged $|H_y|^2$ angular distribution (right) for a slit of width values a) $w = 200\,\text{nm}$, b) $w = 350\,\text{nm}$, and c) $w = 500\,\text{nm}$ immersed in a dielectric ($n = 1.75$) and illuminated by a quasi-plane-wave of wavelength $\lambda_0 = 500\,\text{nm}$. A common saturated color scale has been used to accentuate the fields on the exit side of the slit.

tions for plane-wave, TM-polarized, normal-incidence illumination of a slit immersed in a dielectric ($n = 1.75$) for slit width values $w = 200\,\text{nm}$, $w = 350\,\text{nm}$, and $w = 500\,\text{nm}$. Radiative components of the field in the dielectric region above the slit propagate away from the metal-dielectric interface, and plasmonic components propagate along the metal-dielectric interface. For $w = 200\,\text{nm}$ [Fig. 4.3(a)], the incident plane wave couples into a propagative TM_0 mode in the slit, which is characterized by intensity maxima at the dielectric-metal sidewalls. Diffraction of the TM_0 mode at the exit of the slit yields a relatively strong radiative component with an angular intensity distribution composed of a primary lobe centred about the longitudinal axis and a relatively weak plasmonic component. A lobe describes the concentration of electromagnetic energy in a region. For $w = 350\,\text{nm}$ [Fig. 4.3(b)] and $w = 500\,\text{nm}$[Fig. 4.3(c)], the incident plane wave couples primarily into the TM_1 mode in the slit, which is characterized by an intensity maximum in the dielectric core of the slit. The high-throughput SPP coupling is evident by the large SPP intensities observed for $w = 350\,\text{nm}$. Diffraction of the TM_1 mode at the $w = 350\,\text{nm}$ slit exit yields a relatively weak radiative component with an angular intensity distribution skewed at highly oblique angles and a relatively strong plasmonic component. Further increasing the slit width to $w = 500\,\text{nm}$ increases the total throughput of the slit, but reduces the efficiency of SPP coupling. Diffraction of the TM_1 mode at the $w = 500\,\text{nm}$ slit exit yields a strong radiative component with an angular intensity distribution composed of two distinct side lobes and a relatively weak plasmonic component.

Trends in the SPP coupling efficiencies calculated from the FDTD simu-

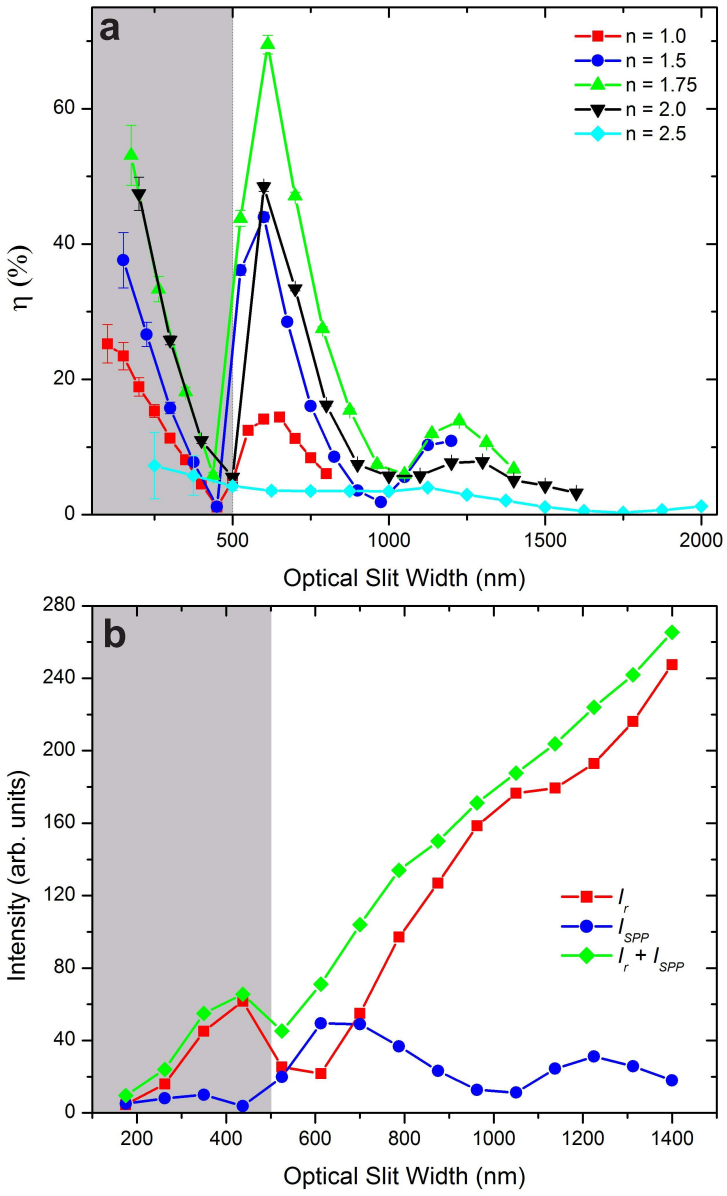

Figure 4.4: a) SPP coupling efficiency as a function of optical slit width for dielectric refractive index values $n = 1.0$ (squares), $n = 1.5$ (circles), $n = 1.75$ (upright triangles), $n = 2.0$ (inverted triangles), $n = 2.5$ (diamonds). b) The measured SPP intensity (squares), radiative intensity (circles), and total intensity (diamonds). The shaded region indicates the sub-wavelength-slit-width regime.

lations are compared to qualitative predictions from the model of diffraction-assisted SPP coupling described in Fig. 4.4. Figure 4.4(a) plots the FDTD-calculated SPP coupling efficiencies as a function of the optical slit width nw for dielectric refractive index values ranging from $n = 1.0$ to $n = 2.5$. For sub-wavelength slit width values $nw < \lambda_0$, highest SPP coupling efficiency is observed for the smallest optical slit width. This trend is consistent with diffraction-dominated SPP coupling predicted to occur for sub-wavelength slit widths, in which small slit width is required to yield large diffracted spatial frequencies to achieve wavevector matching. For super-wavelength slit width values $nw > \lambda_0$, the SPP coupling efficiencies exhibit periodic modulations as a function of optical slit width, qualitatively agreeing with the general trends observed in experimental data measured for a slit in air [64] and theoretical predictions based on an approximate model for SPP coupling from a slit [62]. The data in Fig. 4.4 reveals that the magnitude of the fluctuations in the SPP coupling efficiencies are highly sensitive to the dielectric refractive index. For refractive index values $n = 1.0$, 1.5, 1.75, and 2.0, the SPP coupling efficiency rises as nw increases above λ_0 and reaches local maxima of $\eta = 14\%$, 44%, 68%, and 48% at a super-wavelength optical slit width $nw \simeq 600\,\text{nm}$, respectively. The rapid increase in η as the slit width increases from sub-wavelength slit width values to super-wavelength slit width values is attributed to the disappearance of the TM_0 mode in the slit and the emergence of the TM_1 mode in the slit, which boosts the net real transverse wavevector component at the slit exit to enable wavevector matching. It is interesting to note that the SPP coupling efficiency peak at $nw = 600\,\text{nm}$ observed for lower refractive index values is absent for $n = 2.5$.

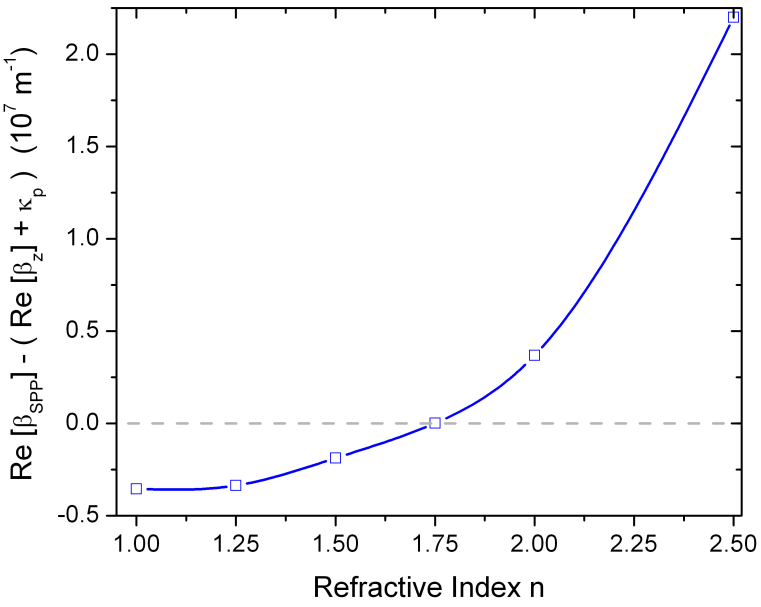

Figure 4.5: Wavevector mismatch $\mathrm{Re}[\tilde{\beta}_{spp}] - (\mathrm{Re}[\tilde{\beta}_z] + \kappa_p)$ as a function of refractive index of the dielectric region for a fixed optical slit width $nw = 600\,\mathrm{nm}$ and free-space wavelength $\lambda_0 = 500\,\mathrm{nm}$.

Figure 4.4(b) displays the time-averaged radiative intensity I_r, SPP intensity I_{spp}, and total intensity $I_t = I_{spp} + I_r$, as a function of the optical slit width for $n = 1.75$. Although the smallest optical slit width generally yields high SPP coupling efficiency, the total throughput and the SPP throughput is low. As the optical slit width increases to $w \simeq \lambda_0$ from sub-wavelength values, an increase in I_r and a decrease in I_{spp} yield low SPP coupling efficiency. In the super-wavelength range of optical slit width values, $520\,\text{nm} < nw < 700\,\text{nm}$, concurrently high SPP throughput and high SPP coupling efficiency ($\eta > 50\%$) are observed. For the optical slit width value $nw \simeq 600\,\text{nm}$, I_{spp} is about an order of magnitude larger than I_{spp} for the smallest slit width value $nw = 175\,\text{nm}$. As the optical slit width is further increased $nw > 700\,\text{nm}$, I_r is significantly greater than I_{spp}, resulting again in low SPP coupling efficiencies.

Variations in the peak SPP coupling efficiency at a fixed optical slit width $nw = 600\,\text{nm}$ for varying n can be qualitatively explained by the mismatch between the net real transverse wavevector component $\text{Re}[\tilde{\beta}_z] + \kappa_p$ and the real SPP wavevector $\text{Re}[\tilde{\beta}_{spp}]$. Figure 4.5 plots the transverse wavevector mismatch $\text{Re}[\tilde{\beta}_{spp}] - (\text{Re}[\tilde{\beta}_z] + \kappa_p)$ as a function of the dielectric refractive index at a constant optical slit width value $nw = 600\,\text{nm}$. The wavevector mismatch increases monotonically from $-0.4 \times 10^7\,\text{m}^{-1}$ to $2.4 \times 10^7\,\text{m}^{-1}$ as the refractive index increases from $n = 1.0$ to $n = 2.5$, crossing zero at $n = 1.75$. Coincidence between the n value that yields peak SPP coupling efficiency at $nw = 600\,\text{nm}$ and that which yields zero wavevector mismatch supports the hypothesis that optimal SPP coupling efficiency occurs when $\text{Re}[\tilde{\beta}_{spp}] = (\text{Re}[\tilde{\beta}_z] + \kappa_p)$, and that this condition can be achieved using a

super-wavelength slit aperture immersed in a dielectric. The relatively large wavevector mismatch for $n = 2.5$ is also consistent with the noted absence of a SPP coupling efficiency peak at $nw = 600\,\text{nm}$.

4.4 Summary

In this chapter, we have designed a bi-axial waveguide SPP coupler that converts a TM_1 mode in a slit to a SPP mode on an adjacent metal surface with high-throughput and high-efficiency. The crux of the design is a super-wavelength slit aperture immersed in a uniform dielectric sustaining a TM_1 mode just above cutoff. High SPP coupling efficiency is achieved when the transverse wavevector component of the TM_1 mode, added with the peak diffracted spatial frequency component, equals to the wavevector of the SPP mode on the metal surface. Based on numerical simulations using FDTD of light propagation through a slit of varying slit width and varying surrounding dielectric refractive index, an optimal slit width and refractive index combination is found that provides high efficiency coupling. The parameters also match the parameters predicted to yield wavevector matching.

Chapter 5

Conclusion

Optical waveguides are structures that guide light. The advent of nanofabrication techniques now allows controlled manufacturing of optical waveguides with nanometer scale features using dielectric, metallic, or semi-conducting materials. Given the degrees of freedom afforded by nanofabrication, optimization of a waveguide design requires efficient modeling techniques. All modeling schemes are based on Maxwell's equations. The way in which Maxwell's equations are applied to model a given optical waveguide depends on the complexity of the waveguide geometry. One of the simplest configurations is the uni-axial waveguide, which guides electromagnetic waves along a single axial direction. The electromagnetic properties of a uni-axial waveguide are easily determined and can be modeled by analytically solving Maxwell's equations. Multi-axial waveguides, on the other hand, guide electromagnetic waves along more than one direction. They are challenging to model by analytical solutions to Maxwell's equations and often require numerical techniques. One of the most popular numerical techniques is the finite-difference time-domain (FDTD) technique. Numerical simulation tools like the FDTD technique enable detailed visualization of electromagnetic fields within complicated optical waveguides systems. A limitation

of the FDTD technique is the massive computation power and processing time required to complete a simulation. Because only one combination of parameters can be explored for a given simulation, hundreds or thousands of simulations are required to completely map out the frequency-dependent electromagnetic response of an optical waveguide for various material combinations and geometrical configurations. As a result, optimization using only numerical simulations is often not feasible.

In this thesis, we have explored a new analytical technique to analyze and optimize the performance of multi-axial waveguides. The technique consists of breaking the multi-axial waveguide down into simpler uni-axial waveguide sub-components. The uni-axial waveguides are modeled by analytically solving Maxwell's equations and mapping out the wavevector of the modes sustained by the waveguides. We hypothesized that efficient coupling between the uni-axial waveguide sub-components is achieved when the in-plane wavevector of the modes sustained by the waveguides are matched. In Chapters 3 and 4, we presented two design examples in which bi-axial waveguides are optimized, using the proposed methodology, to achieve high coupling efficiency. In both examples, the optimized parameters selected using our methodology is shown, through FDTD simulations, to yield maximum coupling efficiency.

5.1 Limitations

One of the major limitations of this technique is that the uni-axial waveguide sub-components are assumed to be infinitely-long, which is typically not

the case. For waveguides that extend over short distances comparable to or less than the wavelength, the uni-axial waveguide solutions may not accurately describe the electromagnetic properties of the actual system. Another major limitation of our methodology is that it cannot quantify the performance of multi-axial waveguides. The methodology only selects waveguide parameters that can potentially yield maximum coupling, but still requires numerical methods like the FDTD technique to rigorously model the waveguide performance. We thus envision that this technique can be potentially used as a supplement to numerical methods to provide first order estimates of optimal parameters.

5.2 Future Work

Future work aims to explore the application of this technique to design multi-axial waveguides composed of more than two uni-axial waveguides connected with each other non-perpendicular angles. Furthermore, we have thus far restricted our treatment to simple cases where the uni-axial waveguide components only sustain a single mode. Further work is needed to verify that this methodology still holds for waveguide systems that sustain more than one mode.

Bibliography

[1] K. Okamoto, *Fundamentals of Optical Waveguides*. Elsevier Inc., second ed., 2006.

[2] D. Colladon, "On the reflections of a ray of light inside a parabolic liquid stream," *Comptes Rendus*, vol. 15, pp. 800 – 802, 1842.

[3] R. J. Bates, *Optical Switching and Networking Handbook*. New York: McGraw Hill, 2001.

[4] M. Hoffmann, "Micromechanical cantilever resonators with integrated optical interrogation," *Sensors and Actuators A: Physical*, vol. 44, pp. 71 – 75, 1994.

[5] D. Christea *et al.*, "Micromachined photonic integrated circuits for sensor applications: experimental results," *Proceedings of SPIE*, vol. 3680, p. 1141, 1999.

[6] M. Ohkawa *et al.*, "Silicon-based integrated optic pressure sensor using intermodal interference between tm-like and te-like modes," *Fiber and Integrated Optics*, vol. 21, pp. 105 – 113, 2002.

[7] M. W. Pruessner *et al.*, "Micromechanical resonators with integrated optical waveguides for sensing applications," *Conference on Lasers and*

Electro-Optics/Quantum Electronics and Laser Science and Photonic Applications Systems Technologies, p. CTuH5, 2005.

[8] N. R. Walker *et al.*, "Selective detection of gas-phase tnt by integrated optical waveguide spectrometry using molecularly imprinted solgel sensing films," *Analytica Chimica Acta*, vol. 593, pp. 82 – 91, 2007.

[9] C. L. Bliss *et al.*, "Rapid fabrication of a microfluidic device with integrated optical waveguides for dna fragment analysis," *Lab on a Chip*, vol. 7, pp. 1280 – 1287, 2007.

[10] G. P. Agrawal, *Fiber-Optic Communication Systems*. New York: Wiley, second ed., 2002.

[11] S. A. Maier, "Waveguiding, the best of both worlds," *Nature Photonics*, vol. 2, pp. 460 – 461, 2008.

[12] D. A. B. Miller, "Device requirements for optical interconnects to silicon chips," *Proceedings of IEEE*, vol. 97, p. 1166, 2009.

[13] E. Ozbay, "Plasmonics: Merging photonics and electronics at nanoscale dimensions," *Science*, vol. 311, p. 189, 2006.

[14] J. A. Dionne *et al.*, "Highly confined photon transport in subwavelength metallic slot waveguides," *Nano Letters*, vol. 6, pp. 1928 – 1932, 2006.

[15] J. Takahara *et al.*, "Guiding of a one-dimensional optical beam with nanometer diameter," *Optics Letters*, vol. 22, pp. 475 – 477, 1997.

[16] K. L. Kliewer and R. Fuchs, "Collective electronic motion in a metallic slab," *Physical Review*, vol. 153, p. 498, 1967.

[17] D. Sarid, "Long-range surface-plasma waves on very thin metal films," *Physical Review Letters*, vol. 47, pp. 844 – 846, 1981.

[18] F. Yang *et al.*, "Long-range surface modes supported by thin films," *Physical Review B*, vol. 44, pp. 5855 – 5872, 1991.

[19] J. J. Burke and G. I. Stegeman, "Surface-polariton-like waves guided by thin, lossy metal films," *Physical Review B*, vol. 33, pp. 5186 – 5201, 1986.

[20] M. Quinten *et al.*, "Electromagnetic energy transport via linear chains of silver nanoparticles.," *Optics Letters*, vol. 23, pp. 1331 – 1333, 1998.

[21] N. C. Panoiu and R. M. O. Jr., "Subwavelength nonlinear plasmonic nanowire," *Nano Letters*, vol. 4, pp. 2427 – 2430, 2004.

[22] J. Dorfmuller *et al.*, "Plasmonic nanowire antennas: Experiment, simulation, and theory," *Nano Letters*, vol. 10, pp. 3596 – 3603, 2010.

[23] R. F. Oulton *et al.*, "A hybrid plasmonic waveguide for subwavelength confinement and long-range propagation," *Nature Photonics*, vol. 2, pp. 496 – 500, 2008.

[24] J. P. Kottmann and O. J. F. Martin, "Plasmon resonant coupling in metallic nanowires," *Optics Express*, vol. 8, pp. 655 – 663, 2001.

[25] T. W. Ebbesen *et al.*, "Extraordinary optical transmission through subwavelength hole arrays," *Nature*, vol. 391, pp. 667 – 669, 1998.

[26] J. Chen *et al.*, "Surface plasmon modes of finite, planar, metal-insulator-metal plasmonic waveguides," *Optics Express*, vol. 16, pp. 14902 – 14909, 2008.

[27] R. Zia *et al.*, "Geometries and materials for subwavelength surface plasmon modes," *Journal of Optical Society of America*, vol. 12, pp. 2442 – 2446, 2004.

[28] J. C. Maxwell, *A treatise on electricity and magnetism.* Oxford Press, 1873.

[29] P. Drude, "Zur elektronentheorie der metalle," *Annalen Der Physik*, vol. 306, p. 506, 1900.

[30] P. Drude, "Zur elektronentheorie der metalle; ii. teil. galvanomagnetische und thermomagnetische effecte," *Annalen Der Physik*, vol. 308, p. 369, 1900.

[31] N. W. Ashcroft and N. D. Mermin, *Solid State Physics.* Saunders, 1976.

[32] A. P. French, *Vibrations and Waves.* Norton, 1971.

[33] C. Kittel, *Introduction to Solid State Physics.* New York: Wiley, seventh ed., 1996.

[34] S. A. Maier, *Plasmonics: Fundamentals and Applications.* New York: Springer Science, first ed., 2007.

[35] E. J. Zeman and G. C. Schatz, "An accurate electromagnetic theory study of surface enhancement factors for silver, gold, copper, lithium,

sodium, aluminum, gallium, indium, zinc, and cadmium," *Journal of Physical Chemistry*, vol. 91, pp. 634 – 643, 1987.

[36] P. B. Johnson and R. W. Christy, "Optical constants of the noble metals," *Physical Review B*, vol. 6, pp. 4370 – 4379, 1972.

[37] A. Vial *et al.*, "Improved analytical fit of gold dispersion: Application to the modeling of extinction spectra with a finite-difference-time-domain method," *Physical Review B*, vol. 71, 2005.

[38] S. C. Her and Y. H. Wang, "Optical and mechanical properties of silver film on glass substrate," *Advanced Materials Research*, vol. 97 - 101, pp. 1412 – 1415, 2010.

[39] I. El-Kady *et al.*, "Metallic photonic crystals at optical wavelengths," *Physical Review B*, vol. 62, 2000.

[40] J. Chilwell and I. Hodgkinson, "Thin films field-transfer matrix theory of planar multilayer waveguides and reflection from prism-loaded waveguides," *Journal of Optical Society of America A*, vol. 1, pp. 742 – 753, 1984.

[41] C. Chen *et al.*, "Efficient and accurate numerical analysis of multilayer planar optical waveguides in lossy anisotropic media," *Optics Express*, vol. 7, pp. 260 – 272, 2000.

[42] E. Verhaugen, "Subwavelength light confinement with surface plasmon polaritons.," *Ph.D. Thesis, Utrecht University*, vol. 18, 2009.

[43] H. A. N. Hejase, "On the use of davidenko's method in complex root search," *IEEE Transactions on Microwave Theory and Techniques*, vol. 41, pp. 141 – 143, 1993.

[44] D. F. Davidenko, "On a new method of numerical solution of systems of nonlinear equations," *Doklady Akad Nauk S.S.S.R*, vol. 88, pp. 601 – 602, 1953.

[45] D. F. Davidenko, "On the approximate solution of systems of nonlinear equations," *Ukraininan Mathematics Journal*, vol. 5, pp. 196 – 206, 1953.

[46] D. F. Davidenko, "An iterative method of parameter variation for inverting linear operators," *USSR Computational Mathematics and Mathematical Physics*, vol. 15, pp. 27 – 44, 1975.

[47] S. H. Talisa, "Application of davidenkos method to the solution of dispersion relations in lossy waveguiding systems," *IEEE Transactions on Microwave Theory and Techniques*, vol. 33, pp. 967 – 971, 1985.

[48] R. L. Espinola *et al.*, "A study of high-index-contrast 90^0 waveguide bend structures," *Optics Express*, vol. 8, pp. 517 – 528, 2001.

[49] C. Manolatou *et al.*, "Highdensity integrated optics," *Journal of Light wave Technology*, vol. 17, pp. 1682 – 1692, 1999.

[50] S. Y. Lin *et al.*, "Experimental demonstration of guiding and bending of electromagnetic waves in a photonic crystal," *Science*, vol. 282, pp. 274 – 276, 1998.

[51] G. Veronis and S. Fan, "Bends and splitters in metal-dielectric-metal subwavelength plasmonic waveguides," *Applied Physics Letters*, vol. 87, pp. 131102(1 – 3), 2005.

[52] L. Liu *et al.*, "Novel surface plasmon waveguide for high integration," *Optics Express*, vol. 13, pp. 6645 – 6650, 2005.

[53] T. W. Lee and S. K. Gray, "Subwavelength light bending by metal slit structure," *Optics Express*, vol. 13, pp. 9652 – 9659, 2005.

[54] K. Yee, "Numerical solution of initial boundary value problems involving maxwell's equations in isotropic media," *IEEE Transactions on Antennas and Propagation*, vol. 14, pp. 302 – 307, 1966.

[55] A. Taflove, "Application of the finite-difference time-domain method to sinusoidal steady state electromagnetic penetration problems," *IEEE Transactions on Electromagnetic Compatibility*, vol. 22, pp. 191 – 202, 1980.

[56] J. Berenger, "A perfectly matched layer for the absorption of electromagnetic waves," *Journal of Computational Physics*, vol. 114, pp. 185 – 200, 1994.

[57] S. D. Gedney, "An anisotropic perfectly matched layer absorbing media for the truncation of fdtd lattices," *IEEE Transactions on Antennas and Propagation*, vol. 44, pp. 1630 – 1639, 1996.

[58] S. A. Maier *et al.*, "Plasmonics - a route to nanoscale optical devices," *Advance Materials*, vol. 13, pp. 1501 – 1505, 2001.

[59] T. Nikolajsen *et al.*, "Polymer-based surface-plasmon-polariton stripe waveguides at telecommunication wavelengths," *Applied Physics Letters*, vol. 82, pp. 668 – 670, 2003.

[60] R. Mehfuz *et al.*, "Enhancing the efficiency of slit-coupling to surface-plasmon-polaritons via dispersion engineering," *Optics Express*, vol. 18, pp. 18206–18216, 2010.

[61] P. Lalanne *et al.*, "Theory of surface plasmon generation at nanoslit apertures," *Physical Review Letters*, vol. 95, p. 263902, 2005.

[62] P. Lalanne *et al.*, "Approximate model for surface-plasmon generation at slit apertures," *Journal of Optical Society of America A*, vol. 23, pp. 1608 – 1615, 2006.

[63] S. Astilean *et al.*, "Light transmission through metallic channels much smaller than the wavelength," *Optical Communication*, vol. 175, pp. 265 – 273, 2000.

[64] H. W. Kihm *et al.*, "Control of surface plasmon generation efficiency by slit-width tuning," *Applied Physics Letters*, vol. 92, p. 051115, 2008.

[65] O. T. A. Janssen *et al.*, "On the phase of plasmons excited by slits in a metal film," *Optics Express*, vol. 14, pp. 11823 – 11832, 2006.

[66] Y. Takakura, "Optical resonance in a narrow slit in a thick metallic screen," *Physical Review Letters*, vol. 86, pp. 5601 – 5603, 2001.

[67] M. W. Kowarz, "Homogeneous and evanescent contributions in scalar near-field diffraction," *Applied Optics*, vol. 34, pp. 3055 – 3063, 1995.

Appendix: Fit Functions

In Chapters 3 and 4, we discussed the design of multi-axial metallic waveguides using the solutions to dispersion relations for uni-axial metallic waveguides. Dispersion relations for uni-axial metallic waveguides are generally complex transcendental equations which are difficult to solve using simple algebraic techniques and require sophisticated iterative techniques. These iterative techniques are usually time consuming and their convergence to a stable solution requires a good initial guess value. Here, we present explicit analytical piece-wise fit functions for the solutions to dispersion relations of various metallic waveguide structures. These explicit expressions can be used to approximate the complex wavevector or serve as an initial guess for iterative solution implementations.

SPP Mode in a Silver-Dielectric-Silver Waveguide

We obtain piece-wise fit functions to the dispersion relations of the symmetric SPP mode over frequencies where it is propagative. The fit functions for the symmetric SPP mode can be given for different dielectric cores as:

Dielectric Core $n = 1.0$

$\omega = 8.5 \times 10^{14} - 8.75 \times 10^{14}$ (Hz) and $t = 150\text{nm} - 300\text{nm}$

$$\begin{aligned}\beta &= 1.72173 \times 10^{7} - 8.2303 \times 10^{-8}\omega - 1.32669 \times 10^{14}t \\ &\quad +1.20818 \times 10^{-22}\omega^2 + 9.33943 \times 10^{19}t^2 + 0.09494\omega t\end{aligned}$$

$\omega = 8.5 \times 10^{14} - 8.75 \times 10^{14}$ (Hz) and $t = 50\text{nm} - 150\text{nm}$

$$\begin{aligned}\beta &= -2.09062 \times 10^{7} - 3.46651 \times 10^{-8}\omega + 1.09635 \times 10^{14}t \\ &\quad +1.39199 \times 10^{-22}\omega^2 + 8.8537 \times 10^{20}t^2 - 0.45034\omega t\end{aligned}$$

$\omega = 3.5 \times 10^{14} - 8.5 \times 10^{14}$ (Hz) and $t = 150\text{nm} - 300\text{nm}$

$$\begin{aligned}\beta &= 6.12927 \times 10^{6} + 3.20113 \times 10^{-8}\omega + -6.05407 \times 10^{-23}\omega^2 \\ &\quad +2.00357 \times 10^{-37}\omega^3 + -3.16232 \times 10^{-52}\omega^4 + 1.93617 \times 10^{-67}\omega^5 \\ &\quad -9.32617 \times 10^{13}t + 5.71877 \times 10^{20}t^2 - 1.95536 \times 10^{27}t^3 \\ &\quad +3.57259 \times 10^{33}t^4 - 2.7277 \times 10^{39}t^5\end{aligned}$$

$\omega = 4.75 \times 10^{14} - 8.2 \times 10^{14}$ (Hz) and $t = 50\text{nm} - 150\text{nm}$

$$\begin{aligned}\beta &= 89293.84003 - 1.72137 \times 10^{-7}\omega + 6.77262 \times 10^{-22}\omega^2 \\ &\quad -1.08811 \times 10^{-36}\omega^3 + 7.76656 \times 10^{-52}\omega^4 - 1.62355 \times 10^{-67}\omega^5 \\ &\quad +1.21543 \times 10^{15}t - 2.30847 \times 10^{22}t^2 + 2.04098 \times 10^{29}t^3 \\ &\quad -8.71403 \times 10^{35}t^4 + 1.45453 \times 10^{42}t^5\end{aligned}$$

Dielectric core n = 1.5

$\omega = 3.5 \times 10^{14} - 7.5 \times 10^{14}$ (Hz) and $t = 120\text{nm} - 300\text{nm}$

$$\begin{aligned}\beta &= -8.18148 \times 10^{7} + 1.09905 \times 10^{-6}\omega - 4.73456 \times 10^{-21}\omega^2 \\ &\quad +1.04218 \times 10^{-35}\omega^3 - 1.13622 \times 10^{-50}\omega^4 + 4.93144 \times 10^{-66}\omega^5 \\ &\quad -2.19077E14t + 1.63401 \times 10^{21}t^2 - 6.56117E27t^3 \\ &\quad +1.36474 \times 10^{34}t^4 - 1.15377 \times 10^{40}t^5\end{aligned}$$

$\omega = 3.5 \times 10^{14} - 6 \times 10^{14}$ (Hz) and $t = 10\text{nm} - 80\text{nm}$

$$\begin{aligned}\beta &= -5.75014 \times 10^{7} + 3.15718 \times 10^{11} e^{-e^{\left(\frac{1.96374\times10^{15}-\omega}{1.11855\times10^{15}}\right)}} \\ &\quad +6.34943 \times 10^{7} e^{-e^{\left(\frac{-7.35261\times10^{-8}-t}{1.43303\times10^{-8}}\right)}} \\ &\quad -3.15122 \times 10^{11} e^{\left(-e^{\left(\frac{1.96374\times10^{15}-\omega}{1.11855\times10^{15}}\right)} - e^{\left(\frac{-7.35261\times10^{-8}-t}{1.43303\times10^{-8}}\right)}\right)}\end{aligned}$$

$\omega = 6 \times 10^{14} - 7.5 \times 10^{14}$ (Hz)

$t = 50\text{nm} - 80\text{nm}$

$$\begin{aligned}\beta &= 8.3505 \times 10^{6} + 6.23672 \times 10^{8} e^{-e^{\left(\frac{1.14896\times10^{15}-\omega}{4.84616\times10^{14}}\right)}} \\ &\quad +6.66111 \times 10^{6} e^{-e^{\left(\frac{5.69646\times10^{-8}-t}{7.42459\times10^{-8}}\right)}} \\ &\quad -6.82193 \times 10^{8} e^{\left(-e^{\left(\frac{1.14896\times10^{15}-\omega}{4.84616\times10^{14}}\right)} - e^{\left(\frac{5.69646\times10^{-8}-t}{7.42459\times10^{-8}}\right)}\right)}\end{aligned}$$

$\omega = 6 \times 10^{14} - 7.5 \times 10^{14}$ (Hz)

$t = 5\text{nm}-30\text{nm}$

$$\begin{aligned}\beta &= 3.6674\times10^{7} + 1.90183\times10^{9}e^{-e^{\left(\frac{1.14951\times10^{15}-\omega}{3.07971\times10^{14}}\right)}} \\ &\quad +1.36918\times10^{8}e^{-e^{\left(\frac{4.09602\times10^{-9}-t}{-7.24051\times10^{-9}}\right)}} \\ &\quad +2.03376\times10^{10}e^{\left(-e^{\left(\frac{1.14951\times10^{15}-\omega}{3.07971\times10^{14}}\right)} - e^{\left(\frac{4.09602\times10^{-9}-t}{-7.24051\times10^{-9}}\right)}\right)}\end{aligned}$$

$\omega = 6\times10^{14} - 7.5\times10^{14}$ (Hz)

$t = 30\text{nm}-50\text{nm}$

$$\begin{aligned}\beta &= 1.07351\times10^{6} + 1.27678\times10^{9}e^{-e^{\left(\frac{1.14951\times10^{15}-\omega}{4.57803\times10^{14}}\right)}} \\ &\quad +2.49982\times10^{7}e^{-e^{\left(\frac{2.83143\times10^{-8}-t}{3.64897\times10^{-8}}\right)}} \\ &\quad -1.74087\times10^{9}e^{\left(-e^{\left(\frac{1.14951\times10^{15}-\omega}{4.57803\times10^{14}}\right)} - e^{\left(\frac{2.83143\times10^{-8}-t}{3.64897\times10^{-8}}\right)}\right)}\end{aligned}$$

$\omega = 3.5\times10^{14} - 6\times10^{14}$ (Hz)

$t = 80\text{nm}-120\text{nm}$

$$\begin{aligned}\beta &= -814849.18221 + 4.41699E\times10^{-8}\omega + 1.16474\times10^{13}t \\ &\quad +1.06179\times10^{-23}\omega^{2} + 1.32263\times10^{14}t^{2} - 0.10634\omega t\end{aligned}$$

$\omega = 6\times10^{14} - 7.5\times10^{14}$ (Hz)

$t = 80\text{nm}-120\text{nm}$

$$\beta = 2.28031\times10^{7} - 9.72998\times10^{-8}\omega + 1.75929\times10^{14}t$$

$$+1.78671 \times 10^{-22}\omega^2 - 7.58382 \times 10^{14}t^2 - 0.37664\omega t$$

Dielectric core n = 2.0

$\omega = 3 \times 10^{14} - 6 \times 10^{14}$ (Hz)

$t = 120\text{nm} - 300\text{nm}$

$$\begin{aligned}\beta &= -1.97964 \times 10^7 + 1.6671 \times 10^9 e^{-e^{\left(\frac{2.85129\times10^{15}-\omega}{1.97609\times10^{15}}\right)}} \\ &\quad +7.20147 \times 10^6 e^{-e^{\left(\frac{-8.48997\times10^{-9}-t}{6.252\times10^{-8}}\right)}} \\ &\quad -6.73854 \times 10^8 e^{\left(-e^{\left(\frac{2.85129\times10^{15}-\omega}{1.97609\times10^{15}}\right)} - e^{\left(\frac{-8.48997\times10^{-9}-t}{6.252\times10^{-8}}\right)}\right)}\end{aligned}$$

$\omega = 6.5 \times 10^{14} - 7.1 \times 10^{14}$ (Hz)

$t = 120\text{nm} - 300\text{nm}$

$$\begin{aligned}\beta &= 3.51039 \times 10^7 + 7.55202 \times 10^9 e^{-e^{\left(\frac{1.00296\times10^{15}-\omega}{1.76148\times10^{14}}\right)}} \\ &\quad -1.86391 \times 10^6 e^{-e^{\left(\frac{4.00369\times10^{-7}-t}{2.17345\times10^{-9}}\right)}} \\ &\quad 6.00459 \times 10^7 e^{\left(-e^{\left(\frac{1.00296\times10^{15}-\omega}{1.76148\times10^{14}}\right)} - e^{\left(\frac{4.00369\times10^{-7}-t}{2.17345\times10^{-9}}\right)}\right)}\end{aligned}$$

$\omega = 6.0 \times 10^{14} - 6.5 \times 10^{14}$ (Hz)

$t = 120\text{nm} - 300\text{nm}$

$$\begin{aligned}\beta &= 2.82033 \times 10^7 + 1.52588 \times 10^8 e^{-e^{\left(\frac{7.86251\times10^{14}-\omega}{1.46422\times10^{14}}\right)}} \\ &\quad 6.00435 \times 10^9 e^{-e^{\left(\frac{-6.37561\times10^{-7}-t}{-3.68951\times10^{-7}}\right)}}\end{aligned}$$

$$-3.31606 \times 10^{10} e^{\left(-e^{\left(\frac{7.86251\times10^{14}-\omega}{1.46422\times10^{14}}\right)} - e^{\left(\frac{-6.37561\times10^{-7}-t}{-3.68951\times10^{-7}}\right)}\right)}$$

$\omega = 3.0 \times 10^{14} - 6.0 \times 10^{14}$ (Hz)

$t = 30\text{nm} - 120\text{nm}$

$$\begin{aligned}\beta &= -3.53696 \times 10^{7} + 3.13797 \times 10^{9} e^{-e^{\left(\frac{4.46772\times10^{15}-\omega}{2.98473\times10^{15}}\right)}} \\ &\quad 1.13447 \times 10^{7} e^{-e^{\left(\frac{4.94075\times10^{-8}-t}{2.12237\times10^{-8}}\right)}} \\ &\quad -9.25342 \times 10^{8} e^{\left(-e^{\left(\frac{4.46772\times10^{15}-\omega}{2.98473\times10^{15}}\right)} - e^{\left(\frac{4.94075\times10^{-8}-t}{2.12237\times10^{-8}}\right)}\right)}\end{aligned}$$

$\omega = 6.0 \times 10^{14} - 6.5 \times 10^{14}$ (Hz)

$t = 30\text{nm} - 120\text{nm}$

$$\begin{aligned}\beta &= 3.83428 \times 10^{7} + 1.87655 \times 10^{8} e^{-e^{\left(\frac{7.82176\times10^{14}-\omega}{1.65181\times10^{14}}\right)}} \\ &\quad -9.72658 \times 10^{6} e^{-e^{\left(\frac{5.01303\times10^{-8}-t}{1.94477\times10^{-8}}\right)}} \\ &\quad -6.92474 \times 10^{7} e^{\left(-e^{\left(\frac{7.82176\times10^{14}-\omega}{1.65181\times10^{14}}\right)} - e^{\left(\frac{5.01303\times10^{-8}-t}{1.94477\times10^{-8}}\right)}\right)}\end{aligned}$$

$\omega = 6.5 \times 10^{14} - 7.1 \times 10^{14}$ (Hz)

$t = 30\text{nm} - 120\text{nm}$

$$\begin{aligned}\beta &= 5.28234 \times 10^{7} + 1.21942 \times 10^{9} e^{-e^{\left(\frac{8.78901\times10^{14}-\omega}{1.36591\times10^{14}}\right)}} \\ &\quad -1.55391 \times 10^{7} e^{-e^{\left(\frac{5.07127\times10^{-8}-t}{1.661\times10^{-8}}\right)}}\end{aligned}$$

$$-2.37427 \times 10^{8} e^{\left(-e^{\left(\frac{8.78901\times10^{14}-\omega}{1.36591\times10^{14}}\right)} - e^{\left(\frac{5.07127\times10^{-8}-t}{1.661\times10^{-8}}\right)}\right)}$$

$\omega = 3.0 \times 10^{14} - 5.5 \times 10^{14}$ (Hz)

$t = 5\text{nm} - 30\text{nm}$

$$\begin{aligned}\beta &= 2.83643 \times 10^{6} + 1.89939 \times 10^{9} e^{-e^{\left(\frac{2.22083\times10^{15}-\omega}{1.28216\times10^{15}}\right)}} \\ &\quad -7.36171 \times 10^{7} e^{-e^{\left(\frac{3.56358\times10^{-9}-t}{-7.72401\times10^{-9}}\right)}} \\ &\quad 1.32238 \times 10^{10} e^{\left(-e^{\left(\frac{2.22083\times10^{15}-\omega}{1.28216\times10^{15}}\right)} - e^{\left(\frac{3.56358\times10^{-9}-t}{-7.72401\times10^{-9}}\right)}\right)}\end{aligned}$$

$\omega = 5.5 \times 10^{14} - 7.1 \times 10^{14}$ (Hz)

$t = 5\text{nm} - 30\text{nm}$

$$\begin{aligned}\beta &= 4.82025 \times 10^{7} + 1.71088 \times 10^{10} e^{-e^{\left(\frac{1.32937\times10^{15}-\omega}{3.69429\times10^{14}}\right)}} \\ &\quad 2.17774 \times 10^{8} e^{-e^{\left(\frac{4.15853\times10^{-9}-t}{-7.20353\times10^{-9}}\right)}} \\ &\quad 1.70486 \times 10^{11} e^{\left(-e^{\left(\frac{1.32937\times10^{15}-\omega}{3.69429\times10^{14}}\right)} - e^{\left(\frac{4.15853\times10^{-9}-t}{-7.20353\times10^{-9}}\right)}\right)}\end{aligned}$$

Dielectric core n= 2.5

$\omega = 2.5 \times 10^{14} - 5.5 \times 10^{14}$ (Hz)

$t = 100\text{nm} - 300\text{nm}$

$$\beta = -7.2073 \times 10^{6} + 2.59213 \times 10^{9} e^{-e^{\left(\frac{2.8552\times10^{15}-\omega}{1.74298\times10^{15}}\right)}}$$

$$-1.79057 \times 10^{6} e^{-e^{\left(\frac{1.3725\times10^{-8}-t}{6.04451\times10^{-8}}\right)}}$$
$$-5.96339 \times 10^{8} e^{\left(-e^{\left(\frac{2.8552\times10^{15}-\omega}{1.74298\times10^{15}}\right)} - e^{\left(\frac{1.3725\times10^{-8}-t}{6.04451\times10^{-8}}\right)}\right)}$$

$\omega = 5.5 \times 10^{14} - 6.0 \times 10^{14}$ (Hz)

$t = 100\text{nm} - 300\text{nm}$

$$\begin{aligned}\beta &= 3.4993 \times 10^{7} + 1.27119 \times 10^{8} e^{-e^{\left(\frac{6.79906\times10^{14}-\omega}{1.08599\times10^{14}}\right)}} \\ &\quad 1.70174 \times 10^{9} e^{-e^{\left(\frac{-3.33857\times10^{-7}-t}{-2.34925\times10^{-7}}\right)}} \\ &\quad -6.89123 \times 10^{9} e^{\left(-e^{\left(\frac{6.79906\times10^{14}-\omega}{1.08599\times10^{14}}\right)} - e^{\left(\frac{-3.33857\times10^{-7}-t}{-2.34925\times10^{-7}}\right)}\right)}\end{aligned}$$

$\omega = 6 \times 10^{14} - 6.5 \times 10^{14}$ (Hz)

$t = 100\text{nm} - 300\text{nm}$

$$\begin{aligned}\beta &= 5.61033 \times 10^{7} + 1.78816 \times 10^{9} e^{-e^{\left(\frac{8.13426\times10^{14}-\omega}{1.15717\times10^{14}}\right)}} \\ &\quad -8.70104 \times 10^{6} e^{-e^{\left(\frac{6.83944\times10^{-8}-t}{2.04979\times10^{-8}}\right)}} \\ &\quad 5.80717 \times 10^{8} e^{\left(-e^{\left(\frac{8.13426\times10^{14}-\omega}{1.15717\times10^{14}}\right)} - e^{\left(\frac{6.83944\times10^{-8}-t}{2.04979\times10^{-8}}\right)}\right)}\end{aligned}$$

$\omega = 2.5 \times 10^{14} - 5.5 \times 10^{14}$ (Hz)

$t = 50\text{nm} - 100\text{nm}$

$$\beta = -6.45697 \times 10^{7} + 1.37518 \times 10^{9} e^{-e^{\left(\frac{3.10394\times10^{15}-\omega}{2.75231\times10^{15}}\right)}}$$

$$1.43777 \times 10^{7} e^{-e^{\left(\frac{8.76514\times10^{-8}-t}{4.37752\times10^{-8}}\right)}}$$
$$-3.05341 \times 10^{8} e^{\left(-e^{\left(\frac{3.10394\times10^{15}-\omega}{2.75231\times10^{15}}\right)} - e^{\left(\frac{8.76514\times10^{-8}-t}{4.37752\times10^{-8}}\right)}\right)}$$

$\omega = 5.5 \times 10^{14} - 6.0 \times 10^{14}$ (Hz)

$t = 50\text{nm} - 100\text{nm}$

$$\begin{aligned}\beta &= 3.39926 \times 10^{7} + 2.51503 \times 10^{8} e^{-e^{\left(\frac{7.99154\times10^{14}-\omega}{2.85374\times10^{14}}\right)}} \\ &\quad -3.40492 \times 10^{7} e^{-e^{\left(\frac{8.81644\times10^{-8}-t}{1.69038\times10^{-7}}\right)}} \\ &\quad -4.69014 \times 10^{7} e^{\left(-e^{\left(\frac{7.99154\times10^{14}-\omega}{2.85374\times10^{14}}\right)} - e^{\left(\frac{8.81644\times10^{-8}-t}{1.69038\times10^{-7}}\right)}\right)}\end{aligned}$$

$\omega = 6.0 \times 10^{14} - 6.5 \times 10^{14}$ (Hz)

$t = 50\text{nm} - 100\text{nm}$

$$\begin{aligned}\beta &= 3.73922 \times 10^{7} + 5.68088 \times 10^{8} e^{-e^{\left(\frac{7.9886\times10^{14}-\omega}{1.65266\times10^{14}}\right)}} \\ &\quad -4.98983 \times 10^{7} e^{-e^{\left(\frac{1.50844\times10^{-7}-t}{1.18004\times10^{-7}}\right)}} \\ &\quad 4.13079 \times 10^{8} e^{\left(-e^{\left(\frac{7.9886\times10^{14}-\omega}{1.65266\times10^{14}}\right)} - e^{\left(\frac{1.50844\times10^{-7}-t}{1.18004\times10^{-7}}\right)}\right)}\end{aligned}$$

$\omega = 1.5 \times 10^{14} - 5 \times 10^{14}$ (Hz)

$t = 5\text{nm} - 50\text{nm}$

$$\beta = -6.19853 \times 10^{8} + 4.75358 \times 10^{10} e^{-e^{\left(\frac{1.25148\times10^{15}-\omega}{7.88071\times10^{14}}\right)}}$$

$$6.25779 \times 10^{8} e^{-e^{\left(\frac{-1.0823\times10^{-8}-t}{4.90041\times10^{-9}}\right)}}$$
$$-4.69103 \times 10^{10} e^{\left(-e^{\left(\frac{1.25148\times10^{15}-\omega}{7.88071\times10^{14}}\right)} - e^{\left(\frac{-1.0823\times10^{-8}-t}{4.90041\times10^{-9}}\right)}\right)}$$

$\omega = 5 \times 10^{14} - 6.5 \times 10^{14}$ (Hz)

$t = 5\text{nm} - 50\text{nm}$

$$\begin{aligned}\beta &= 4.62771 \times 10^{7} + 5.12298 \times 10^{10} e^{-e^{\left(\frac{1.57816\times10^{15}-\omega}{4.94713\times10^{14}}\right)}} \\ &\quad 2.02722 \times 10^{11} e^{-e^{\left(\frac{-7.59034\times10^{-8}-t}{-3.93686\times10^{-8}}\right)}} \\ &\quad 4.89833 \times 10^{14} e^{\left(-e^{\left(\frac{1.57816\times10^{15}-\omega}{4.94713\times10^{14}}\right)} - e^{\left(\frac{-7.59034\times10^{-8}-t}{-3.93686\times10^{-8}}\right)}\right)}\end{aligned}$$

Dielectric core n = 3.0

$\omega = 2.5 \times 10^{14} - 5 \times 10^{14}$ (Hz)

$t = 100\text{nm} - 300\text{nm}$

$$\begin{aligned}\beta &= 2.88107 \times 10^{7} + 2.13426 \times 10^{9} e^{-e^{\left(\frac{1.95942\times10^{15}-\omega}{1.04187\times10^{15}}\right)}} \\ &\quad -2.47784 \times 10^{7} e^{-e^{\left(\frac{-1.87313\times10^{-8}-t}{5.74129\times10^{-8}}\right)}} \\ &\quad 2.14085 \times 10^{8} e^{\left(-e^{\left(\frac{1.95942\times10^{15}-\omega}{1.04187\times10^{15}}\right)} - e^{\left(\frac{-1.87313\times10^{-8}-t}{5.74129\times10^{-8}}\right)}\right)}\end{aligned}$$

$\omega = 5 \times 10^{14} - 6 \times 10^{14}$ (Hz)

$t = 100\text{nm} - 300\text{nm}$

$$\begin{aligned}\beta &= 4.67772 \times 10^7 + 3.21912 \times 10^9 e^{-e^{\left(\frac{8.07685\times10^{14}-\omega}{1.50667\times10^{14}}\right)}} \\ &\quad 402975.77697 e^{-e^{\left(\frac{4.50521\times10^{-7}-t}{3.73193\times10^{-8}}\right)}} \\ &\quad 1.06579 \times 10^8 e^{\left(-e^{\left(\frac{8.07685\times10^{14}-\omega}{1.50667\times10^{14}}\right)} - e^{\left(\frac{4.50521\times10^{-7}-t}{3.73193\times10^{-8}}\right)}\right)}\end{aligned}$$

$\omega = 2.5 \times 10^{14} - 5 \times 10^{14}$ (Hz)

$t = 50\text{nm} - 100\text{nm}$

$$\begin{aligned}\beta &= -5.89053 \times 10^7 + 1.51844 \times 10^9 e^{-e^{\left(\frac{2.60327\times10^{15}-\omega}{2.18067\times10^{15}}\right)}} \\ &\quad 1.10074 \times 10^7 e^{-e^{\left(\frac{8.7235\times10^{-8}-t}{4.68116\times10^{-8}}\right)}} \\ &\quad -3.0804 \times 10^8 e^{\left(-e^{\left(\frac{2.60327\times10^{15}-\omega}{2.18067\times10^{15}}\right)} - e^{\left(\frac{8.7235\times10^{-8}-t}{4.68116\times10^{-8}}\right)}\right)}\end{aligned}$$

$\omega = 5.5 \times 10^{14} - 5.8 \times 10^{14}$ (Hz)

$t = 50\text{nm} - 100\text{nm}$

$$\begin{aligned}\beta &= 3.43401 \times 10^7 + 5.50512 \times 10^9 e^{-e^{\left(\frac{8.34557\times10^{14}-\omega}{2.81694\times10^{14}}\right)}} \\ &\quad -4.59404 \times 10^7 e^{-e^{\left(\frac{1.32879\times10^{-7}-t}{1.28984\times10^{-7}}\right)}} \\ &\quad 3.23191 \times 10^8 e^{\left(-e^{\left(\frac{8.34557\times10^{14}-\omega}{2.81694\times10^{14}}\right)} - e^{\left(\frac{1.32879\times10^{-7}-t}{1.28984\times10^{-7}}\right)}\right)}\end{aligned}$$

$\omega = 5.8 \times 10^{14} - 6.0 \times 10^{14}$ (Hz)

$t = 50\text{nm}-100\text{nm}$

$$\begin{aligned}\beta &= 5.54605\times10^{7} + 5.88966\times10^{8}e^{-e^{\left(\frac{6.81188\times10^{14}-\omega}{9.463\times10^{13}}\right)}} \\ &\quad -5.96491\times10^{7}e^{-e^{\left(\frac{1.29969\times10^{-7}-t}{2.57514\times10^{-7}}\right)}} \\ &\quad 5.94126\times10^{8}e^{\left(-e^{\left(\frac{6.81188\times10^{14}-\omega}{9.463\times10^{13}}\right)} - e^{\left(\frac{1.29969\times10^{-7}-t}{2.57514\times10^{-7}}\right)}\right)}\end{aligned}$$

$\omega = 2.5\times10^{14} - 4.0\times10^{14}$ (Hz)

$t = 5\text{nm}-50\text{nm}$

$$\begin{aligned}\beta &= -4.87592\times10^{9} + 2.31914\times10^{11}e^{-e^{\left(\frac{4.98913\times10^{14}-\omega}{3.06452\times10^{14}}\right)}} \\ &\quad 4.88724\times10^{9}e^{-e^{\left(\frac{-2.6278\times10^{-8}-t}{5.00396\times10^{-9}}\right)}} \\ &\quad -2.31762\times10^{11}e^{\left(-e^{\left(\frac{4.98913\times10^{14}-\omega}{3.06452\times10^{14}}\right)} - e^{\left(\frac{-2.6278\times10^{-8}-t}{5.00396\times10^{-9}}\right)}\right)}\end{aligned}$$

$\omega = 4.0\times10^{14} - 6.0\times10^{14}$ (Hz)

$t = 20\text{nm}-50\text{nm}$

$$\begin{aligned}\beta &= -1.12192\times10^{6} + 8.92744\times10^{9}e^{-e^{\left(\frac{1.63305\times10^{15}-\omega}{7.77546\times10^{14}}\right)}} \\ &\quad 1.71474\times10^{7}e^{-e^{\left(\frac{2.54566\times10^{-8}-t}{3.20063\times10^{-8}}\right)}} \\ &\quad -9.24941\times10^{9}e^{\left(-e^{\left(\frac{1.63305\times10^{15}-\omega}{7.77546\times10^{14}}\right)} - e^{\left(\frac{2.54566\times10^{-8}-t}{3.20063\times10^{-8}}\right)}\right)}\end{aligned}$$

$\omega = 4.0\times10^{14} - 6.0\times10^{14}$ (Hz)

$t = 5\text{nm}-20\text{nm}$

$$\begin{aligned}\beta &= 5.5263\times10^{7} + 5.33629\times10^{10}e^{-e^{\left(\frac{1.52435\times10^{15}-\omega}{5.03452\times10^{14}}\right)}} \\ &\quad 2.58337\times10^{8}e^{-e^{\left(\frac{4.26971\times10^{-9}-t}{-7.10258\times10^{-9}}\right)}} \\ &\quad 4.69963\times10^{11}e^{\left(-e^{\left(\frac{1.52435\times10^{15}-\omega}{5.03452\times10^{14}}\right)} - e^{\left(\frac{4.26971\times10^{-9}-t}{-7.10258\times10^{-9}}\right)}\right)}\end{aligned}$$

Dielectric core n = 3.5

$\omega = 2.7\times10^{14} - 5.0\times10^{14}$ (Hz)

$t = 100\text{nm}-300\text{nm}$

$$\begin{aligned}\beta &= 7.70898\times10^{6} + 8.58092\times10^{9}e^{-e^{\left(\frac{2.04069\times10^{15}-\omega}{9.57004\times10^{14}}\right)}} \\ &\quad -4.78262\times10^{6}e^{-e^{\left(\frac{3.83384\times10^{-7}-t}{1.54557\times10^{-8}}\right)}} \\ &\quad 5.36255\times10^{7}e^{\left(-e^{\left(\frac{2.04069\times10^{15}-\omega}{9.57004\times10^{14}}\right)} - e^{\left(\frac{3.83384\times10^{-7}-t}{1.54557\times10^{-8}}\right)}\right)}\end{aligned}$$

$\omega = 5.0\times10^{14} - 5.5\times10^{14}$ (Hz)

$t = 100\text{nm}-300\text{nm}$

$$\begin{aligned}\beta &= 6.63587\times10^{7} + 1.37356\times10^{9}e^{-e^{\left(\frac{6.35074\times10^{14}-\omega}{7.67264\times10^{13}}\right)}} \\ &\quad -7.41799\times10^{7}e^{-e^{\left(\frac{3.61797\times10^{-7}-t}{1.37614\times10^{-9}}\right)}} \\ &\quad 1.03749\times10^{9}e^{\left(-e^{\left(\frac{6.35074\times10^{14}-\omega}{7.67264\times10^{13}}\right)} - e^{\left(\frac{3.61797\times10^{-7}-t}{1.37614\times10^{-9}}\right)}\right)}\end{aligned}$$

$\omega = 2.5 \times 10^{14} - 4.8 \times 10^{14}$ (Hz)

$t = 40\text{nm} - 100\text{nm}$

$$\begin{aligned}\beta &= -5.45379 \times 10^{6} + 1.20082 \times 10^{10} e^{-e^{\left(\frac{2.82914 \times 10^{15} - \omega}{1.46163 \times 10^{13}}\right)}} \\ &\quad 1.0073 \times 10^{6} e^{-e^{\left(\frac{4.9367 \times 10^{-8} - t}{1.86263 \times 10^{-8}}\right)}} \\ &\quad -2.86019 \times 10^{9} e^{\left(-e^{\left(\frac{2.82914 \times 10^{15} - \omega}{1.46163 \times 10^{15}}\right)} - e^{\left(\frac{4.9367 \times 10^{-8} - t}{1.86263 \times 10^{-8}}\right)}\right)}\end{aligned}$$

$\omega = 4.8 \times 10^{14} - 5.5 \times 10^{14}$ (Hz)

$t = 40\text{nm} - 100\text{nm}$

$$\begin{aligned}\beta &= 7.1167 \times 10^{7} + 4.42601 \times 10^{9} e^{-e^{\left(\frac{7.71803 \times 10^{14} - \omega}{1.53727 \times 10^{14}}\right)}} \\ &\quad -1.71814 \times 10^{7} e^{-e^{\left(\frac{5.16071 \times 10^{-8} - t}{1.40188 \times 10^{-8}}\right)}} \\ &\quad 5.46782 \times 10^{8} e^{\left(-e^{\left(\frac{7.71803 \times 10^{14} - \omega}{1.53727 \times 10^{14}}\right)} - e^{\left(\frac{5.16071 \times 10^{-8} - t}{1.40188 \times 10^{-8}}\right)}\right)}\end{aligned}$$

$\omega = 2.5 \times 10^{14} - 5 \times 10^{14}$ (Hz)

$t = 20\text{nm} - 40\text{nm}$

$$\begin{aligned}\beta &= -1.16087 \times 10^{8} + 4.21399 \times 10^{9} e^{-e^{\left(\frac{1.86309 \times 10^{15} - \omega}{1.3616 \times 10^{15}}\right)}} \\ &\quad 1.55129 \times 10^{8} e^{-e^{\left(\frac{2.81664 \times 10^{-8} - t}{4.13305 \times 10^{-8}}\right)}} \\ &\quad -5.06593 \times 10^{9} e^{\left(-e^{\left(\frac{1.86309 \times 10^{15} - \omega}{1.3616 \times 10^{15}}\right)} - e^{\left(\frac{2.81664 \times 10^{-8} - t}{4.13305 \times 10^{-8}}\right)}\right)}\end{aligned}$$

$\omega = 5 \times 10^{14} - 5.5 \times 10^{14}$ (Hz)

$t = 20\text{nm} - 40\text{nm}$

$$\begin{aligned}\beta &= 1.06796 \times 10^{8} + 1.6759 \times 10^{9} e^{-e^{\left(\frac{6.72104\times10^{14}-\omega}{1.53218\times10^{14}}\right)}} \\ &\quad -1.49326 \times 10^{8} e^{-e^{\left(\frac{2.93069\times10^{-8}-t}{5.06187\times10^{-8}}\right)}} \\ &\quad -1.87427 \times 10^{9} e^{\left(-e^{\left(\frac{6.72104\times10^{14}-\omega}{1.53218\times10^{14}}\right)} - e^{\left(\frac{2.93069\times10^{-8}-t}{5.06187\times10^{-8}}\right)}\right)}\end{aligned}$$

$\omega = 2.5 \times 10^{14} - 4.5 \times 10^{14}$ (Hz)

$t = 20\text{nm} - 40\text{nm}$

$$\begin{aligned}\beta &= 9.25716 \times 10^{6} + 1.19191 \times 10^{9} e^{-e^{\left(\frac{1.06392\times10^{15}-\omega}{6.14568\times10^{14}}\right)}} \\ &\quad -9.9057 \times 10^{7} e^{-e^{\left(\frac{4.14344\times10^{-9}-t}{-7.18321\times10^{-9}}\right)}} \\ &\quad 9.86027 \times 10^{9} e^{\left(-e^{\left(\frac{1.06392\times10^{15}-\omega}{6.14568\times10^{14}}\right)} - e^{\left(\frac{4.14344\times10^{-9}-t}{-7.18321\times10^{-9}}\right)}\right)}\end{aligned}$$

$\omega = 4.5 \times 10^{14} - 5.5 \times 10^{14}$ (Hz)

$t = 20\text{nm} - 40\text{nm}$

$$\begin{aligned}\beta &= 8.62397 \times 10^{7} + 6.48528 \times 10^{10} e^{-e^{\left(\frac{1.05886\times10^{15}-\omega}{2.73221\times10^{14}}\right)}} \\ &\quad 5.25007 \times 10^{8} e^{-e^{\left(\frac{4.28125\times10^{-9}-t}{-7.07869\times10^{-9}}\right)}} \\ &\quad 5.17244 \times 10^{11} e^{\left(-e^{\left(\frac{1.05886\times10^{15}-\omega}{2.73221\times10^{14}}\right)} - e^{\left(\frac{4.28125\times10^{-9}-t}{-7.07869\times10^{-9}}\right)}\right)}\end{aligned}$$

TM_1 Mode in a Silver-Dielectric-Silver Waveguide

We obtain piece-wise fit functions to the dispersion relations of the TM_1 mode over frequencies where it is propagative. The fit functions for the TM_1 mode can be given for different dielectric cores as:

Dielectric core n = 1.0

For,

$\omega = 4.5 \times 10^{14} - 9 \times 10^{14}$ (Hz)

$t = 660 - 800$ nm

$$\begin{aligned} \beta &= -6.93061 \times 10^{7} + 9.10218 \times 10^{-8}\omega + 1.06405 \times 10^{14}t \\ &\quad -1.48057 \times 10^{-23}\omega^2 - 4.17409 \times 10^{19}t^2 - 0.05735\omega t. \end{aligned}$$

$\omega = 6 \times 10^{14} - 9 \times 10^{14}$ (Hz)

$t = 600 - 660$ nm

$$\begin{aligned} \beta &= -9.92251 \times 10^{7} + 1.33067 \times 10^{-7}\omega + 1.60785 \times 10^{14}t \\ &\quad -2.94254 \times 10^{-23}\omega^2 - 6.51506 \times 10^{19}t^2 - 0.0959\omega t. \end{aligned}$$

$\omega = 7.5 \times 10^{14} - 9 \times 10^{14}$ (Hz)

$t = 400 - 660$ nm

$$\begin{aligned}\beta &= -9.92251 \times 10^{7} + 1.33067 \times 10^{-7}\omega + 1.60785 \times 10^{14}t \\ &\quad -2.94254 \times 10^{-23}\omega^2 - 6.51506 \times 10^{19}t^2 - 0.0959\omega t.\end{aligned}$$

Dielectric core n = 1.5

For,

$\omega = 4 \times 10^{14} - 9 \times 10^{14}$ (Hz)

$t = 550 - 750$ nm

$$\begin{aligned}\beta &= -3.97487 \times 10^{7} + 8.22517 \times 10^{-8}\omega + 5.71795 \times 10^{13}t \\ &\quad -1.84235 \times 10^{-23}\omega^2 - 2.3324 \times 10^{19}t^2 - 0.03228\omega t.\end{aligned}$$

$\omega = 6 \times 10^{14} - 9 \times 10^{14}$ (Hz)

$t = 350 - 550$ nm

$$\begin{aligned}\beta &= -9.96598 \times 10^{7} + 1.63938 \times 10^{-7}\omega + 1.89559 \times 10^{14}t \\ &\quad -4.68169 \times 10^{-23}\omega^2 - 9.59265 \times 10^{19}t^2 - 0.12007\omega t.\end{aligned}$$

Dielectric core n = 2.0

For,

$\omega = 4 \times 10^{14} - 9 \times 10^{14}$ (Hz)

$t = 450 - 750$ nm

$$\begin{aligned}\beta &= -2.86733 \times 10^{7} + 7.95334 \times 10^{-8}\omega + 4.39631 \times 10^{13}t \\ &\quad -1.4343 \times 10^{-23}\omega^2 - 1.93033 \times 10^{19}t^2 - 0.02472\omega t.\end{aligned}$$

$\omega = 4 \times 10^{14} - 9 \times 10^{14}$ (Hz)

$t = 350 - 450$ nm

$$\begin{aligned}\beta &= -1.14088 \times 10^{8} + 1.82421 \times 10^{-7}\omega + 3.03427 \times 10^{14}t \\ &\quad -4.46102 \times 10^{-23}\omega^2 - 2.1498 \times 10^{20}t^2 - 0.17968\omega t.\end{aligned}$$

Dielectric core n = 2.5

For,

$\omega = 4 \times 10^{14} - 9 \times 10^{14}$ (Hz)

$t = 450 - 800$ nm

$$\begin{aligned}\beta &= -1.55081 \times 10^{7} + 7.18463 \times 10^{-8}\omega + 2.4086 \times 10^{13}t \\ &\quad -7.46259 \times 10^{-24}\omega^2 - 1.08697 \times 10^{19}t^2 - 0.0126\omega t.\end{aligned}$$

$\omega = 4 \times 10^{14} - 9 \times 10^{14}$ (Hz)

$t = 350 - 450$ nm

$$\begin{aligned}\beta &= -4.44726 \times 10^{7} + 1.09333 \times 10^{-7}\omega + 1.05957 \times 10^{14}t \\ &\quad -2.16556 \times 10^{-23}\omega^2 - 7.31737 \times 10^{19}t^2 - 0.05808\omega t.\end{aligned}$$

Dielectric core n = 3.0

For,

$\omega = 4 \times 10^{14} - 9 \times 10^{14}$ (Hz)

$t = 400 - 800$ nm

$$\begin{aligned}\beta &= -1.22715 \times 10^{7} + 7.75821 \times 10^{-8}\omega + 2.04492 \times 10^{13}t \\ &\quad -5.59765 \times 10^{-24}\omega^2 - 9.94216 \times 10^{18}t^2 - 0.00996\omega t.\end{aligned}$$

$\omega = 4 \times 10^{14} - 9 \times 10^{14}$ (Hz)

$t = 300 - 400$ nm

$$\begin{aligned}\beta &= -3.53474 \times 10^{7} + 1.0746 \times 10^{-7}\omega + 9.04739 \times 10^{13}t \\ &\quad -1.71373 \times 10^{-23}\omega^2 - 6.74423 \times 10^{19}t^2 - 0.04795\omega t.\end{aligned}$$

Dielectric core n = 3.5

For,

$\omega = 4 \times 10^{14} - 9 \times 10^{14}$ (Hz)

$t = 450 - 800$ nm

$$\begin{aligned}\beta &= -8.39088 \times 10^{6} + 8.26824 \times 10^{-8}\omega + 1.43673 \times 10^{13}t \\ &\quad -3.46659 \times 10^{-24}\omega^2 - 7.20406 \times 10^{18}t^2 - 0.00639\omega t.\end{aligned}$$

$\omega = 4 \times 10^{14} - 9 \times 10^{14}$ (Hz)

$t = 300 - 450$ nm

$$\begin{aligned}\beta &= -2.24798 \times 10^{7} + 9.9966 \times 10^{-8}\omega + 5.86262 \times 10^{13}t \\ &\quad -1.00665 \times 10^{-23}\omega^2 - 4.49514 \times 10^{19}t^2 - 0.02861\omega t.\end{aligned}$$